Evaluating the Performance of a Prototype TPC For Use in the ND280m Detector of the T2K Experiment

by

Kyle Fransham
B.Sc. (Honours) Carleton University 2005

A Thesis Submitted in Partial Fullfillment of the
Requirements for the Degree of

MASTER OF SCIENCE

in the Department of Physics and Astronomy

Evaluating the Performance of a Prototype TPC For Use in the ND280m Detector of the T2K Experiment

By

Kyle Fransham

B.Sc. (Honours) Carleton University 2005

Supervisory Committee

Dr.Dean Karlen, Supervisor
Department of Physics and Astronomy

Dr. Michael Roney, Departmental Member
Department of Physics and Astronomy

Dr. Robert Kowalewski, Departmental Member
Department of Physics and Astronomy

Dr. Isabel Trigger, External Member
TRIUMF

Supervisory Committee

Dr.Dean Karlen, Supervisor
Department of Physics and Astronomy

Dr. Michael Roney, Departmental Member
Department of Physics and Astronomy

Dr. Robert Kowalewski, Departmental Member
Department of Physics and Astronomy

Dr. Isabel Trigger, External Member
TRIUMF

Abstract

A prototype time projection chamber has been designed and constructed to study the performance that can be expected by the large scale time projection chambers in the ND280m detector of the Tokai to Kamioka (T2K) neutrino oscillation experiment. Tests using the prototype will indicate any changes necessary to the fullscale design in order to meet the physics goals of the detectors.

Some TPC gas parameters are measured, including the drift velocity, diffusion constant, and electron attachment coefficient. The spatial resolution of the TPC is also measured, and results are presented for two candidate TPC gasses.

Table of Contents

Supervisory Committee **ii**

Abstract **iii**

Table of Contents **iv**

List of Figures **viii**

List of Tables **xvi**

Acknowledgements **xviii**

1 Introduction **1**

1.1 Elementary Particle Physics 1

1.1.1 The Standard Model 1

1.1.2 Neutrino Oscillation Physics 4

1.2 The T2K Experiment 7

1.3 The ND280m Detector 10
    1.3.1 Neutrino Interactions in ND280m 11
    1.3.2 Detector Design 11

2 Time Projection Chambers **16**

2.1 TPC Basics 16
2.2 ND280m TPC Physics Requirements 17
    2.2.1 Particle Identification 17
    2.2.2 Resolution 20

3 The UVic-TRIUMF Prototype TPC **24**

3.1 Field Cage 25
3.2 Gas Amplification 26
3.3 Data Acquisition 28
    3.3.1 Pad Array 28
    3.3.2 Readout Electronics 29
    3.3.3 Trigger 32
3.4 HV Control 34
    3.4.1 Hardware 34
    3.4.2 Software 35

4 Data Analysis And Selections **39**

4.1 Removing Bad Channels 39

4.2 Track Fitting Parameters 42

4.3 Track Fitting 45

  4.3.1 Software and Algorithm 45

  4.3.2 Cuts on Fitted Tracks 48

4.4 Monte Carlo Generation 50

5 TPC Running Conditions **54**

5.1 Electric Fields 54

5.2 Trigger Configuration 54

5.3 Run Codes and Gas Choice 55

6 Measurement Methods **59**

6.1 Drift Velocity 59

6.2 Diffusion 62

6.3 Attachment 64

  6.3.1 Energy Loss 65

  6.3.2 Pressure Effects 67

6.4 Resolution 68

7 Results **72**

7.1 Drift Velocity 73

7.2 Diffusion 76
7.3 Attachment 84
7.3.1 Shaping Time Effects 92
7.4 Resolution and Bias 95
7.4.1 Overall TPC Resolution 96
7.4.2 Resolution vs Drift 101
7.4.3 Resolution vs y 108
7.4.4 Resolution vs x coordinate 119
7.4.5 Resolution vs Azimuthal Angle 124
7.4.6 Resolution vs Dip Angle 128

8 Conclusion **131**

Bibliography **133**

List of Figures

1.1 A pictorial representation of the particles in the standard model, showing the three families. The force carriers on the right are the mediating bosons described above. 2

1.2 The allowed neutrino interactions in the standard model. Above, ”l” represents any lepton. 3

1.3 The energy spectrum at 2.0 (black), 2.5 (red), and 3.0 (blue) degrees away from the axis of the neutrino beam. As the angle gets larger, the distribution gets narrower and lower in energy. [1] 9

1.4 The ratio of the reconstructed neutrino energy spectrum at Super-K with oscillation to the spectrum with no oscillation. [1] 10

1.5 A cutaway view of the ND280m detector, showing the various subdetectors. Note that one yoke of the magnet has been removed, for clarity. 12

1.6 A diagram of one of the three TPCs that will be installed in the ND280m detector 15

2.1 A schematic cutout view of a TPC . The diagram shows the cloud of ionization produced by the passage of a charged particle through the gas volume. 17

2.2 The energy loss of muons, pions, electrons and protons in Argon, normalized to the energy loss of a minimum ionizing particle. 19

2.3 A Monte Carlo study of dE/dx in the TPC for electrons (red) and muons (blue), with correct relative populations in the right hand plot. 20

3.1 A photo of the UVic-TRIUMF TPC. 25

3.2 A cross sectional view of the TPC. 26

3.3 A triple GEM stack with the different electric fields labeled. Here, E_{drift}, $E_{transfer}$ and $E_{induction}$ are all different labels for the generic E_{ext} described above. The top of GEM 1 faces the drift volume of the TPC, while the electrons are collected by the readout pads at the bottom. 28

3.4 The configuration of readout pads in the TPC. Dark grey pads are active; light grey pads are uninstrumented. 29

3.5 The charge collected by a single readout pad for a period of 100μs after a trigger. The pulse corresponding to the cloud of ionization left by a charged particle in the gas volume is clearly visible at 35μs after the trigger. 30

3.6 A block diagram of the readout chain of the TPC. Charge is collected by the readout pads, passed through the TPC outer box to the readout electronics, inverted, and digitized. 31

3.7 The scintillators NIM logic units used to trigger the TPC on cosmic rays. 33

3.8 **a)** A block diagram showing the link between computer (serial input) and the power supply. This circuit, without the DCC, is replicated ten times and used to adjust the voltage on the HV power supplies and the DCCs. **b)** The DCC attached to a GEM. The voltmeters shown are used to read the GEM voltage and current, and are present on all channels. 36

4.1 a) The mean RMS of the signal measured by each readout pad. The pads with no values correspond to uninstrumented regions of the TPC. b) The RMS of the number of electrons collected by each pad when they are not sampling the electrons produced by a track in the TPC. 40

4.2 The readout from the TPC is shown above, with three of the parameters found in the track fitting algorithm. 46

4.3 An example of the charge collected by five adjacent pads in an event. 47

4.4 Distributions of the cut quantities. 51

4.5 Distributions of the cut quantities. 52

5.1 The dimensions of the scintillators used to build the cosmic ray trigger. 56

5.2 The placement of the scintillators with respect to the TPC for 5 different trigger configurations 57

5.3 The placement of the scintillators with respect to the TPC for 3 different trigger configurations 58

6.1 The expected drift velocity as a function of electric field for different gases. 60

6.2 The readout from the TPC is shown above. The track starts below the upper pads and has a positive dip angle, signifying a cosmic ray that came through the central cathode. 61

6.3 The expected transverse diffusion of electrons drifting through gases as a function of electric field as calculated by Magboltz. 63

6.4 The fraction of electrons in a charge cloud being lost to electron capture on O_2 as a function of drift time. 65

6.5 The change in gain in the TPC as a function of inverse barometric pressure. The curve fit to the second data set is used to normalize every measured gain to a standard pressure of 101.3 kPa. 69

7.1 The drift times of tracks that crossed the central cathode in data set D4. 74

7.2 The drift velocity calculated by Magboltz of electrons in varying concentrations of $ArCO_2$. All values correspond to an electric field of 180V/cm. 74

7.3 A plot showing σ for each track that was selected in data sets A1-A4. 78

7.4 σ^2 as a function of drift time for data sets A1-A4. ($ArCO_2$ gas) . . . 79

7.5 σ^2 as a function of drift time for data sets D1-D4. ($ArCO_2$ gas) . . . 80

7.6 σ^2 as a function of drift time for data sets B1-B3. ($ArCH_4CO_2$ gas) . 81

7.7 The electron attachment of data sets A1 and A2. ($ArCO_2$ gas) 85

7.8 The electron attachment of data sets A3 and A4 ($ArCO_2$ gas) 86

7.9 The electron attachment of two different MC simulations of data sets A1 through A4.($ArCO_2$ gas) 87

7.10 The electron attachment of data sets D1 through D4.($ArCO_2$ gas) . . 88

7.11 The electron attachment of data sets B1, B2 and B3 ($ArCH_4CO_2$ gas) 89

7.12 The electron attachment of two different MC simulations of data sets B1, B2 and B3. 90

7.13 The expected standard deviation of the charge cloud in the longitudinal direction as a function of angle for different drift distances. The yellow line shows the shaping time of the electronics. 93

7.14 dE/dx as a function of angle for a fixed drift time of 475$< t_{drift} <$500. 94

7.15 The distribution of residuals in the transverse direction for $ArCO_2$ data sets A1-A4 and D1-D4. 97

7.16 The distribution of residuals in the transverse direction for $ArCH_4CO_2$ data sets B1-B3. 98

7.17 The distribution of residuals in the longitudinal direction for $ArCO_2$ data sets A1-A4 and D1-D4. 99

7.18 The distribution of residuals in the longitudinal direction for $ArCH_4CO_2$ data sets B1-B3. 100

7.19 The transverse resolution of the TPC as a function of drift time for $ArCO_2$ data sets A1-A4 and D1-D4. 102

7.20 The transverse resolution of the TPC as a function of drift time for $ArCH_4CO_2$ data sets B1-B3. 103

7.21 The longitudinal resolution of the TPC as a function of drift time for $ArCO_2$ data sets A1-A4 and D1-D4. 104

7.22 The longitudinal resolution of the TPC as a function of drift time for $ArCH_4CO_2$ data sets B1-B3. 105

7.23 The transverse resolution and bias of the TPC as a function of local y coordinate for $ArCO_2$ data sets A1-A4 and D1-D4. 109

7.24 The transverse resolution and bias of the TPC as a function of local y coordinate for $ArCH_4CO_2$ data sets B1-B3. 110

7.25 The longitudinal resolution and bias of the TPC as a function of local y coordinate for $ArCO_2$ data sets A1-A4 and D1-D4. 111

7.26 The longitudinal resolution and bias of the TPC as a function of local y coordinate for $ArCH_4CO_2$ data sets B1-B3. 112

7.27 A diagram of a track that has a bias distribution similar to that shown in figures 7.23 and 7.25 113

7.28 The transverse bias as a function of y coordinate and the residual distributions of the upper and lower modules. 115

7.29 The transverse bias as a function of y coordinate for different drift distances and x coordinates. 116

7.30 A photo of the pattern of aluminum strips on the central cathode, as well as the readout from a typical laser flash. 118

7.31 The transverse resolution and bias of the TPC as a function of local x coordinate for $ArCO_2$ data sets A1-A4 and D1-D4. 120

7.32 The transverse resolution and bias of the TPC as a function of local x coordinate for $ArCH_4CO_2$ data sets B1-B3. 121

7.33 The longitudinal resolution and bias of the TPC as a function of local x coordinate for $ArCO_2$ data sets A1-A4 and D1-D4. 122

7.34 The longitudinal resolution and bias of the TPC as a function of local x coordinate for $ArCH_4CO_2$ data sets B1-B3. 123

7.35 The transverse resolution and bias of the TPC as a function of azimuthal angle (ϕ) for $ArCO_2$ data sets A1-A4, and F1 and D2 combined. 125

7.36 The transverse resolution and bias of the TPC as a function of azimuthal angle (ϕ) for $ArCH_4CO_2$ data sets B1-B3. 126

7.37 The non-uniform ionization along a track, responsible for degrading the resolution of the TPC at larger track angles. 127

7.38 The longitudinal resolution and bias of the TPC as a function of dip angle ($\tan\lambda$) for $ArCO_2$ data sets A1-A4, and F1 and D2 combined. 129

7.39 The longitudinal resolution and bias of the TPC as a function of dip angle ($\tan\lambda$) for $ArCH_4CO_2$ data sets B1-B3. 130

List of Tables

1.1 The mass limits of the different flavours of neutrino, as compiled by the Particle Data Group. 4

1.2 The interaction types and their relative rates of occurence in the ND280m detector, as predicted by Monte Carlo simulation.[1] 11

5.1 The potentials on the TPC components. GEM DV is the potential difference between the top and bottom surfaces of a single GEM. . . . 55

5.2 The potentials on the TPC components. 55

5.3 The gasses and trigger configurations used during data taking. 56

7.1 The expected and measured drift velocities in $ArCO_2$ and $ArCH_4CO_2$ gas. 75

7.2 The fit parameters of the linear functions in figures 7.4 through 7.6 . 77

7.3 The input and measured diffusion constants (D) for Monte Carlo data sets. 77

7.4 The expected and measured diffusion constants (D) for different data sets. Expected diffusion constants for measured data were calculated by Magboltz. Measured diffusion constants presented here have been scaled by $D^{MC}_{expected}/D^{MC}_{measured}$. 82

7.5 The expected and measured electron lifetimes in $ArCO_2$ and $ArCH_4CO_2$ gas. 91

7.6 The measured TPC resolutions in $ArCO_2$ and $ArCH_4CO_2$ gas. 96

Acknowledgements

The completion of this thesis would have been infinitely more difficult without the assistance of some very special people. First of all, the contribution of my supervisor, Dr. Dean Karlen, has been phenomenal. Dean has provided me with every opportunity to increase my knowledge, and has been incredibly patient and understanding throughout the course of my Master's degree. His support, suggestions, and guidance have made this thesis many orders of magnitude better than it would be on its own. It is impossible to overstate the gratitude that I have for all that he has done for me.

The entire T2K group at UVic has provided me with countless hours of training, help with troubleshooting, explanations to problems (even for those that I caused), and most of all, an atmosphere to learn more than I could have thought possible.

Finally, I'd like to thank my parents and especially my beautiful wife, Carla, for their unflinching and unwavering support as I pursue my dreams.

Chapter 1

Introduction

1.1 Elementary Particle Physics

1.1.1 The Standard Model

The field of particle physics is broad, and is currently best described by a theory called the standard model. Developed in the early 1970's, the standard model now has sixteen fundamental particles, separated into three categories: quarks, leptons, and mediating bosons. Figure 1.1 shows the names of these particles, and how they interrelate.[2] Each of the particles in the standard model has an associated antiparticle with identical mass and opposite charge. Ordinary matter (protons, neutrons and electrons) is composed primarily from particles in the first generation. The properties of those particles outside of those that make up ordinary matter is the study

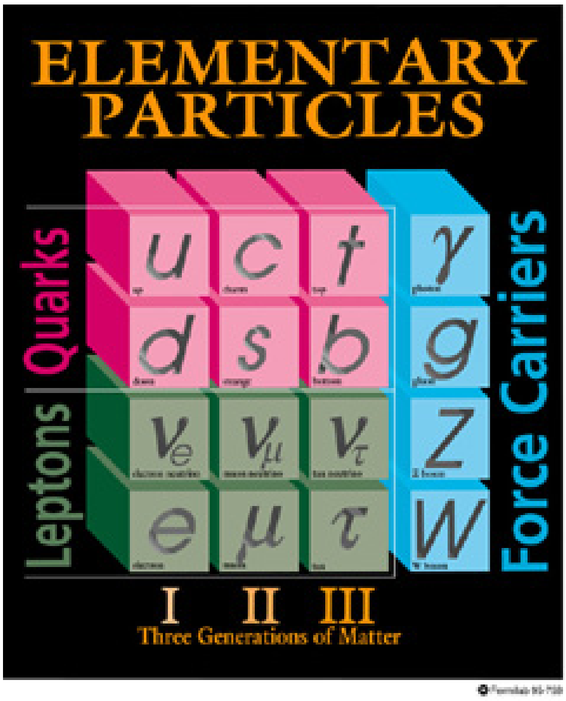

Figure 1.1: A pictorial representation of the particles in the standard model, showing the three families. The force carriers on the right are the mediating bosons described above.

of numerous particle physics experiments. [3]

Of particular interest to this thesis are the neutrinos. The existence of the neutrino was originally postulated in 1930 by Fermi, who used a massless neutral particle as an explanation for the non-monochromatic electron energy spectrum measured in beta decay experiments. The neutrino remained experimentally unseen until 1956, when Reines and Cowan used scintillators around a water target to measure neutrinos from the Savannah River Nuclear Power Plant in South Carolina.[2]

According to the standard model, the massive charged leptons can interact via the weak and electromagnetic interactions, while the neutrinos are massless and only interact weakly. The two tree-level weak interaction vertices of the neutrinos are shown in figure 1.2. Investigations into neutrino mass using a tritium decay process for the electron neutrino, a pion decay process for the muon neutrino, and a tau decay process for the tau neutrino have placed upper limits on the mass of the neutrino. [4] Table 1.1 below shows the current limits for the neutrino masses as compiled by the Particle Data Group [4].

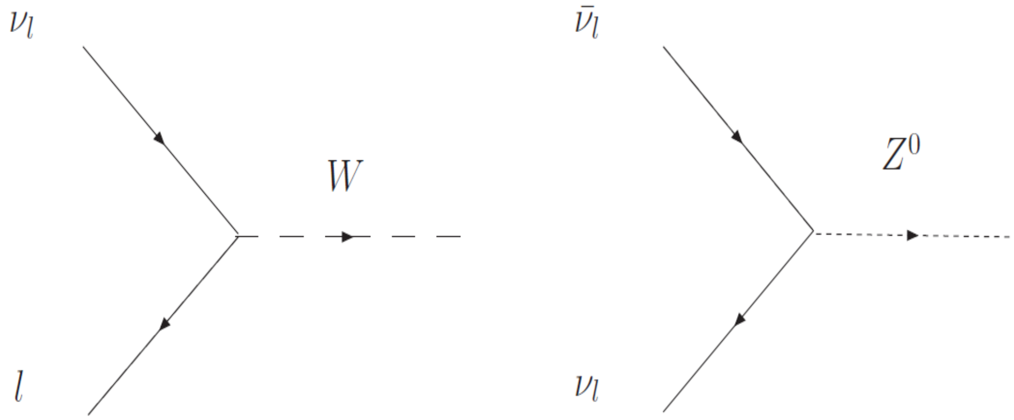

Figure 1.2: The allowed neutrino interactions in the standard model. Above, "l" represents any lepton.

In the standard model, where all neutrino masses are zero, there cannot be any mixing between flavours. However, recent results from Super Kamiokande (Super K) [5] on atmospheric neutrino oscillation and from the Sudbury Neutrino Observatory

Flavour	Mass Limit
ν_e	< 2 eV/c^2
ν_μ	< 0.17 MeV/c^2
ν_τ	< 18 MeV/c^2

Table 1.1: The mass limits of the different flavours of neutrino, as compiled by the Particle Data Group.

[6] on solar neutrino oscillation indicate that neutrinos can mix between different flavour states.

In figure 1.2, the flavour of the lepton is conserved at every vertex. This fact still holds true in the standard model, but the discovery of neutrino oscillation implies a non-zero mass difference between two neutrino states, indicating a non-zero neutrino mass. This effect will be more thoroughly discussed in the following section.

1.1.2 Neutrino Oscillation Physics

When a neutrino interacts, it does so weakly, confining itself to a single weak eigenstate. However, since the neutrino has a non-zero mass, the mass eigenstates are not necessarily the same as the weak eigenstates. In fact, weak eigenstates $|\nu_\alpha\rangle$ are superpositions of all three of the mass eigenstates $|\nu_i\rangle$, with the weak eigenstates given by:

$$|\nu_\alpha\rangle = \sum_i U^*_{\alpha i}|\nu_i\rangle \tag{1.1}$$

Where $U_{\alpha i}$ is the leptonic mixing matrix [4] given by

$$U = \begin{bmatrix} c_{12}c_{13} & s_{12}c_{13} & s_{13}e^{-i\delta} \\ -s_{12}c_{23} - c_{12}s_{23}s_{13}e^{i\delta} & c_{12}c_{23} - s_{12}s_{23}s_{13}e^{1\delta} & s_{23}c_{13} \\ s_{12}s_{23} - c_{12}c_{23}s_{13}e^{i\delta} & -c_{12}s_{23} - s_{12}c_{23}s_{13}e^{i\delta} & c_{23}s_{13} \end{bmatrix} \tag{1.2}$$

with $s_{ij} \equiv \sin(\theta_{ij})$, $c_{ij} \equiv \cos(\theta_{ij})$, and where θ_{ij} is the mixing angle between states i and j. Since U is a unitary matrix, it is invertible, so equation 1.1 also inverts:

$$|\nu_i\rangle = \sum_i U_{i\alpha}|\nu_\alpha\rangle \tag{1.3}$$

where i = 1,2,3 and $\alpha = e$, μ, τ.

For a neutrino initially in state $|\nu_i\rangle$, the propagation of the mass eigenstate through space is given by [7]:

$$|\nu_i(t)\rangle = e^{-iE'_i t'}|\nu_i(t = 0)\rangle \tag{1.4}$$

where

$$E'_i = \gamma(E_i - \beta p_i) \tag{1.5}$$

and

$$t' = t/\gamma \tag{1.6}$$

are respectively the mass and proper time in the neutrino rest frame . At relativistic energy scales, $\beta \approx 1$ and the neutrino energy in the lab frame can be rewritten as

$$E_i = \sqrt{p_i^2 + m_i^2} \approx p_i + \frac{m_i^2}{2p_i} \tag{1.7}$$

Combining equations 1.5, 1.6 and 1.7 shows that the phase factor in equation 1.4 is

$$e^{-i(m_i^2/2p_i)t} \tag{1.8}$$

where m_i is the mass of mass eigenstate i.

To simplify the equations, a system of units has been adopted where the speed of light (c), and the reduced Plank's constant ($\hbar$) are both set equal to unity. Because the velocity of the neutrino is near the speed of light, this choice of units implies that the time t is equal to the distance travelled by the neutrino, L. Finally, assuming that momentum is constant between the $|\nu_i\rangle$ states implies that $p_i = p \approx E$, where E is the average energy of all of the different mass eigenstate components of the neutrino.[4] The state vector for a neutrino initially in the $|\nu_\alpha\rangle$ state is therefore

$$|\nu_\alpha(L)\rangle \approx \sum_i U_{\alpha i}^* e^{-i(m_i^2/2E)L} |\nu_i\rangle \tag{1.9}$$

Inserting equation 1.3 into equation 1.9 above gives the state vector as a function of distance travelled in terms of the observable weak eigenstates $|\nu_\beta\rangle$ and the masses

m_i of the mass eigenstates: [4]

$$|\nu_\alpha(L)\rangle \approx \sum_\beta \left[\sum_i U^*_{\alpha i} e^{-i(m_i^2/2E)L} U_{\beta i} \right] |\nu_\beta\rangle \tag{1.10}$$

Therefore, the probability for a neutrino created with flavour α to be measured in flavour state β after having travelled a distance L is:

$$\begin{aligned} P(\nu_\alpha \to \nu_\beta) &= |\langle \nu_\beta | \nu_\alpha(L) \rangle|^2 \qquad (1.11) \\ &= \delta_{\alpha\beta} - 4 \sum_{i<j} \Re(U^*_{\alpha i} U_{\beta i} U_{\alpha j} U^*_{\beta j}) \sin^2[1.27 \Delta m_{ij} (L/E)] \\ &\quad +2 \sum_{i<j} \Im(U^*_{\alpha i} U_{\beta i} U_{\alpha j} U^*_{\beta j}) \sin[2.54 \Delta m_{ij} (L/E)] \qquad (1.12) \end{aligned}$$

In the limit where only two of the mass states dominate the oscillation, the probability of a μ neutrino not to oscillate reduces to

$$P(\nu_\mu \to \nu_\mu) = 1 - \sin^2 2\theta_{23} \sin^2 \left(\frac{1.27 \Delta m^2_{23} L}{E} \right) \tag{1.13}$$

1.2 The T2K Experiment

T2K is a long-baseline neutrino oscillation experiment designed to place strict limits on some of the parameters of the lepton mixing matrix shown in the previous section. Specifically, more accurate measurements of the parameters $\sin^2 2\theta_{23}$ and

Δm_{23} through $\nu_\mu \rightarrow \nu_x$ oscillation, and a measurement of $\sin^2 2\theta_{13}$ through $\nu_\mu \rightarrow \nu_e$ appearance are the main goals of the first phase of the experiment. Future goals also include improving the sensitivity to the CP violating phase term in the lepton mixing matrix, δ. [1]

The experiment itself is localized in two locations: Tokai, on the east side of Japan; and Super-Kamiokande (Super-K) in the west. At Tokai, a 30-50 GeV synchrotron produces a 0.75MW proton beam, which in turn strikes a target, primarily producing pions. The pions from the interactions in the target are focused by three horn magnets, and are then directed towards a long helium-filled tunnel, where they decay: $\pi \rightarrow \mu + \nu_\mu$. The horn magnet can be tuned to focus positive or negative pions, which subsequently decay into neutrinos or anti-neutrinos respectively. The pion beam is directed 2.5^o away from the final detector at Super-Kamiokande, since an off-axis neutrino beam has a sharper, narrower energy distribution, as shown in figure 1.3.

The neutrino beam, originally created as ν_μ with a small ν_e background, propagates 295 km to Super-Kamiokande, where the final neutrino spectra are measured. Super-Kamiokande is a 50 kTon ring-imaging water Cherenkov detector, located 2700m underground in the Kamioka Mozumi mine in Japan. The detector is cylindrical, and instrumented about the cylinder's surface are 11200 photomultiplier tubes that collect the Cherenkov light emitted from the charged products of neutrino inter-

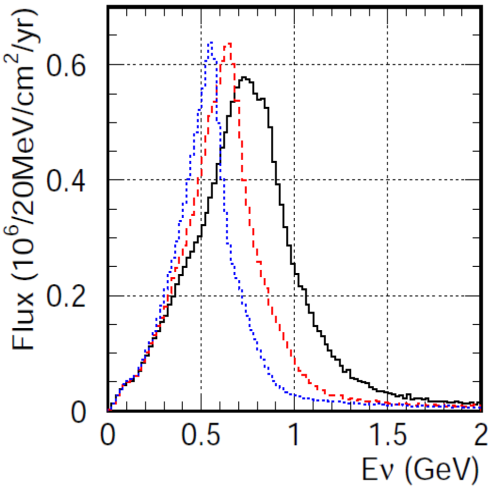

Figure 1.3: The energy spectrum at 2.0 (black), 2.5 (red), and 3.0 (blue) degrees away from the axis of the neutrino beam. As the angle gets larger, the distribution gets narrower and lower in energy. [1]

actions in the water volume. Reconstruction of the Cherenkov ring allows for some distinction between charged current events created by a ν_μ and those created by a ν_e .

The oscillation parameters $\sin^2 2\theta_{13}$ and Δm^2 are measured by the ν_μ survival probability, after the ν_μ has travelled the 295km between JPARC and Super-K. Figure 1.4 shows the ratio between the neutrino spectra at Super-K with and without neutrino oscillation, in the case of oscillation with parameters $\sin^2 2\theta_{13} = 1.0$ and $\Delta m^2 = 2.7 \times 10^{-3} eV^2$. The depth of the dip in this figure is dependent on the magnitude of $\sin^2 2\theta_{13}$, while the location of the minimum scales with Δm^2.

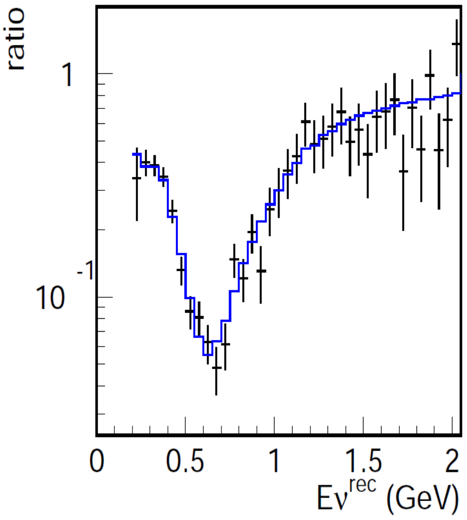

Figure 1.4: The ratio of the reconstructed neutrino energy spectrum at Super-K with oscillation to the spectrum with no oscillation. [1]

1.3 The ND280m Detector

The entire T2K experiment hinges on determining the fraction of ν_μ that have oscillated into another flavour, and to perform this measurement it is crucial to understand the energy spectrum and flavour content of the neutrino beam at creation. The Near Detector at 280 meters (ND280m) from the proton target has been designed with this specific purpose in mind. Like Super-K, the ND280m detector samples the neutrino beam 2.5^o off-axis, ensuring that the neutrino energy distribution is similar at both detectors.

1.3.1 Neutrino Interactions in ND280m

In the ND280m detector, many different charged-current (CC) and neutral-current (NC) reactions are expected. The CC interactions proceed through exchange of a W boson, while NC reactions involve exchange of the neutral Z^0 boson. Figure 1.2 shows the allowed CC and NC vertices. Table 1.2 shows the particles that participate in the different interactions, as well as the fraction of neutrino events in the near detector that are expected to proceed through the various channels.

Event Type	Reaction	Fraction
CCQE	$\nu_\mu + n \to \mu^- + p$ $\nu_\mu + e \to \mu^- + \nu_e$	38.3%
CC1π	$\nu_\mu + p \to \mu^- + p + \pi^+$	10.5%
	$\nu_\mu + n \to \mu^- + p + \pi^0$	2.9%
	$\nu_\mu + n \to \mu^- + n + \pi^+$	3.0%
CCNπ	$\nu_m u + nucleon \to \mu^- + N\pi$	7.0%
CC-Other	...	9.8%
NC1π	$\nu_\mu + n \to \nu_\mu + n + \pi^0$	1.7%
	$\nu_\mu + p \to \nu_\mu + p + \pi^0$	2.1%
	$\nu_\mu + n \to \nu_\mu + p + \pi^-$	1.1%
	$\nu_\mu + p \to \nu_\mu + n + \pi^+$	1.1%
NCNπ	$\nu_m u + nucleon \to \nu_\mu + N\pi$	2.1%
NC-Other	...	20.4%

Table 1.2: The interaction types and their relative rates of occurence in the ND280m detector, as predicted by Monte Carlo simulation.[1]

1.3.2 Detector Design

The ND280m detector is composed of multiple subdetectors, shown in figure 1.5, all surrounded by a large magnet. The magnet produces a 0.2T magnetic field throughout

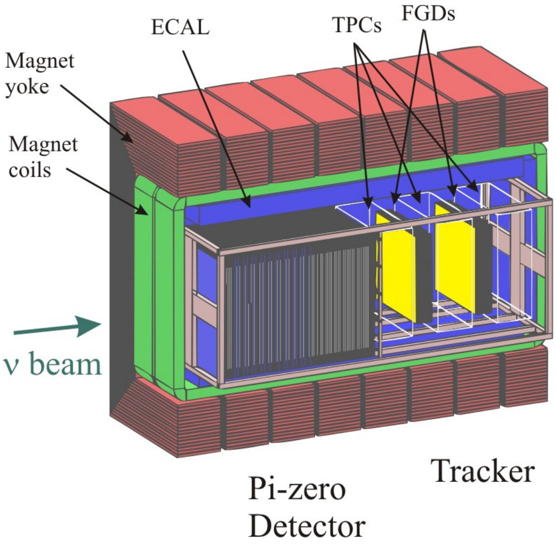

Figure 1.5: A cutaway view of the ND280m detector, showing the various subdetectors. Note that one yoke of the magnet has been removed, for clarity.

the volume of the detector, useful in determining the charges and momenta of particles produced in neutrino interactions. The magnet is composed of two C-shaped yokes, each with 16 nested iron leaves, and was formerly used in the UA1 experiment at CERN.

Side Muon Range Detector

Strips of plastic scintillator instrumented with wavelength-shifting fibers are placed in between the leaves of the magnet, and this subdetector is known as the Side Muon Range Detector (SMRD). The SMRD serves two main functions. First, the energies of muons produced in the detector can be estimated by measuring the depth of penetration into the magnet. This is especially useful for interactions where the muon momentum cannot be measured by the tracker, either because the muons do not pass through the tracker, or because they have small angles with respect to the magnetic field, making the bending radius difficult to measure. The second main function of the SMRD is to serve as a signal to identify neutrino interactions in the yokes, and to identify cosmic ray particles passing through the detector.

Pi-Zero Detector

At the upstream end of the ND280m detector is the Pi-Zero Detector (P0D), which will be used to measure the neutral current π^0 rate: $\nu_\mu + p \rightarrow \nu_\mu + p + \pi^0$ [1]. The P0D consists of 76 alternating X and Y scintillator bar tracking planes, with a 0.6mm lead sheet spliced between each scintillator bar layer. The lead helps to increase the efficiency for detecting gamma rays produced in π^0 decays. In the central region of the P0D, a 3cm thick re-fillable water bladder separates each tracking layer, providing a removable oxygen target for neutral current neutrino interactions. This oxygen target is vital to measure the π^0 production rate as a function of energy and direction, in order to predict the π^0 production rate at Super-K.

Electromagnetic Calorimeter

The Electromagnetic Calorimeter (ECAL) surrounds the tracker and the P0D, and is used primarily to identify photons produced by the decay of a π^0, where the π^0 was produced in the tracker or the P0D as a result of neutral or charged current neutrino interactions. Since the photons are produced at all angles [1], the ECAL is designed to be hermetic, and is placed on all sides of the inner detector (composed of the tracker and P0D). The outer section of the ECAL is composed of alternating 3mm lead sheets and 1cm x 5 cm scintillator bar layers, while the inner section, known as the pre-radiator section, is composed of three lead sheets, each backed with three layers of scintillator bars. Wavelength shifting fibers are placed in all scintillator bars, and connected to photomultipliers for readout.

Tracker

The nd280m tracker is composed of three Time Projection Chambers (TPCs) separated by two Fine Grained Detectors (FGDs). The three TPCs are identical gas-filled detectors that measure the ionization deposited by charged particles passing through their active volume. Figure 1.6 shows a schematic of one of the three TPCs. The outer dimensions of each TPC are 1.0m in the direction along the neutrino beam, and 2.5m in the other two directions. A 7 cm gas gap separates an inner volume from the outer TPC box. Each TPC is bisected by a central cathode, and read out

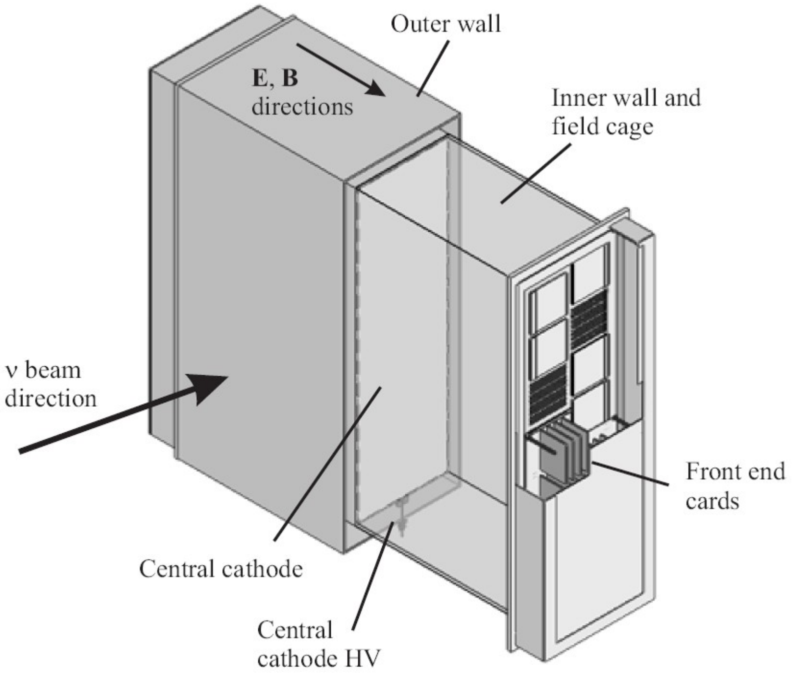

Figure 1.6: A diagram of one of the three TPCs that will be installed in the ND280m detector

on both ends. Section 2.2.2 details the physics requirements for the ND280m TPCs, and chapter 2.1 describes time projection chambers in more detail.

The upstream FGD is composed of 30 layers of 1cm x 1cm scintillator bars, alternating in X and Y orientation. The downstream FGD is similar in construction to the upstream FGD, but with every second XY layer replaced with a passive water target. The FGDs provide target mass for the incoming neutrinos, and their finely segmented design is useful for tracking of recoil protons and charged pions, allowing for separation between CCQE and CC-nonQE events.

Chapter 2

Time Projection Chambers

2.1 TPC Basics

A Time Projection Chamber (TPC) is a gas-filled detector designed for tracking the paths of charged particles. When particles pass through the detector, gas molecules along the track are ionized. A strong uniform electric field is applied to the drift volume, which drifts the cluster of electrons from the ionization to a readout plane perpendicular to the electric field, where the charge is collected and amplified.

The readout plane of a TPC is segmented into different channels, and the charge deposited on each channel is recorded. Measuring the drift time of electrons in the gas permits a full 3D reconstruction of the incident particle's path, since ionization created close to the readout plane arrives before the electrons from a track segment that is far away. Figure 2.1 shows a cutaway view of a generic TPC, with a schematic representation of the track of ionization resulting from the passage of a charged particle.

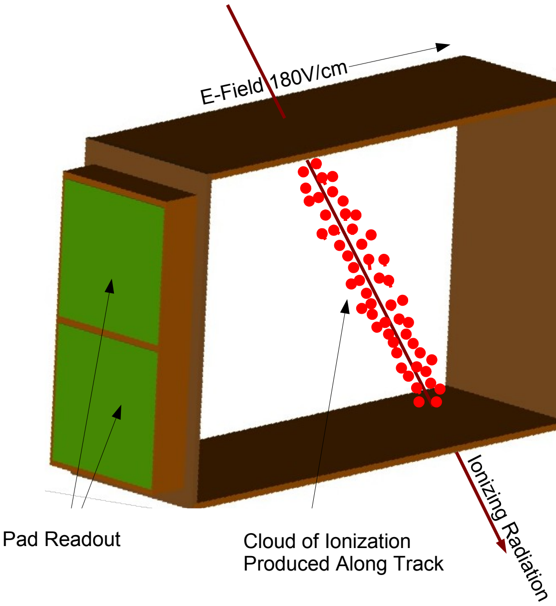

Figure 2.1: A schematic cutout view of a TPC . The diagram shows the cloud of ionization produced by the passage of a charged particle through the gas volume.

2.2 ND280m TPC Physics Requirements

2.2.1 Particle Identification

As shown in section 1.2, the measurement of $\sin^2 2\theta_{13}$ is accomplished by observing the appearance of ν_e at Super-K. The probability for a ν_μ to oscillate to a ν_e is small, and there is a small ν_e component in the beam when it is created in Tokai. It is therefore very important for the ND280m detector to understand the fraction of ν_e already in the beam, allowing the intrinsic ν_e background to be subtracted from the total measured ν_e signal at Super-K.

To determine the fraction of intrinsic ν_e in the beam, a relatively clean sample of CCQE ν_e events in ND280m must be selected. Since lepton flavour is conserved in the CCQE interaction, ν_e CCQE events produce an electron in the final state. Selecting those electrons produced by ν_e CCQE interactions permits the determination of the ν_e flux at the ND280m detector, and doing so requires the detector to be able to distringuish between these electrons and the muons produced in ν_μ CCQE interactions. The TPCs are designed to discriminate between electrons and muons by looking at the energy loss as a function of track length (dE/dx) of the different particles. At the energy scale of the T2K experiment, electrons deposit more energy than muons in a gas as they travel through it, as shown below in figure 2.2.

Comparing the dE/dx of electrons and muons at energies between 0.2 and 1.2 GeV, (the energies for which the ν_e background must be determined) there is a separation in the dE/dx curves. The ability of the TPCs to correctly identify a particle as being an electron or a muon is therefore dependent on the dE/dx resolution of the detector.

Empirically, the dE/dx resolution of time projection chambers has been found to be:

$$\frac{\sigma(dE/dx)}{< dE/dx >} = 0.41n^{-0.43}(xP)^{-0.32} \tag{2.1}$$

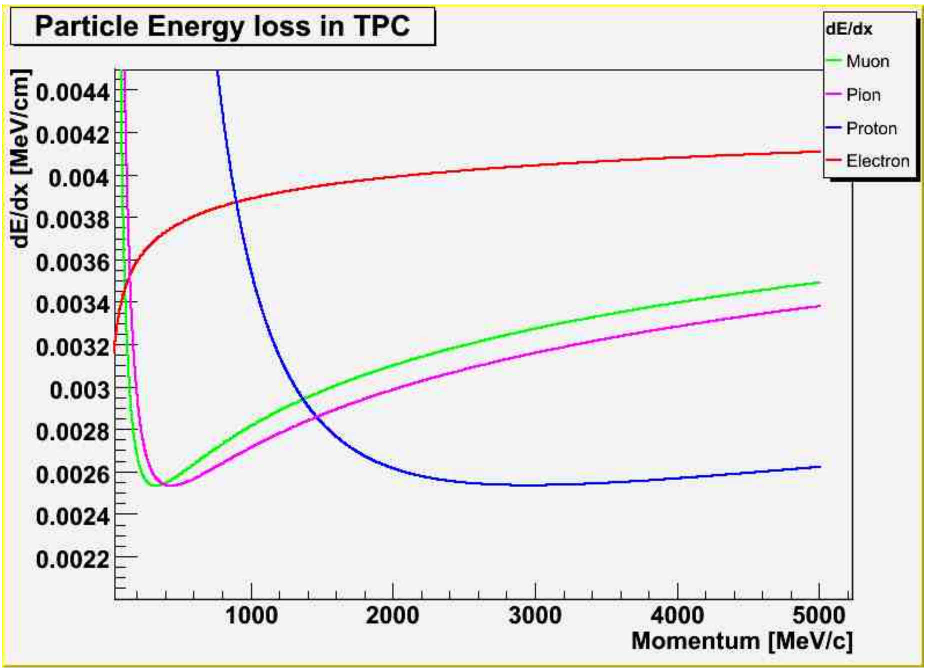

Figure 2.2: The energy loss of muons, pions, electrons and protons in Argon, normalized to the energy loss of a minimum ionizing particle.

where $< dE/dx >$ is the expected dE/dx at a particular energy from figure 2.2, n is the number of TPC pad rows that a track crosses, x is the projected path length of the track over each pad row in cm, and P is the pressure of the TPC gas in atm. In a single TPC, particles travelling directly along the beam axis cross 72 pad rows, each having a width of 1 cm, corresponding to a dE/dx resolution of ∼7%. This result improves significantly if the track crosses two TPCs. Also, if the track is angled with respect to the pad plane, the projected path length x will increase, improving the dE/dx resolution.

Using this information, Monte Carlo studies using a GEANT4 simulation of the

ND280m detector[8] show good separation between the dE/dx of electrons and muons from CCQE interactions. Figure 2.3 shows the dE/dx distributions of electrons and muons in the TPC. Inspecting figure 2.3 shows that selecting only those tracks with a measured dE/dx greater than the mean of the electron distribution would result in a sufficiently pure sample of electrons.

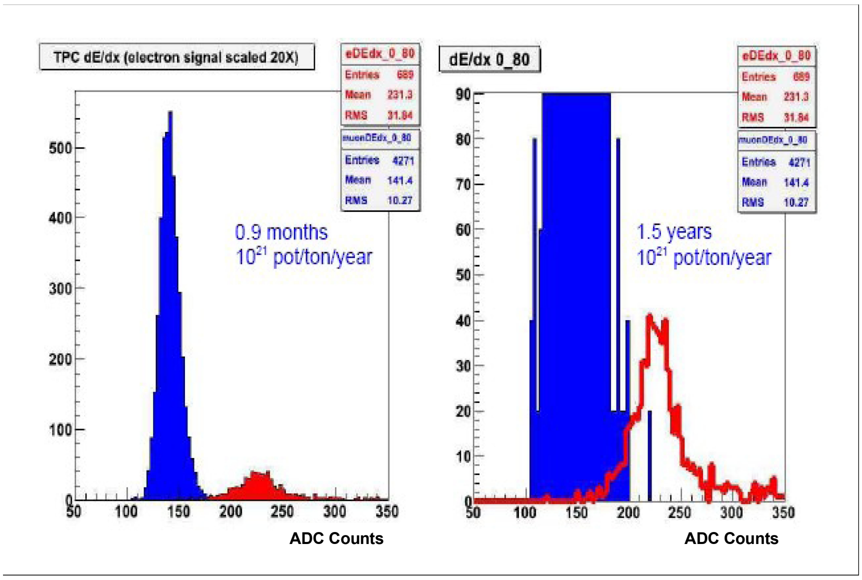

Figure 2.3: A Monte Carlo study of dE/dx in the TPC for electrons (red) and muons (blue), with correct relative populations in the right hand plot.

2.2.2 Resolution

The main role of the three TPCs in the ND280m detector is to determine the neutrino energy spectrum by measuring the momenta of muons produced in CCQE interactions. The reconstruction of the neutrino energy from the energy of the final state muon is limited to 10% by Fermi motion inside of the target nucleus resulting from the neutrino collision. This restriction means that the TPC needs to be able to determine the muon momentum to better than 10% at energies less than 1 GeV, since the neutrino energy spectrum is mostly contained between 0.2 and 1.2 GeV, as shown in figure 1.3.

Restricting the muon momentum determination to better than 10% implies that the radius of curvature must also be known to 10% since the two quantites are linearly proportional:

$$p\cos\lambda = 0.3zBR \tag{2.2}$$

where p is the momentum in GeV/c, λ is the pitch angle, z is the particle's charge, B is the magnetic field in Tesla, and R is the radius of curvature in meters. [4] This can be used to place requirements on the space point resolution of the TPC. The curvature error on the track of a charged particle in a magnetic field, using many uniformly spaced measurements of the particle's position is approximately:

$$\sigma^2_{1/R} = \sigma^2_{1/R_{res}} + \sigma^2_{1/R_{ms}} \tag{2.3}$$

where $\sigma^2_{1/R_{res}}$ is the curvature error due to a finite detector resolution, and $\sigma^2_{1/R_{ms}}$ is the curvature error due to multiple scattering. Ignoring the smaller term, $\sigma^2_{1/R_{ms}}$, the curvature error can be parameterized as:

$$\sigma_{1/R} = \sigma_{1/R_{res}} = \frac{\epsilon}{L'^2}\sqrt{\frac{720}{N+4}} \tag{2.4}$$

where ϵ is the spatial resolution from one row of pads in the TPC, L', is the projected length of the track on the readout plane of the TPC, and N is the number of points measured along the track. [4] A 1 GeV/c muon that crosses straight across the entire TPC has $L' = 72$ cm, $N = 72$, and $\cos\lambda = 1$. Imposing the restriction on the curvature

$$\frac{\sigma_{1/R}}{1/R} < 0.1 \tag{2.5}$$

sets a limit on the spatial resolution of the TPC of

$$\epsilon < \frac{1}{10}L'^2\sqrt{\frac{N+4}{720}}\left(\frac{0.3zB}{p\cos\lambda}\right) \approx 1\text{mm} \tag{2.6}$$

A Monte Carlo simulation has been developed to confirm that the spatial resolution of the TPC will give the desired momentum resolution, and the results from the Monte Carlo are compared to those from a prototype TPC, both described in detail in the following chapters.

Results from the prototype TPC will also be analyzed to explore some of the systematic effects that could reduce the sensitivity to the neutrino oscillation parameters described previously. In order for the systematic uncertainties to remain lower than the statistical error on the measurements, the energy scale of the distribution of muons reconstructed from CCQE interactions in ND280m must be known to 2% or better.[1]

Since the momentum of muons is measured by the radius of curvature of a charged track in the TPCs, the accuracy of the oscillation measurements is especially sensitive to any systematic effects producing a shift in the radius of curvature of a particle. A particle with a transverse momentum of 1 GeV/c has a radius of curvature of 16.7m in the 0.2T magnetic field of the ND280m detector. If this track crosses the entire 760mm width of a TPC, it has a sagitta of 4.3 mm. A change in sagitta of ±0.1 mm produces a shift in the measured radius of curvature of 2%, so any biases in the TPCs producing a shift in curvature must be understood at the 0.1mm level. The prototype TPC will help to give some insight into the type of biases that can be expected in the full-size TPC modules in ND280m.

Chapter 3

The UVic-TRIUMF Prototype TPC

Construction of the TPC used in this analysis was accomplished by a joint effort between the University of Victoria and TRIUMF in Vancouver, BC, and was completed in December, 2005. Figure 3.1 shows a side view of the TPC, before any of the front-end electronics were connected. The drift volume of the TPC has glass-epoxy laminate (G10) walls clad with copper about its surface, and is bounded on one end by a copper-clad G10 cathode. The opposite end of the drift volume faces two stacks of three gas electron multipliers (GEMs) in front of the readout electronics, described below in sections 3.2 and 3.3 respectively.

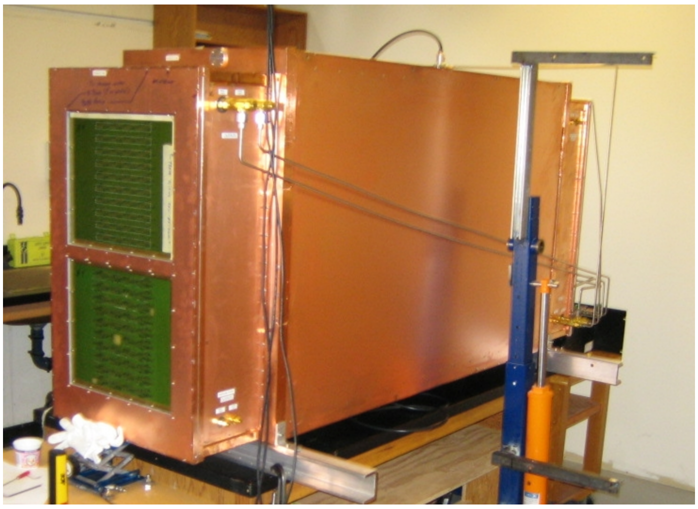

Figure 3.1: A photo of the UVic-TRIUMF TPC.

3.1 Field Cage

The copper cladding on the G10 walls of the drift volume has been machined away in strips, leaving strips of copper surrounding the drift volume. Each strip is connected to the adjacent strips via two 20MΩ resistors in parallel. Applying a negative voltage to the central cathode, which is in turn connected to the first of the copper strips, creates a uniform electric field in the active region of the detector. The strips help to shape the field inside of the drift volume, and a wire grid in front of the readout further increases the field uniformity.

The field cage is encased by an outer box, with a gas gap between the two walls. The walls of the outer box are constructed from copper clad rohacell, and act as a Faraday cage, preventing any external electric fields from contaminating the field in the drift volume. Figure 3.2 shows a cross-sectional view of the TPC.

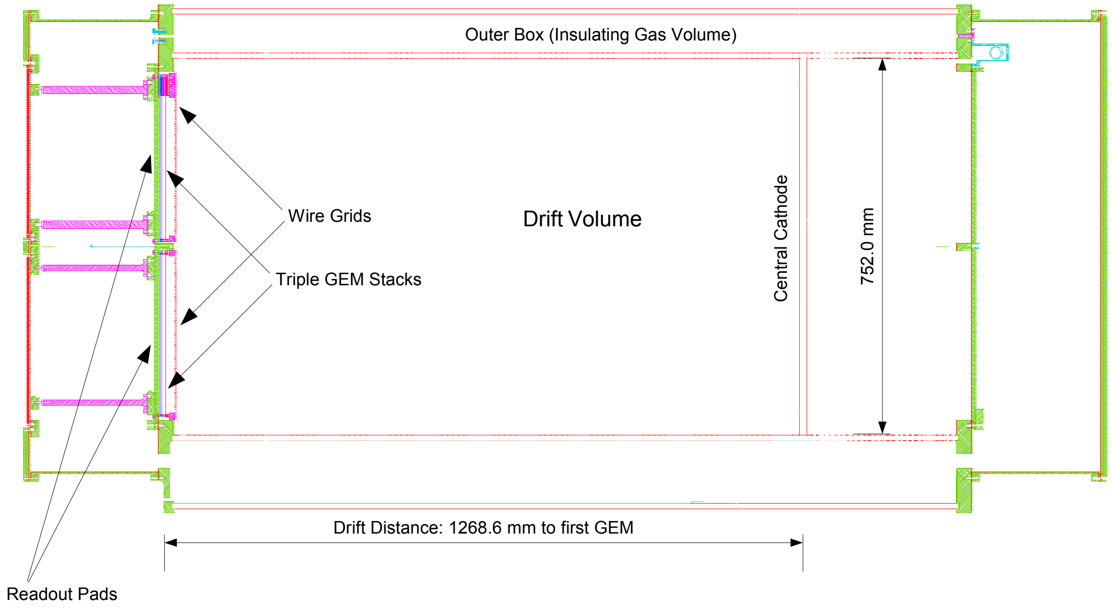

Figure 3.2: A cross sectional view of the TPC.

3.2 Gas Amplification

To increase the amplitude of the signal from electrons drifting in the gas volume, a series of three gas electron multipliers (GEMs) is placed in front of each readout module. A GEM foil consists of two sheets of conductor separated by a 50μm thin insulating layer with a uniform pattern of open holes across the entire active surface. The pitch and diameter of the holes can vary for different GEM designs, but are typically on the order of 100 to 200μm and 50 to 100μm respectively.[9] A potential difference of several hundred volts between the two conductive layers creates a large electric field in the GEM holes, accelerating and multiplying electrons that drift toward the foils.

The potentials applied to the GEM surfaces are chosen to increase the number of electrons produced in the GEM holes, collect all of the electrons from the drift volume into the GEM holes, while ensuring that there is almost no breakdown between the surfaces of the GEM. These criteria are all functions of the ratio E_{ext}/E_{hole}, where E_{ext} is the magnitude of the external field outside of the GEM holes, and E_{hole} is the magnitude of the electric field inside of the GEM holes. [10] E_{hole} is defined by the difference in potential between the surfaces of a single GEM, while E_{ext} is defined by the difference in potential between the top or bottom surface of the GEM and the potential of the adjacent element in the drift chamber. Figure 3.3 below shows a triple GEM stack and the E_{ext} and E_{hole} fields.

In the prototype TPC, there are two separate GEM stacks, each of which lies above a separate readout board. The combination of a wire grid, three GEMs and a pad readout board is called a module. Modules 1 and 2 are visible in figures 2.1 and 3.2.

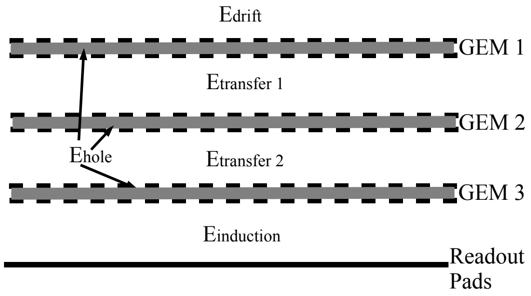

Figure 3.3: A triple GEM stack with the different electric fields labeled. Here, E_{drift}, $E_{transfer}$ and $E_{induction}$ are all different labels for the generic E_{ext} described above. The top of GEM 1 faces the drift volume of the TPC, while the electrons are collected by the readout pads at the bottom.

3.3 Data Acquisition

3.3.1 Pad Array

The boundary of the inner TPC volume is defined by the readout pads, directly behind the GEMs. The readout pads are 0.8cm × 0.8cm gold-plated copper squares etched onto a printed circuit board. Each pad is connected by a feedthrough to the other side of the circuit board, which faces the outer gas volume. Each channel is then conneced to a cable that relays the signal through the outer box, where it is connected to the front-end electronics. Figure 3.4 shows the configuration of readout pads, as seen from a perspective outside of the TPC. The smaller pads visible on the top and bottom of figure 3.4 are 0.6cm × 0.6cm in size, and were made to study the resolution of a more finely segmented pad array. Because the number of readout

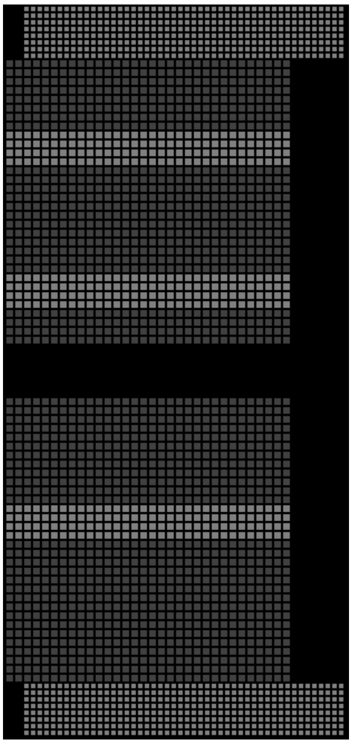

Figure 3.4: The configuration of readout pads in the TPC. Dark grey pads are active; light grey pads are uninstrumented.

channels available in the electronics was less than the number of pads, the small pads and the large pads shown in light grey in figure 3.4 were left uninstrumented.

3.3.2 Readout Electronics

When an ionizing particle crosses the cosmic telescope, a trigger signal is sent to the readout electronics. The electronics measures the amount of charge collected per 100ns time bin for a total of 100μs after a trigger. Figure 3.5 shows the charge collected by a single readout pad after the readout electronics have been activated by

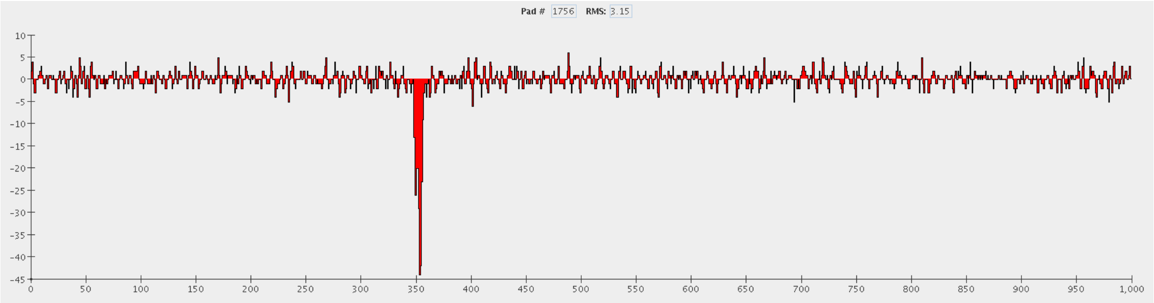

Figure 3.5: The charge collected by a single readout pad for a period of 100μs after a trigger. The pulse corresponding to the cloud of ionization left by a charged particle in the gas volume is clearly visible at 35μs after the trigger.

the trigger.

To measure the amount of charge collected by a pad during each time interval, each pad is connected via ribbon cables and feedthroughs to an inverter card outside the outer box. Each inverter card houses 128 signal inverters, used to change the polarity of the electron signal so that it can be read by the front-end cards (FECs). The FECs used in the prototype TPC were originally developed for the ALICE TPC. [11] The ALICE TPC has anode wires that collect the drifting electrons, inducing a positive signal on readout pads below. The FECs were therefore developed to process a signal of positive charge. Since the T2K prototype TPC has readout pads that directly collect the signal electrons, the inverter cards are needed to change the polarity of the signal, enabling it to be read by the FECs.

Each FEC houses eight ALice Tpc ReadOut (ALTRO) chips, and each ALTRO chip concurrently process 16 channels. When the system is triggered, the charge collected by the pads is inverted, then sampled and amplified by a charge sensitive amplifier, which transforms the signal into a semi-gaussian shape that is read by the ALTRO chip. The ALTRO chip then converts the signal to a digital form and saves it to memory. The memory holds up to 1000 such samples for each event, and can store up to 8 events at any time. [11] Figure 3.6 shows a block diagram of the TPC readout chain.

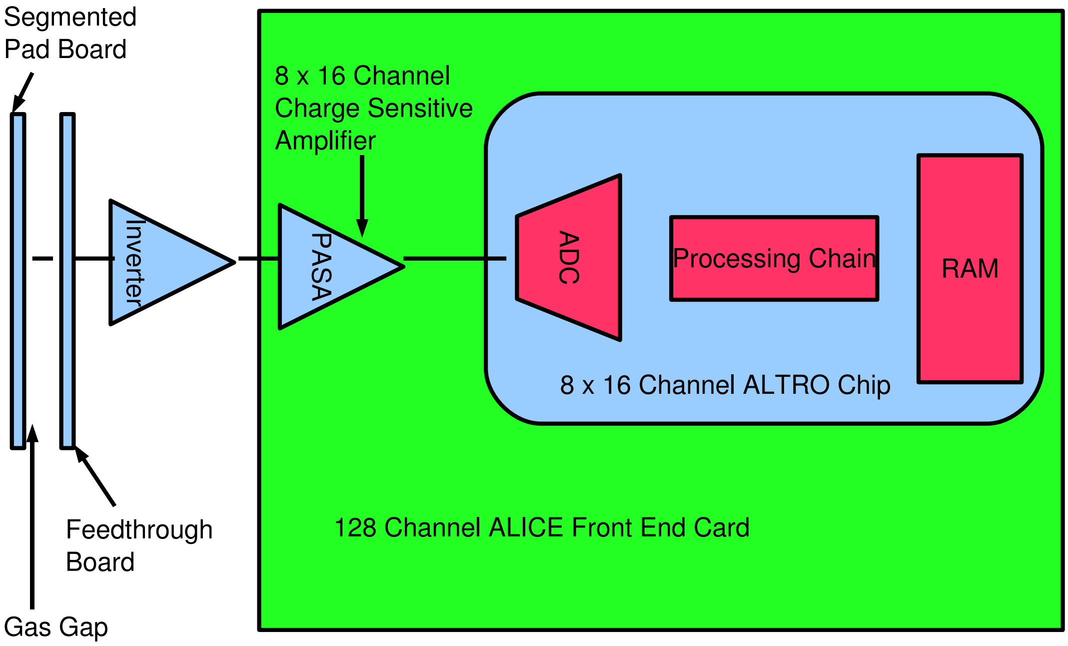

Figure 3.6: A block diagram of the readout chain of the TPC. Charge is collected by the readout pads, passed through the TPC outer box to the readout electronics, inverted, and digitized.

A custom backplane bus interfaces up to 9 FECs with a U2F data concentrator card. For the prototype TPC, six FECs were connected to the upper module, and seven FECs were connected to the lower module. Each module has its own backplane bus and data concentrator card. Both of the concentrator cards were connected to a USB hub, which was then interfaced to a personal computer running Scientific Linux. The Maximum Integrated Data Acquisition System (MIDAS) was used to interface the computer to the data concentrator cards and read out events from the FECs. MIDAS is a physics-oriented data acquision system jointly developed at the Paul Scherrer Institute in Switzerland and at TRIUMF. Based on a C library with several applications, MIDAS allows the data acquisition system to be controlled from offsite. This is a useful feature for overnight data runs.

3.3.3 Trigger

In order to observe the cosmic rays used to test the prototype TPC, one layer of plastic scintillator paddles was placed above the TPC, and two layers of paddles, separated by 15cm of lead, were placed below. Through NIM logic units, the outputs from all three layers were attached to a coincidence unit. A trigger is sent to the Data Acquisition (DAQ) electronics when all three paddles simultaneously register the passage of a charged particle. Figure 3.7 shows three scintillator paddles attached to the different discriminators, coincidence unit, delay units, and gate generator used in the cosmic telescope. When the coincidence unit registers a hit on all three scintillators, the

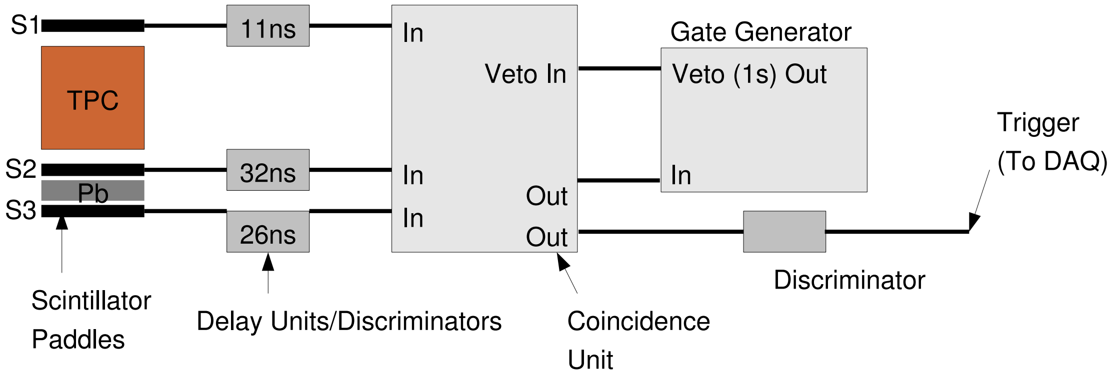

Figure 3.7: The scintillators NIM logic units used to trigger the TPC on cosmic rays.

trigger is fired, and a second output activates the gate generator. The output from the gate generator is fed back into the veto on the coincidence unit, ensuring that the ionized electrons have drifted through the gas volume, and the event has been read by the readout electronics. The lead between the bottom two scintillator paddles ensures that only Minimum Ionizing Particles (MIPs) can fire all of the scintillators. The placement of the paddles relative to the detector was used to study different regions of the TPC, as well as to select cosmic ray tracks with a specific angular distribution. The specific scintillator paddle configurations that were used for these measurements are detailed in section 3.3.3.

3.4 HV Control

A custom high voltage (HV) control system was designed for this project. More details can be found in reference [12].

3.4.1 Hardware

In order to maintain field uniformity across both modules in the prototype TPC, the two wire grids are connected to a single power supply, as are the top surfaces (facing the drift volume) of each corresponding pair of GEMs between modules. (i.e. The top surface of the top GEM (GEM 1) in one module is connected to the top surface of GEM 1 in the other module.) This results in a total of four high voltage (HV) power supplies needed to power the wire grid and the top surfaces of all of the GEMs. The supplies each have an analog input for remote control, such that 0-10 V input proportionally outputs 0-10 kV.

The bottom surfaces (facing the readout pads) of all of the GEMs are biased relative to the top surfaces through the use of EMCO G05 isolated DC to DC converters (DCCs). These DCCs take an input voltage of 0-12 VDC, and proportionally output 0-500 VDC. The use of these DCCs to bias the GEMs enforces the condition that there is never more than 500 Volts between the surfaces of a single GEM, regardless of the magnitude of the voltage on the top surface. Furthermore, if the GEM should develop a problem, the potential across the GEM can be reduced while still keeping the upper surface at the same potential as its neighbour in the other module, allowing the TPC to continue operating. Figure 3.8b shows the input HV powering the top surface of a GEM, and the DCC powering the lower surface. The figure also shows the DATEL 20-LCD-0-9 voltmeters used to monitor the current and voltage across each GEM. The voltmeters are battery operated, allowing them to float at high potentials and allows the current to be monitored at the 1nA level.

To control the HV power supplies and the DCCs, an 8 bit MICROCHIP PIC16F627A microcontroller was programmed to read a serial input, and connected to a Digital to Analog Converter (DAC) that outputs 0-10 VDC. Figure 3.8 below shows the connections between serial input, microcontroller and DAC. The block in figure 3.8a represents the main circuit used to generate the 0-10 Volt input required by the HV power supplies and the DCCs. This circuit (without the DCC) was replicated ten times; six were attached to DCC modules to control the voltage across the six GEMs, and four were connected to the remote inputs of the HV power supplies to define the potentials of the top surfaces of the GEMs and the wire grid.

3.4.2 Software

Serial communication between the computer and the on-board microchips was accomplished through the use of a publicly available Java Communications API (commapi),[13] which facilitates communication between Java applications and the computer's serial

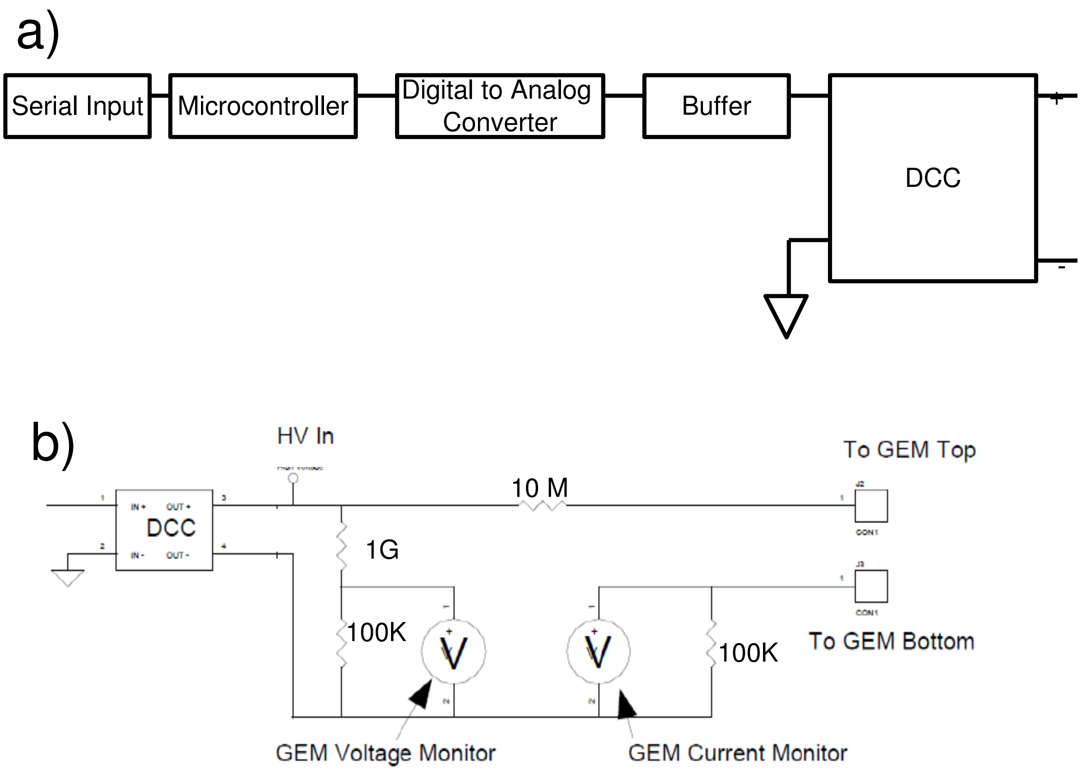

Figure 3.8: **a)** A block diagram showing the link between computer (serial input) and the power supply. This circuit, without the DCC, is replicated ten times and used to adjust the voltage on the HV power supplies and the DCCs. **b)** The DCC attached to a GEM. The voltmeters shown are used to read the GEM voltage and current, and are present on all channels.

ports. A one-way communication protocol between the computer and microcontroller was developed using five-byte data strings. The first byte is the address of the particular microcontroller (0 through 9). The second byte is a command, telling the microcontroller which action to perform, while the following two bytes are a value associated with that particular command. The final byte is a checksum. For this implementation, five actions (commands) were defined:

- **Set:** Upon receiving the "set" command, the microcontroller sets a target output voltage on the DAC according to the value specified by the next two bytes in the serial string. Since a 12 bit DAC was used, there are 4096 possible analog output voltages, ranging between 0 and 10 volts. After sending a "set" command, therefore, the computer sends a value ranging from 0 to 4096, depending on the desired output voltage. This value is stored in the microcontroller's memory.

- **Speed:** Since a rapid change in voltage can potentially be damaging to some components in the TPC, all voltages are slowly ramped by the microcontroller. The speed at which the voltage changes is defined by the number of milliseconds that the system waits before incrementing the voltage by one output step, where one output step corresponds to approximately 2.44mV.

- **Goto:** After a microcontroller has a target voltage (specified by the “set” command) and a speed stored in memory, it is given a “goto” command to instruct it to begin ramping to the target voltage at the specified speed.

- **Max:** The “max” command defines a maximum target voltage for a microcontroller. If the microcontroller recieves any “set” commands with a target voltage greater than the previously defined maximum, it will ignore them.

- **Reset:** The reset command forces the microcontroller to begin ramping down at the fastest speed possible, regardless of what action it is currently performing. The “reset” command is a useful way to return all voltages to zero should any unforseen problems arise.

Chapter 4

Data Analysis And Selections

4.1 Removing Bad Channels

Before identifying tracks in a data set, a search for noisy channels is performed. Inspecting the readout for a single pad shown in figure 3.5 shows that there is some noise present, seen by fluctuations in the signal for time bins not associated with the actual pulse. To quantify the amount of noise in a particular channel, two criteria are examined.

First, for each of the 1664 active channels, the RMS of the charge collected for each event is measured, and the mean RMS for all of the events in the data set is calculated. Figure 4.1a shows the mean RMS of the signal for all of the channels in a data set with 1132 events. Analyzing this figure shows that the mean RMS of

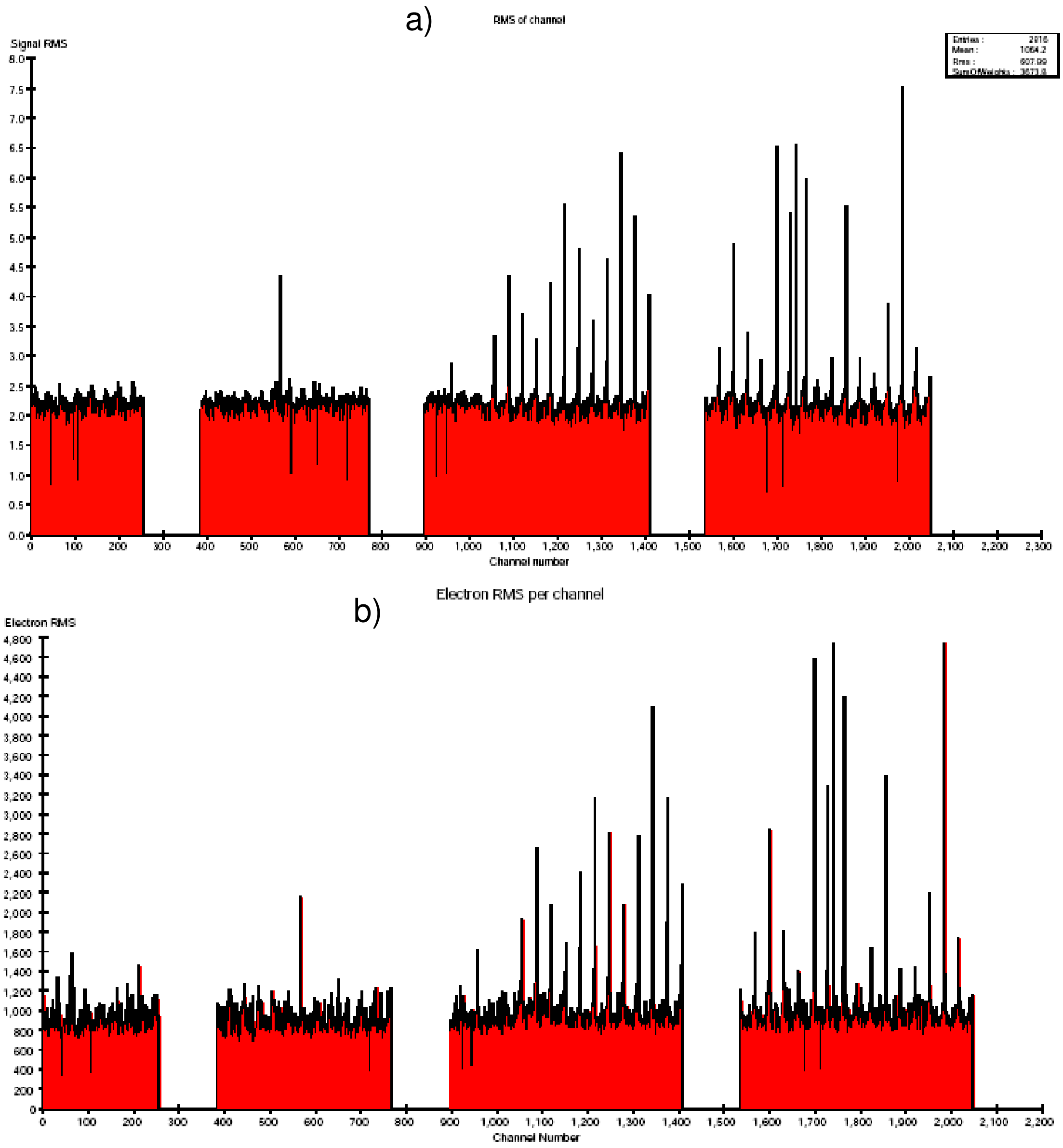

Figure 4.1: a) The mean RMS of the signal measured by each readout pad. The pads with no values correspond to uninstrumented regions of the TPC. b) The RMS of the number of electrons collected by each pad when they are not sampling the electrons produced by a track in the TPC.

the signal has a similar value for the majority of pads, but there are some that have an RMS that is noticeably lower or higher than the typical value. Pads with a small RMS could be the result of a faulty ampifier, or a malfunction in some other electronic component. Channels with a mean RMS less than 1.5 are therefore eliminated from the analysis. Furthermore, no data from any channel with a mean RMS greater than 2.7 is used, since pads with a large RMS can register false signals. Noise from any one of the electronic components, or factors internal to the TPC could cause a channel to have a large RMS.

A second method quantifies the noise in terms of equivalent electrons. Random time bins are sampled, and the corresponding number of electrons that would create a similar fluctuation in the signal is estimated for those time bins. The RMS of this quantity is used to define the electron equivalent noise, and it must be between 600 and 1500 for the channel to be acceptable.

There is a periodicity apparent in figure 4.1, especially as channel number increases. Since the pads are numbered horizontally along the rows, a bad area in the TPC causes the pad RMS to be large in intermittent channel numbers. Figure 4.2 in the following section shows the pads that do not pass the noise cuts in a lighter shade of gray. It can be observed that the pads along the outsides of the lower module are noisier than those in the center. The reason for this is unknown, but it persists across multiple front end readout and inverter cards.

4.2 Track Fitting Parameters

In order to perform the track fit in the most rigorous and efficient manner, a number of parameters are defined before finding cosmic ray tracks in the events. The list below describes these parameters, which values were used, and how they affect the track fitter.

General Settings

- **Bad Channels** The readout from any channels that do not pass the noise cuts defined above in section 4.1 is ignored.
- **Bad Rows** Any uninstrumented pad rows in the TPC, or rows that are excessively noisy are defined, and their readout is ignored.
- **Seed Rows** The two rows used to define a straight track, used as a seed for the fitting algorithm. As discussed below, these are rows 17 and 43.
- **Minimum Number of Rows Hit** The minimum number of pad rows with hits along the track defined by the seed rows. If there were less than 20 rows with such signals, no track was found.
- **Minimum Number of Electrons Per Pad** To constitute a signal, a pad must collect more than this number of electrons. In this analysis, the electron

cutoff was set to 5000 for runs that used $ArCO_2$ gas, and 6000 for runs using $ArCH_4CO_2$ gas.

Basic Pulse Finding/Fitting

- **Pedestal** The number of time bins to use for calculating the pedestal is input, as well as the time bin to start the pedestal calculation. For this analysis, the first 50 time bins (out of the total of 1000) were used for the pedestal calculation.
- **Time Slice** The time slice defines which time bins to use in the analysis, and which to ignore. Due to a bug in the MIDAS software, all data from the last time bin (999) had to be ignored.
- **Number of Pads per Peak** This parameter defines the number of adjacent pads to use when finding peaks in the signal. This was set to four.
- **Number of Time Bins per Peak** This parameter defines the number of sequential time bins to use when finding peaks in the signal. This parameter was set to six.
- **Minimum Cluster Size** The cluster-finding algorithm will define a cluster as a group of adjacent pads having a minimum summed signal equal to this parameter. The minimum cluster size was set to be 100.0 ADC counts in this analysis.

- **Gain** The number of ADC channels (see section 3.3.2) per femtocoulomb of charge deposited on the readout pads.

To estimate the total amount of charge collected by a pad, the average pulse height over a variable number of bins can be used. The parameters that define the pulse are listed below.

- **Pulse Delay** The number of time bins to use after the peak in the charge calculation time bin was set to two.
- **Pulse Length** The total number of time bins to use in the average pulse height calculation. Five time bins were used.
- **Minimum Pulse Length** Pulses must be longer than four time bins, to reject pulses that span the start or end of the readout time.
- **Delayed Ratio** The delayed ratio is the average ratio of summed signal after the pulse delay to peak signal. It scales the summed signal to be on average the same as the peak height.

4.3 Track Fitting

4.3.1 Software and Algorithm

The track-fitting software used to fit the cosmic ray data collected by the TPC is a TPC data analysis package written in Java, called jtpc. [14] The jtpc analysis package reads in the raw data produced by the MIDAS software package described in Section 3.3, and uses a cluster-finding algorithm to find the tracks. If a cluster of charge is found, the center of charge in rows 17 and 43 are used to define a straight track, which is then used as the seed for the track fitter. See Figure 4.2 for the locations of these rows. If there is no pad in row 17 or 43 where the amount of charge collected is above the noise threshold, no track is found and the event is rejected. Selecting rows 17 and 43 also places initial cuts on the angle and fiducial containment of the track, since tracks that cross only one module cannot deposit charge on both of these rows.

After a seed track has been found, the information in all of the active rows is used to fit the track. Two separate fits are performed on each track. The first is a four parameter fit, and uses the maximum likelihood method to fit the projection of the track on the readout plane [15]. Figure 4.2 shows the parameters that are fit in this case. The first parameter, x0, is the x-coordinate of the fitted track where it crosses the center of the TPC, at y=0. The second parameter, ϕ, is the angle between the track and the y-axis of the TPC, where the x and y axes are as defined

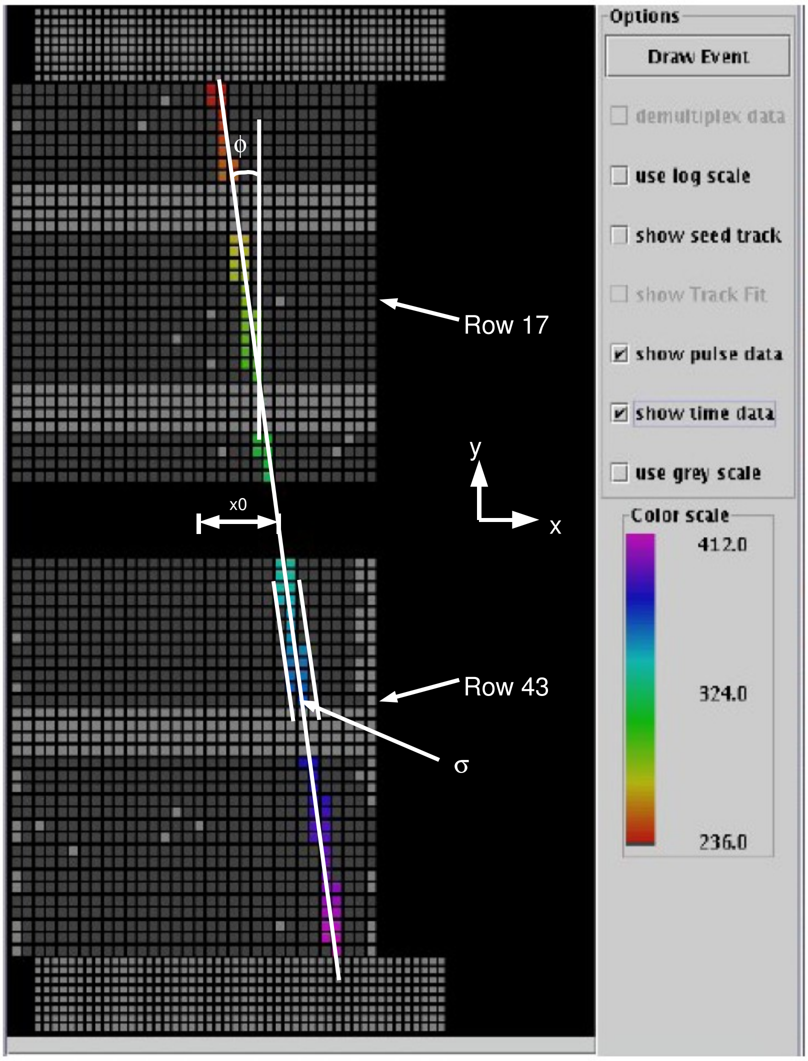

Options

Draw Event

☐ demultiplex data

☐ use log scale

☐ show seed track

☐ show Track Fit

☑ show pulse data

☑ show time data

☐ use grey scale

Figure 4.2: The readout from the TPC is shown above, with three of the parameters found in the track fitting algorithm.

in figure 4.2, and the positive z axis is parallel to the drift direction, increasing with drift time (a left handed coordinate system). Also fit are the track width (σ), and the inverse radius of curvature. Since the tracks are from cosmic rays in the absence of a magnetic field, the tracks are straight with an infinite radius of curvature, so the inverse radius of curvature is fixed at zero.

The minimum negative log likelihood fit uses not only the pads that were hit, but also the amount of charge collected by each pad. For example, see figure 4.3 which shows the charge collected for five adjacent pads in an event. Since pad 3 collected more charge than pad 1, the center of the track must have been closer to pad 3 than pad 1. The charge distribution of a cluster of electrons created by an ionizing particle has a Gaussian profile as the electrons drift through the gas, so the center of charge in

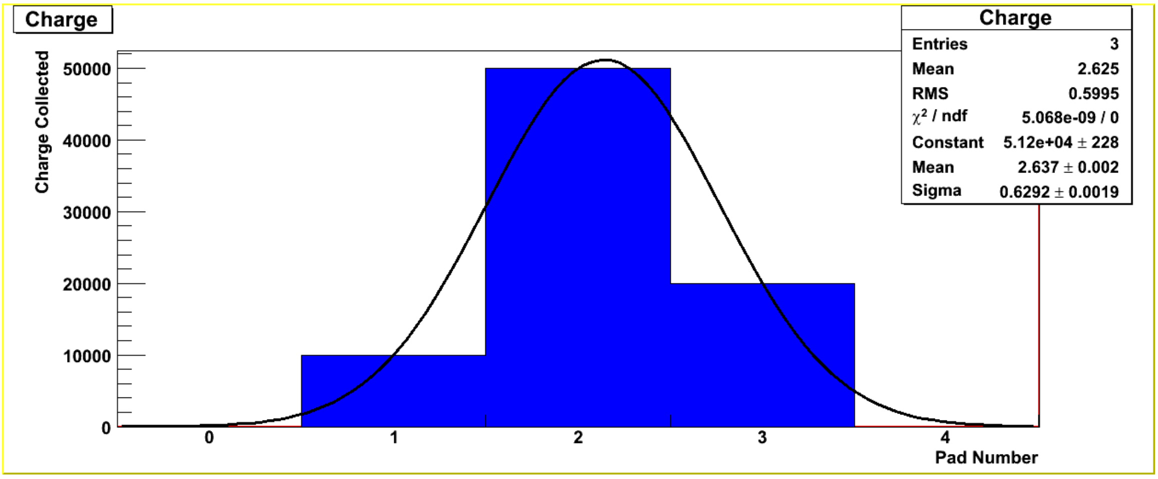

Figure 4.3: An example of the charge collected by five adjacent pads in an event.

this simple example is found by fitting a Gaussian distribution to the charge collected by the pads. The center of charge corresponds to the location of the incident ionizing particle. When fitting for actual tracks, the fit method uses the charge information from all the pads in a cluster to fit for x0, σ, ϕ, and 1/R as defined above.

Independently from the fit in the readout plane, a second fit is performed using timing information, where the dip angle (tanλ) and z-coordinate at y=0 (z0) are determined from the arrival time of the peak of the signal pulse on each pad row.

4.3.2 Cuts on Fitted Tracks

After the track fit has been performed, a number of selections can be placed on the fitted tracks to improve the quality of the data. In order to study the performance of the TPC, events where a single particle fires all three scintillators and leaves a track of charge in the gas are desired. Therefore, cuts have been placed on the data to eliminate events where multiple particles cross the TPC, where more than one particle triggers the readout, or where the particle leaving a track in the TPC is not the same particle that caused the scintillators to fire. These cuts are listed below, and figures 4.4 and 4.5 show sample distributions of the parameters that are being cut on, indicating which values of these parameters are selected or rejected. The distributions shown in the figure are for $ArCH_4CO_2$ gas; some of the actual cut values are different for the other gas ($ArCO_2$) used in the experiment but the relative positions in the distributions are similar.

- **Fiducial Cuts** Any tracks with $|x0| < 110$mm are rejected. This cut selects against particles on the very edges of the TPC. Also, situations where the primary particle crosses only one module but there is a cluster of charge in row 17 or 43 due to noise or a secondary incident particle are removed from the data set.

- **Vertical Cuts** $ArCO_2$ tracks with $|\mathrm{tanl}| > 0.6$, $ArCH_4CO_2$ tracks with $|\mathrm{tanl}| > 0.2$, and any tracks with $|\phi| > 0.5$ are cut. This cut mainly rejects tracks from particles that did not fire the scintillators.

- **Track Width Cuts and Error Cuts** These two selections place requirements on the goodness of fit of the track. For $ArCO_2$ gas, only tracks with $0.75 < \sigma < 2.5$ are kept. Since $ArCH_4CO_2$ gas has a larger diffusion constant, only tracks with $1.75 < \sigma < 4.0$ are kept. Tracks with a small width can be the result of a failure in the track fitting algorithm, or can be due to tracks that deposit charge on only one pad in each row. Occasionally, two particles pass through the TPC close enough together that only a single cluster of charge is found. A large σ is a signature of this type of event, so cuts on the maximum value of sigma are placed to reject these two-particle tracks. When doing the fit, errors on the parameters x0 and σ are determined. The limits $\mathrm{err(x0)} < 0.2$ and $\mathrm{err}(\sigma)$

< 0.2 are imposed to select against unusual tracks or fitter errors. Only a small fraction of events are removed.

- **Drift Time Cuts** For fiducial containment of the track, the cuts (150 time bins) $<$ z0 $<$ (950 time bins) are imposed for $ArCO_2$ gas. Since $ArCH_4CO_2$ gas has a much larger drift velocity, the cuts (50 time bins) $<$ z0 $<$ (375 time bins) are imposed on the data.
- **Return Code Cut** A return code of 0 is returned by the track fitter in the case of a normal track fit. If the software detects a noisy event, a track on the edge of the TPC, or if the fitter fails while it is fitting the track, a non-zero integer is returned. Only events with a return code of 0 are therefore analyzed further.
- **Cluster Cut** The cluster finding algorithm hunts for clusters according to the parameters described in the previous section. Since only single tracks through the TPC are desired, any event where more than one cluster is found in one row of pads is rejected from the analysis.

4.4 Monte Carlo Generation

Monte Carlo data were produced to use as a comparison with the measured data. A cosmic ray generator, written using the GEANT3 software suite, [16] was used to

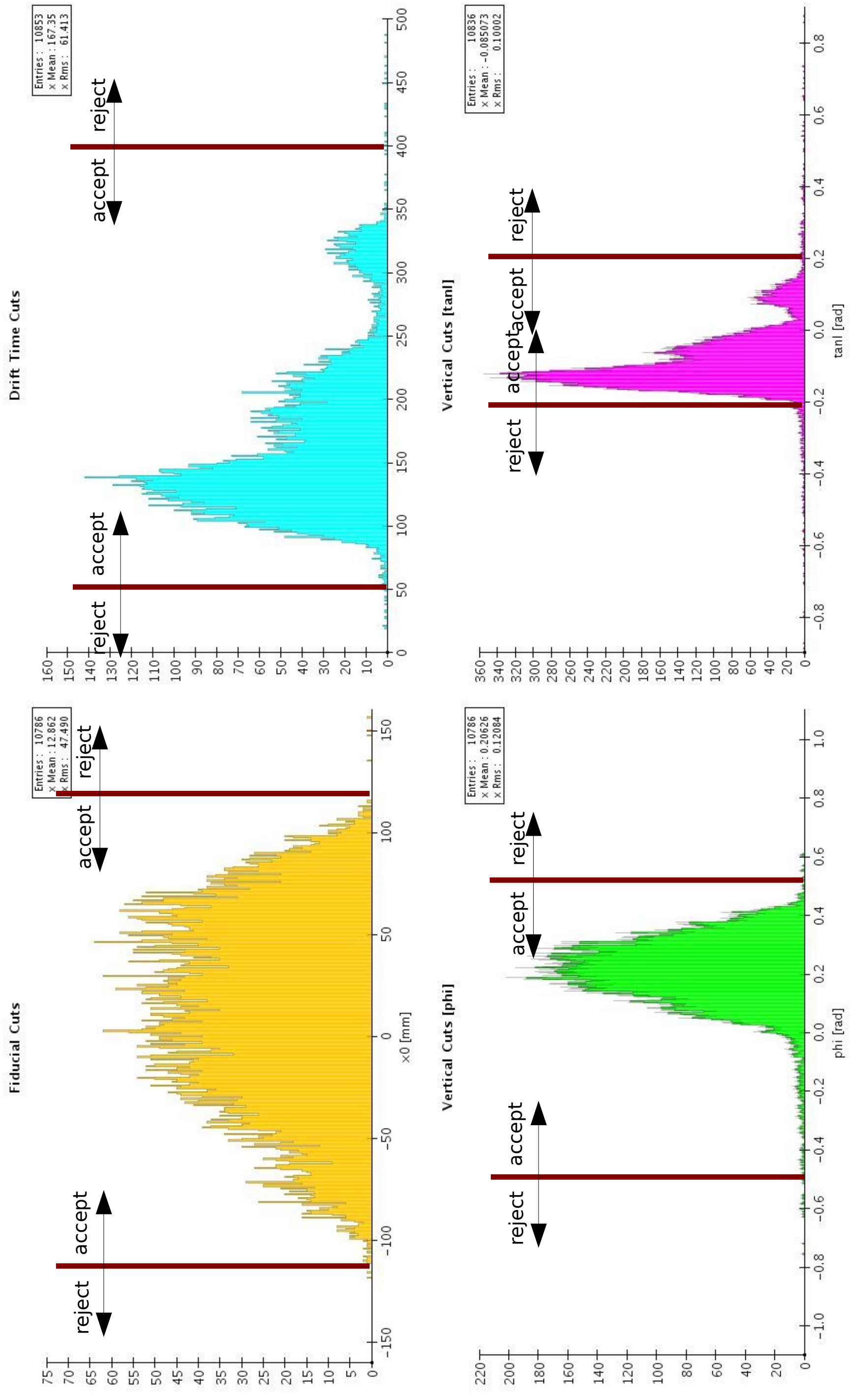

Figure 4.4: Distributions of the cut quantities.

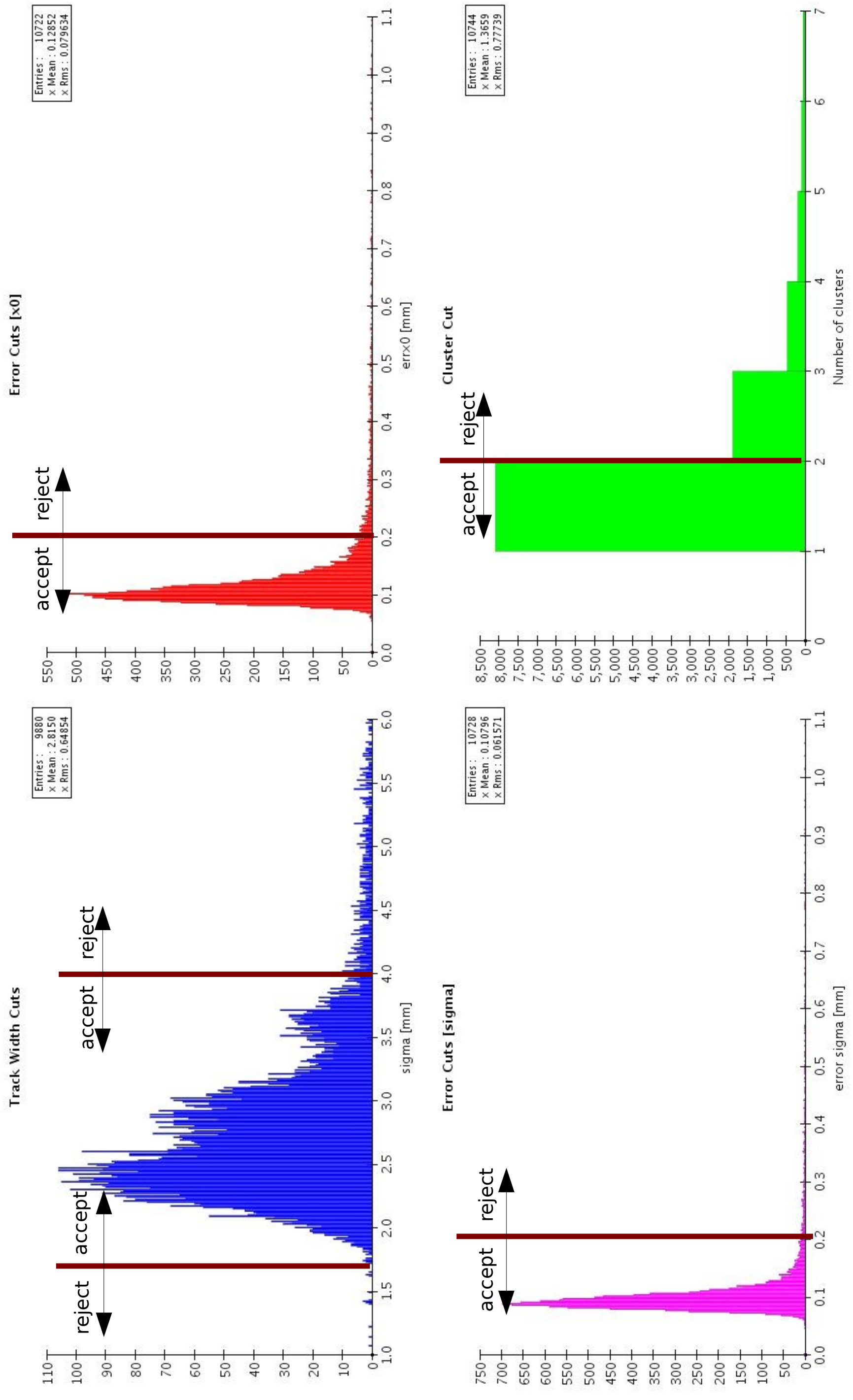

Figure 4.5: Distributions of the cut quantities.

simulate cosmic ray muons passing through the TPC. The GEANT software package is a tool that uses Monte Carlo techniques to simulate the passage of elementary particles through matter.

Once the track locations and energy deposition in the gas have been simulated by GEANT, the jtpc TPC simulation program is used to simulate clusters of ionization along the track. These clusters of ionization are then propagated through the gas of the TPC, and evolve according to the diffusion constant, drift velocity, and attachment coefficient of the gas. The input values for the diffusion constant and the drift velocity were estimated by using Magboltz, [17] a program which describes electron transport properties in electric and magnetic fields for various gasses. The following sections describe these parameters in more detail.

After the simulated clusters of ionization have been propagated through the TPC, the TPC simulation program then transforms the charges into simulated pad hits. Using the properties of the electronics described in section 3.3.2, the simulated charges collected by each pad are converted to digital pad readout signals, in the same format as the output from the MIDAS software. The analysis of the Monte Carlo data then proceeds in an identical fashion as the cosmic ray data collected by the TPC.

Chapter 5

TPC Running Conditions

5.1 Electric Fields

The operation of the TPC is highly sensitive to the magnitudes and directions of the electric fields in different regions of the detector. A single electric field configuration was used for all of the data that were taken. Table 5.1 lists the potentials on different TPC elements, and table 5.2 lists the corresponding electric fields in the regions of the TPC.

5.2 Trigger Configuration

Different trigger configurations were used during the data-taking phase. Figure 5.1 shows the sizes of the scintillators that were used to construct the trigger, and figures

TPC Element	**Voltage**
Central Cathode	-25.14 ± 0.1 kV
Wire Grid	-2668 ± 2 V
Drift Low	-2573 ± 2 V
GEM 1 Top	-2232 ± 2 V
GEM 2 Top	-1488 ± 2 V
GEM 3 Top	-744 ± 2 V
GEM DV	-360.0 ± 0.1 V
Pad Readout	0

Table 5.1: The potentials on the TPC components. GEM DV is the potential difference between the top and bottom surfaces of a single GEM.

TPC Region	**Electric Field**
Drift Field	180 V/cm
Transfer Field 1	800 V/cm
Transfer Field 2	800 V/cm
Induction Field	800 V/cm

Table 5.2: The potentials on the TPC components.

5.2 and 5.3 show the placement of the scintillators with respect to the TPC. Figure 3.7 shows the vertical placement of S1, S2 and S3.

5.3 Run Codes and Gas Choice

Throughout the experiment, different gases and trigger configurations were tested in the TPC. Table 5.3 lists the run code, gas, and trigger configuration of the TPC for all of the analyzed data. The trigger configurations are shown in figures 5.2 and 5.3. Henceforth, every data set will be refered to by its run code.

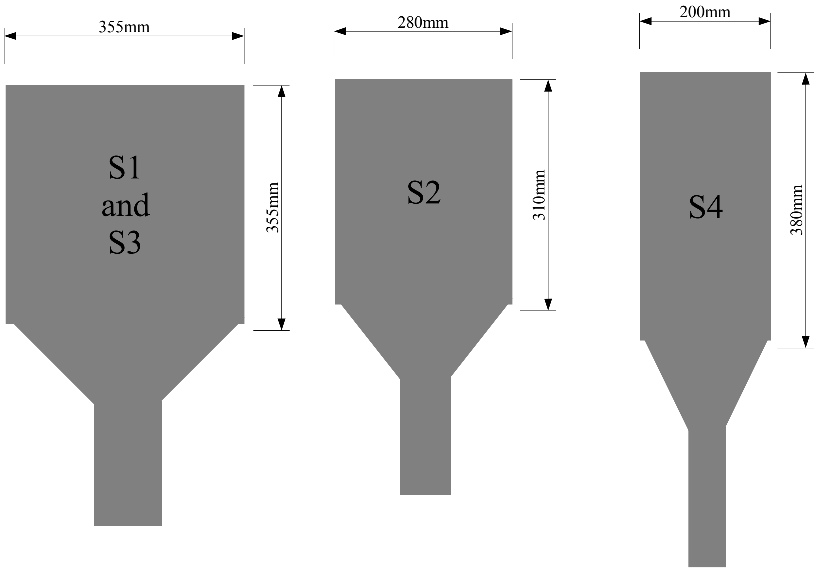

Figure 5.1: The dimensions of the scintillators used to build the cosmic ray trigger.

Run Code	**Gas**	**Flow Rate**	**Trigger Config.**
A1	Ar:CO_2 90:10	1l/min	Case 1
A2	Ar:CO_2 90:10	0.5l/min	Case 1
A3	Ar:CO_2 90:10	2l/min	Case 1
A4	Ar:CO_2 90:10	1l/min	Case 1
B1	P5:CO_2 98:2	1l/min	Case 1
B2	P5:CO_2 99:1	1l/min	Case 1
B3	P5:CO_2 97:3	1l/min	Case 1
C1	(Ar:N_2 99:1):CO_2 90:10	1l/min	Case 1
C1	(Ar:N_2 98:2):CO_2 90:10	1l/min	Case 1
D1	Ar:CO_2 90:10	1l/min	Case 2
D2	Ar:CO_2 90:10	1l/min	Case 3
D3	Ar:CO_2 90:10	1l/min	Case 4
D4	Ar:CO_2 90:10	1l/min	Case 5
E1	Ar:CO_2 90:10	1l/min	Case 6
E2	Ar:CO_2 90:10	1l/min	Case 7
F1	Ar:CO_2 90:10	1l/min	Case 8

Table 5.3: The gasses and trigger configurations used during data taking.

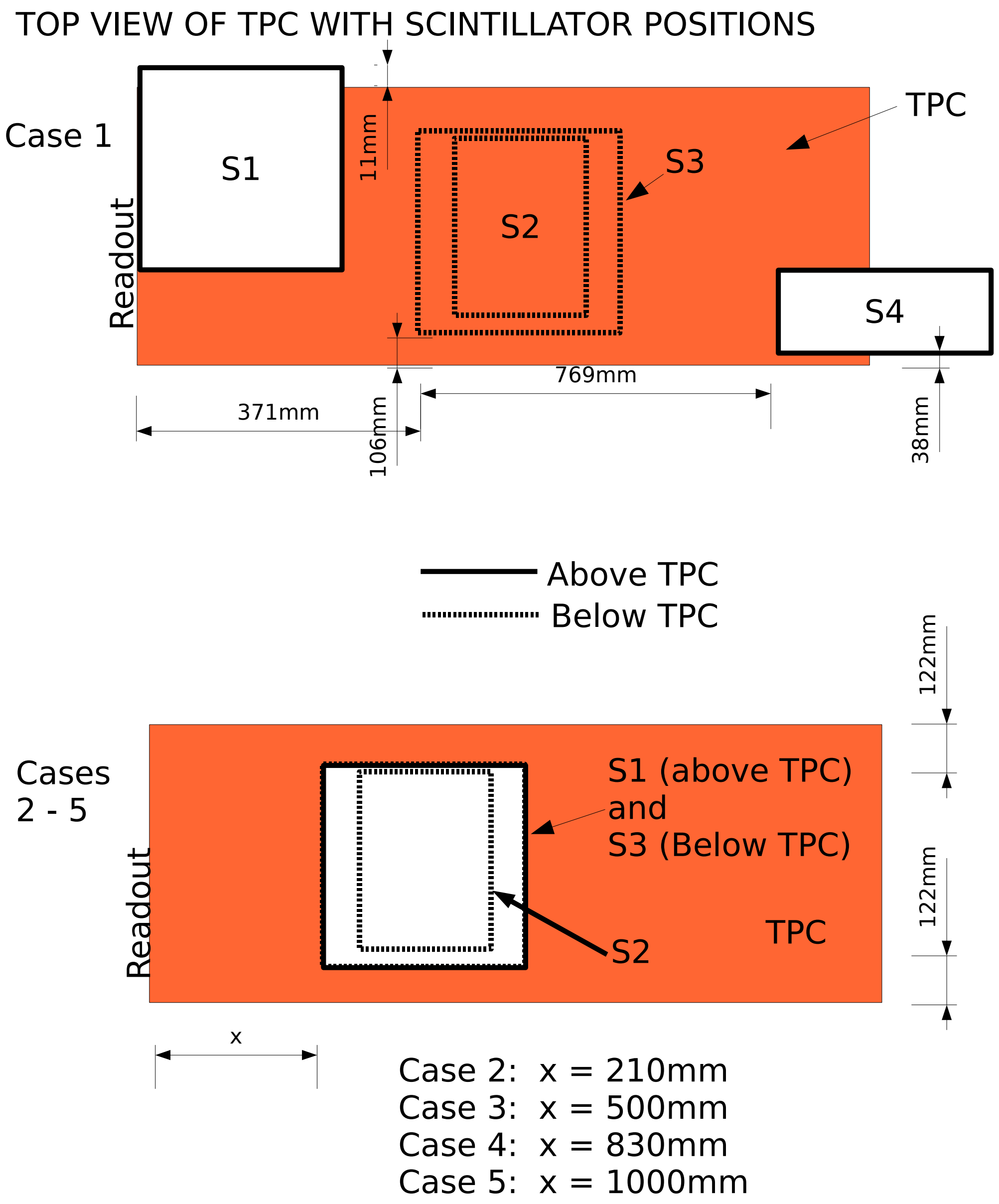

Figure 5.2: The placement of the scintillators with respect to the TPC for 5 different trigger configurations

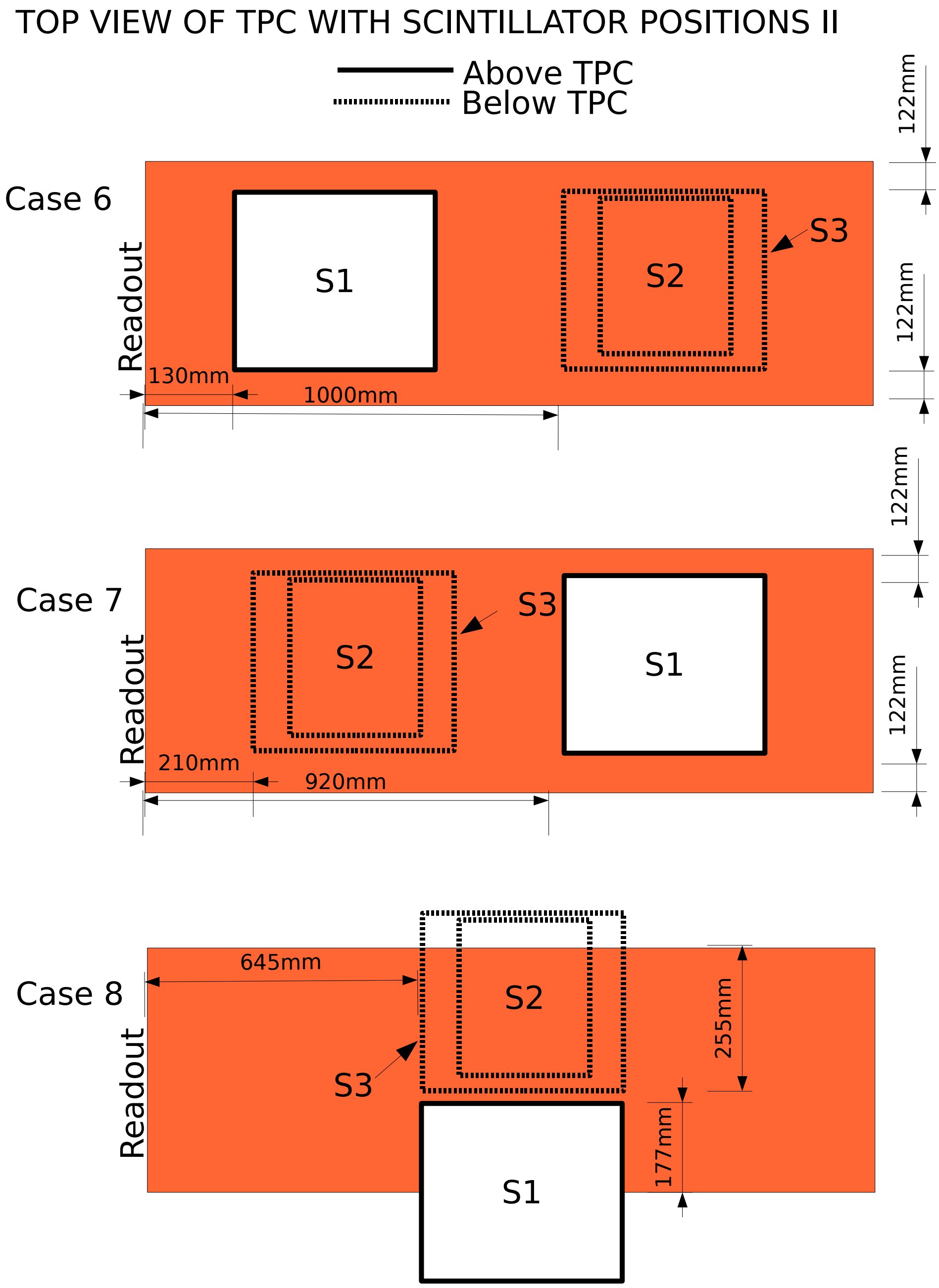

Figure 5.3: The placement of the scintillators with respect to the TPC for 3 different trigger configurations

Chapter 6

Measurement Methods

6.1 Drift Velocity

When a charged particle in an electric field passes through a gas, creating ionization, the electrons and positive ions produced will accelerate in opposite directions, along the electric field lines. The velocity of the electrons is limited by the number of collisions the electron experiences with other gas molecules. To first order, assuming the electron stops after each collision, the average velocity of electrons drifting in a uniform electric field is called the drift velocity (v_d), [18]

$$v_d = \frac{e}{2m} E\tau \tag{6.1}$$

where τ is the mean time between collisions and is, in general, a function of the electric field, E.

Figure 6.1 shows theoretical values for the drift velocity of the relevant gases, as predicted by Magboltz. [17]

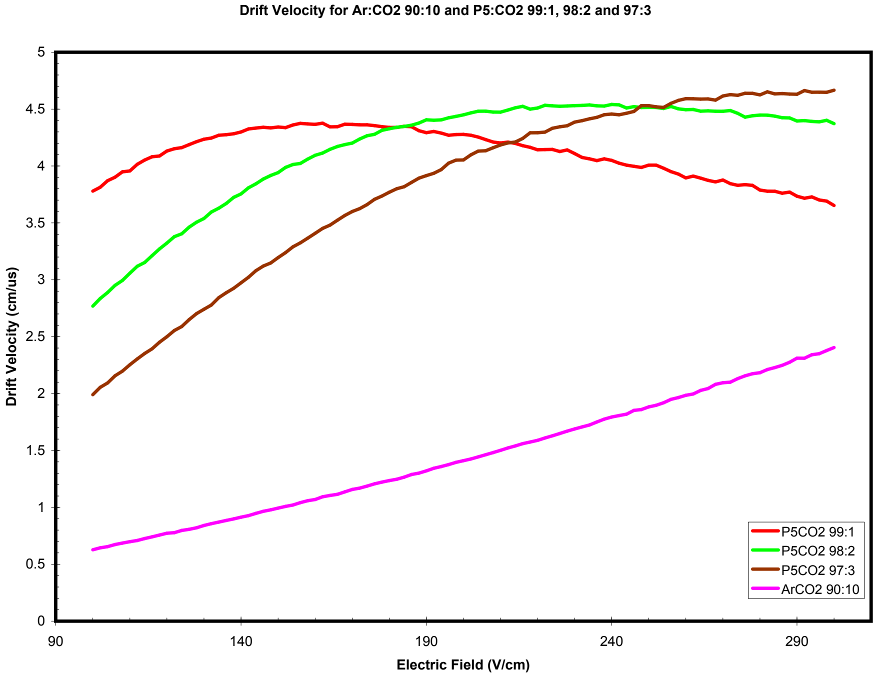

Figure 6.1: The expected drift velocity as a function of electric field for different gases.

To measure the drift velocity in the TPC, the cosmic telescope was aligned to trigger on tracks that cross the central cathode, as shown in cases 1 and 5 in figure 5.2. In the analysis, selecting for events with positive dip angles and high drift times where no signal was measured on the uppermost pads allowed for the isolation of these cathode crossers. Figure 6.2 shows an example of such an event.

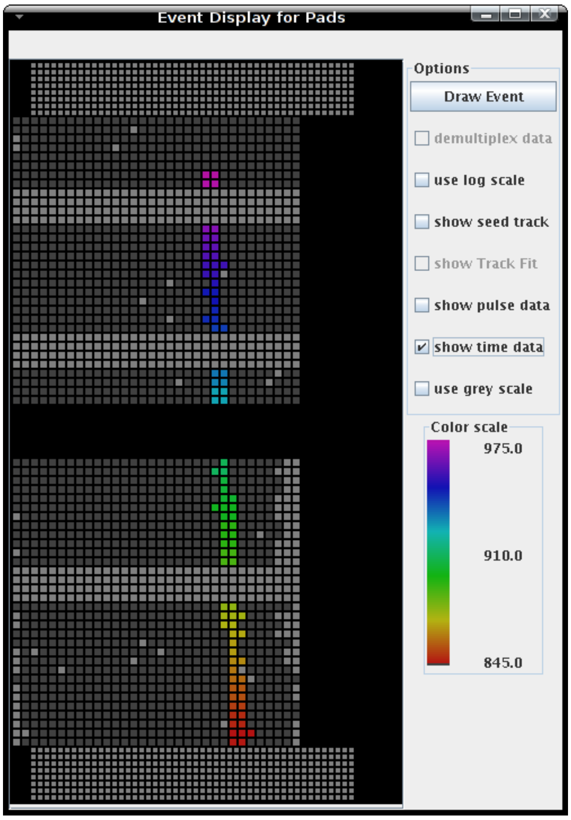

☐ demultiplex data
☐ use log scale
☐ show seed track
☐ show Track Fit
☐ show pulse data
☑ show time data
☐ use grey scale

Figure 6.2: The readout from the TPC is shown above. The track starts below the upper pads and has a positive dip angle, signifying a cosmic ray that came through the central cathode.

For each candidate track found, the drift time of the electrons landing on only the uppermost pads with a signal was used. These drift times were then histogrammed, and the largest time bin with a significant number of entries was used to calculate the drift velocity. The drift distance of the TPC is 1272.5 mm between the central cathode and the top GEM. The electric fields in the region between the uppermost

GEM and the readout pads are much larger than the field in the drift volume, so 0.2 μs was subtracted from the total time to compensate. The drift velocity for each run was then found by dividing the drift distance of the TPC by the corrected time.

6.2 Diffusion

When a cluster of electrons is created in a gas, collisions cause the cluster to diffuse according to a Gaussian Distribution [19] :

$$\frac{dN}{dx} = \frac{N_{tot}}{\sqrt{2\pi D^2 t}} e^{-\frac{x^2}{2D^2 t}} \tag{6.2}$$

where dN/dx is the amount of charge in an element dx at a distance x from the center of the cluster, N_{tot} is the total amount of charge in the cluster and t is the amount of time since the charge cloud was created. The diffusion constant of a gas D is therefore associated with with the standard deviation of the charge cloud: $\sigma_x^2 = D^2 t$. However, for the results presented in this thesis, a definition of the diffusion constant in units of $\mu m/\sqrt{cm}$ is adopted:

$$\sigma^2 = D^2 z \tag{6.3}$$

where z is the distance the charge cloud has travelled in the TPC.

The RMS of the track (σ) is determined for each track from the four-parameter track fit described in Section 4.3.1. The diffusion constant is measured for each run by fitting a linear function to a plot of σ^2 versus t, where t is the drift time of electrons in the gas. To express the diffusion constant in conventional units of $\mu\text{m}/\sqrt{\text{cm}}$ as shown in equation 6.3, multiply the slope by the inverse of the drift velocity, v_d:

$$D^2 = 10^8 \frac{\sigma^2}{t} \cdot \frac{1}{v_d} \tag{6.4}$$

Figure 6.3 shows the diffusion constants calculated by Magboltz for concentrations of $ArCO_2$ and $ArCH_4CO_2$ gas.

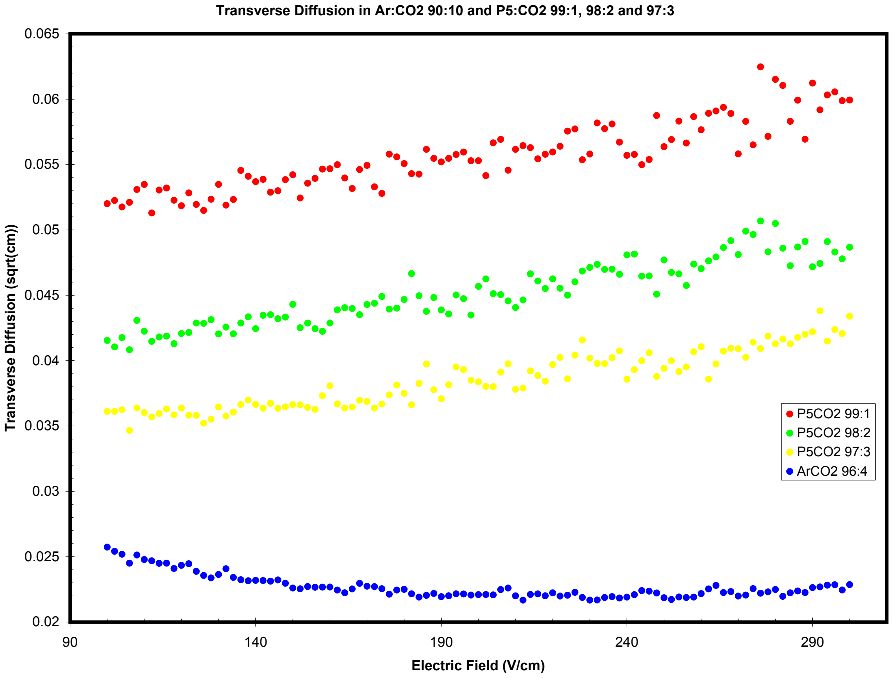

Figure 6.3: The expected transverse diffusion of electrons drifting through gases as a function of electric field as calculated by Magboltz.

6.3 Attachment

The presence of an electronegative gas in the TPC can result in a loss of signal electrons, since some electrons drifting in a charge cluster can attach to electronegative gas molecules. The electrons produced by a track at high drift times will spend more time propagating through the gas than those produced by a track close to the readout, and will therefore have a higher probability of attaching to an electronegative molecule. Consequently, the amount of electronegative gas present in the TPC can be determined by measuring the amount of the charge deposited on the readout as a function of drift time.

Assuming the probability for an electron to be lost is constant throughout the TPC, the loss of electrons from a drifting cluster can be written as

$$\frac{N}{N_0} = e^{-t/\tau_C} \tag{6.5}$$

where t is the drift time of the track and τ_C is the mean lifetime for capture. One potential source of electronegative gas in the TPC is oxygen contamination caused by air leaking into the drift volume from the atmosphere. Figure 6.4 shows the expected amount of attachment for different levels of O_2 contamination in the TPC.

Oxygen contamination caused by air leakage into the inner TPC volume is not the only potential cause of electron attachment. The components used to construct

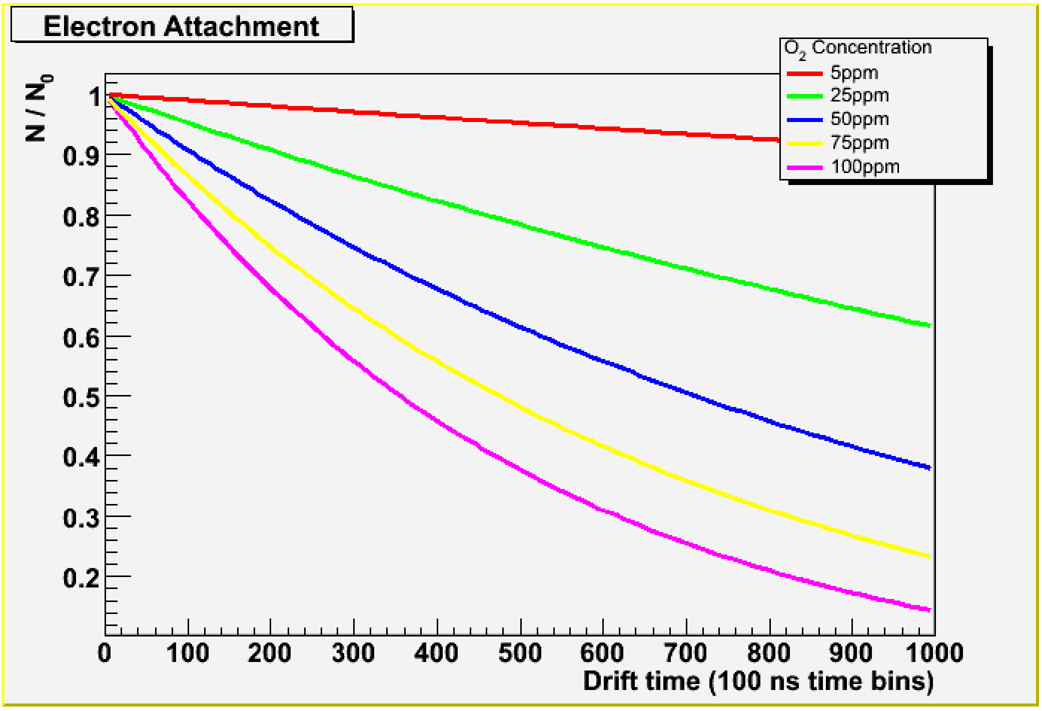

Figure 6.4: The fraction of electrons in a charge cloud being lost to electron capture on O_2 as a function of drift time.

the TPC or its gas system could out-gas an electronegative contaminant into the gas volume, and this signal would be indistinguishable from oxygen contamination. The electron lifetimes that are measured are therefore only compared to an equivalent O_2 concentration, although this may not be the contaminant actually causing the electron attachment.

6.3.1 Energy Loss

The parameter N/N_0 shown in equation 6.2 and figure 6.4 is a poor quantity to choose for studying attachment, since the initial number of electrons in the cluster, N_0, is not independent of track angle. A better quantity to use is the energy loss as a function of projected path length, dE/dx, which quantifies the number of electrons detected by the readout pads per unit track length.

To measure the dE/dx in the TPC, the total charge deposited on every pad row by a single track is histogrammed. The highest 10% of the values are rejected, and the mean of the remaining lowest 90% of the row charges is found. This quantity is then divided by the projected path length of the fitted track over a single pad row, since a highly angled track with respect to the y-axis will cross a longer section of gas in front of each pad, resulting in a larger electron signal being detected.

A track that crosses the TPC directly in front of the readout pads will not lose (almost) any of its electrons to attachment, so it is possible to rewrite equation 6.2.

$$\frac{(dE/dx)_t}{(dE/dx)_{z=0}} = \frac{N}{N_0} = e^{-t/\tau_C} \tag{6.6}$$

Therefore, from the relationship between dE/dx and drift distance, it is possible to extract the attachment coefficients in the gas.

6.3.2 Pressure Effects

The gas gain of a GEM (M) is exponentially proportional to the first Townsend coefficient (α) and the distance (d) between the two charged planes of a GEM [20, 21]:

$$M = e^{\alpha d}. \tag{6.7}$$

Because $\alpha/P \sim E/P$, where E is the electric field between the two planes of the GEM and P is the pressure [21], there is an exponential relationship between gas gain and pressure,

$$M = Ae^{C/P} \tag{6.8}$$

where A and C are constants.

Measuring the electron attachment in the TPC relies on measuring the amplitude of the signal collected by the readout pads, which is in turn affected by the gas gain of the GEMs. The TPC operates at atmospheric pressure, so a change in barometric pressure can cause different gains in the GEMs. In a single run where an attachment coefficient is extracted from the dE/dx as a function of drift distance, it is less important to correct for pressure effects, since the flux of cosmic ray muons through any area of the TPC is constant over time. However, in runs D1 through D4, the scintillators were moved to different drift distances for the different runs. To combine these results, it is important to normalize the measured amplitude to the barometric pressure at the time that the gain was measured.

Figure 6.5 shows the dE/dx in the TPC as a function of inverse barometric pressure, as recorded by an Environment Canada weather station close to the TPC. The pressure varied the most during run D2, (shown on the plot in red) so this run was selected as the baseline for all others. An exponential curve of the form given in 6.8 was fit to the data from run D2, and the dE/dx of each track in all four data sets was scaled according to the pressure measured at that time. The scaling factor was chosen so that all measured dE/dx values were normalized to a standard pressure of 101.3 kPa.

An inspection of figure 6.5 already reveals the occurrence of electron attachment in the TPC. As shown in table 5.3 and figure 5.2, the average drift distance increases as run number increases for data sets D1 through D4. For any given pressure in figure 6.5 the measured dE/dx of a lower numbered data set is larger than the gain of a higher numbered data set, clearly indicating a decrease in dE/dx as drift distance increases. This effect will be treated in more detail in the following chapter.

6.4 Resolution

To ensure that the TPC meets the resolution goals stated in section 2.2.2, it is essential to determine the accuracy to which the position of a track in the TPC is known. Longitudinal resolution is measured in the drift direction, along the z axis of the

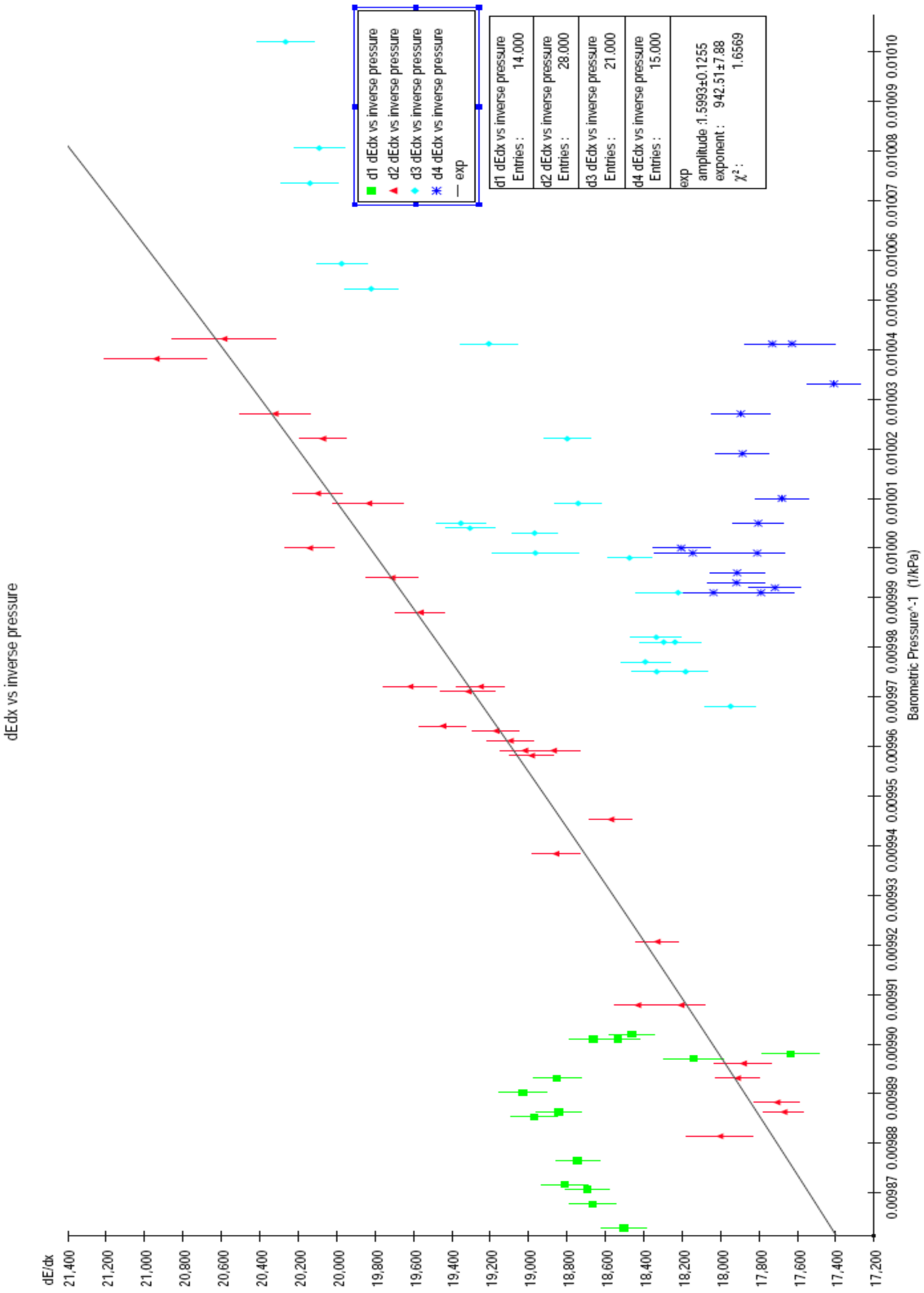

Figure 6.5: The change in gain in the TPC as a function of inverse barometric pressure. The curve fit to the second data set is used to normalize every measured gain to a standard pressure of 101.3 kPa.

TPC. Similarly, transverse resolution is measured perpendicular to the drift direction and the zenith, shown as the x-axis in figure 4.2.

To quantify the resolution of the TPC, the following algorithm is used:

1. Each track is fit using the algorithm described in section 4.3.1.

2. A local fit is performed on the charge deposited in each active pad row, fixing all parameters except x_0 and z_0. The resulting fit parameters are defined as x_0^{row} and z_0^{row}, and represent the fitted center of the charge cluster in each row.

3. For each row, a quantity called the residual (δx in the transverse direction, and δz in the longitudinal direction) is defined, where $\delta x = x_0^{row} - (x_0 - y \tan\phi)$ and $\delta z = z_0^{row} - (z_0 + y \tan\lambda)$. The coordinate y is the vertical distance of the center of the pad row from the center of the TPC, so the values $x_0 - y \tan\phi$ and $z_0 + y \tan\lambda$ are the x and z coordinates of the fitted track on a specific pad row. The residuals δx and δz are therefore the difference between the overall track fit and the local track fit on each pad row.

4. The distributions of δx and δz are histogrammed, and each distribution is fit with a Gaussian function.

5. The resolution of the TPC is determined by the standard deviation of the Gaussian function found in the previous step.

6. Furthermore, a quantity called the bias is defined by the mean of the fitted Gaussian, and is useful for identifying local systematics or anomalies in the TPC.

Apart from measuring the overall resolution of the TPC, it is also useful to look at the resolution and bias as a function of different track parameters. A large bias from tracks originating in a certain area of the TPC volume could indicate distortions in the electric field in that region, amongst other possibilities. In the following section, plots of longitudinal and transverse resolution and bias are shown as a function of the following track parameters:

- x, y and z
- ϕ and $\tan\lambda$

Chapter 7

Results

In this chapter, the results of the tests performed on the prototype TPC are presented. The measured drift velocities and diffusion constants of different gases are shown and compared to theoretical values as a check that the TPC is performing as expected, and that the gas mixtures are correct. Knowing the level of electron attachment in the gases is important to perform accurate dE/dx measurements, as described in section 2.2.2, so the measured amounts of electron attachment are shown. A discussion of why a different system is needed to extract absolute levels of electron attachment from the gases follows. Finally, a thorough investigation into the spatial resolution of the TPC is presented, with emphasis on any systematics that could affect the quality of the measurements.

7.1 Drift Velocity

In order to localize tracks in a time projection chamber, the drift velocity of the gas must be known. Table 7.1 shows the drift velocities measured by data sets A1-A4, B1-B3 and D4. The data sets not included in this sample are those that did not have a scintillator above the central cathode, thereby prohibiting a measurement of drift velocity using the drift time of cathode crossing events. Figure 7.1 shows the distribution of the drift times associated with the uppermost pads in a track for data set D4, in the case where the incident particle crossed through the central cathode.

The errors on the drift velocities in table 7.1 arise from the uncertainty in selecting the uppermost time bin. An inspection of table 7.1 seems to indicate that the drift velocities of $ArCO_2$ gas are all significantly higher than the expected drift velocities calculated by Magboltz. The expected drift velocities quoted in table 7.1 are for a concentration of exactly 90.00 parts Ar and 10.00 parts CO_2. Figure 7.2 shows the variation of expected drift velocity as a function of argon concentration in $ArCO_2$. It can be observed that an increase of 0.5% in argon concentration is sufficient to produce drift velocities similar to those seen in table 7.1. However, at a flow rate on the order of 1 l/min, the relative concentrations of Argon and CO_2 in the gas were known to 0.1%, so the discrepancy cannot be attributed to an uncertainty in the gas. It is more likely that Magboltz underestimates the drift velocity of $ArCO_2$ gas at these concentrations.

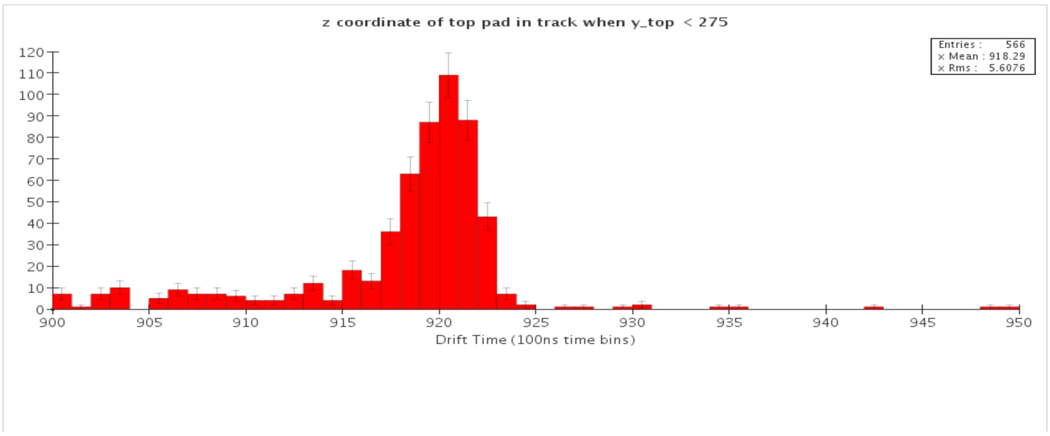

Figure 7.1: The drift times of tracks that crossed the central cathode in data set D4.

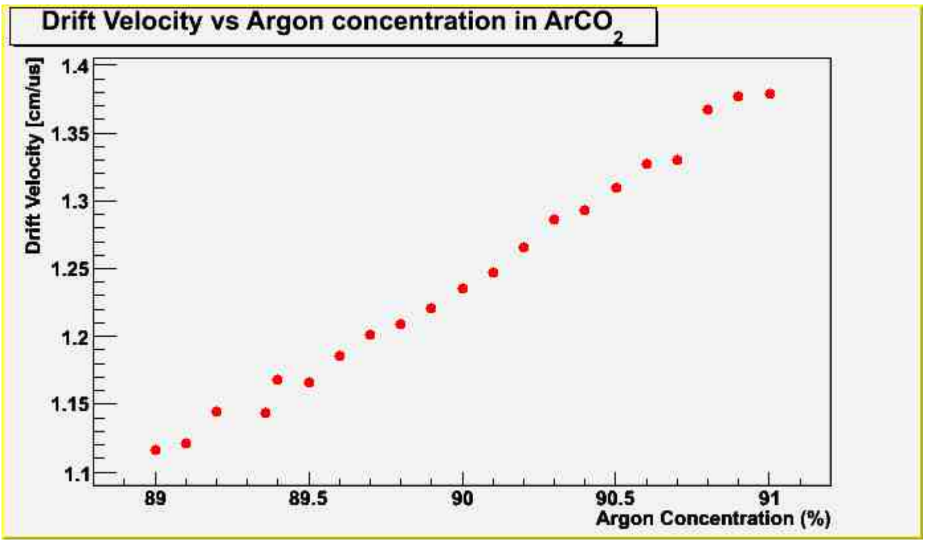

Figure 7.2: The drift velocity calculated by Magboltz of electrons in varying concentrations of $ArCO_2$. All values correspond to an electric field of 180V/cm.

Data Set	v_d **(Magboltz)** mm/μs	v_d **(measured)** mm/μs
ArCO$_2$		
A1	12.30	13.05 ± 0.02
A2	12.30	13.31 ± 0.02
A3	12.30	13.02 ± 0.02
A4	12.30	12.88 ± 0.02
D4	12.30	13.83 ± 0.02
ArCH$_4$CO$_2$		
B1	40.65	40.53 ± 0.18
B2	42.85	43.14 ± 0.21
B3	36.35	36.25 ± 0.15
Data Set	v_d **(Input to MC)** mm/μs	v_d **(measured)** mm/μs
ArCO$_2$		
(A1-A4)MC	13.1	13.10 ± 0.02
D4MC	13.1	13.21 ± 0.02
ArCH$_4$CO$_2$		
B1MC	40.0	39.94 ± 0.18
B2MC	44.0	43.86 ± 0.22
B3MC	36.0	36.02 ± 0.15

Table 7.1: The expected and measured drift velocities in ArCO$_2$ and ArCH$_4$CO$_2$ gas.

Interestingly, the expected and measured ArCH$_4$CO$_2$ drift velocities appear much more consistent than the ArCO$_2$ values. Furthermore, except for data set MCD4, the drift velocities measured from the Monte Carlo data sets are all consistent with the input values, demonstrating that the method used to determine the drift velocity of a TPC gas is valid.

For all data sets, the drift velocity has been measured to a degree of precision high enough to allow all of the other measurements to be performed without significant drift velocity contribution to the error. This measurement will need to be performed with a similar precision in the full-scale modules.

7.2 Diffusion

Although the successful operation of the TPCs in the ND280m detector does not require knowing the diffusion constant of the drift gas to a high degree of precision, measuring the diffusion constant of the gas serves as a check that the prototype TPC is operating properly. Below, figure 7.3 shows the fit results of the parameter σ^2 for each selected track in data sets A1-A4 as a function of drift distance. As demonstrated in section 6.2, the slope of this distribution yields the diffusion constant for the gas. The data points in figures 7.4 through 7.6 show the mean σ^2 for an interval of time bins, and the slope of the linear functions fit to each data set represent the measured diffusion constants. Table 7.2 shows a summary of the parameters of all of the fitted functions in figures 7.4 through 7.6, and tables 7.3 and 7.4 list the corresponding diffusion constants for the gases.

At intermediate drift times, the diffusion plots in figures 7.4 and 7.6 show measured data but no Monte Carlo data in data sets A and B. This occurs because of the orientation of the uppermost scintillator that was used for the cosmic trigger in these data sets. (See scintillator S1 in case 1 of figure 5.2.) The light guide of this scintillator extended down the length of the TPC, and it was found that particles passing through the light guide also caused the scintillator to fire. If the light guide were inactive, so

Data Set	**p0**	**p1**	χ^2/ndf
Figure 7.4			
A1-A4	0.020 ± 0.013	(5.32 ± 0.02) $\times 10^{-3}$	824.1/39
(A1-A4)MC	0.303 ± 0.013	(4.28 ± 0.02) $\times 10^{-3}$	50.1/16
Figure 7.5			
D1-D4	0.276 ± 0.006	(5.53 ± 0.01) $\times 10^{-3}$	1057/50
(D1-D4)MC	0.265 ± 0.007	(5.08 ± 0.01) $\times 10^{-3}$	124.6/43
Figure 7.6			
B1	0.384 ± 0.035	(5.87 ± 0.03) $\times 10^{-2}$	118.5/30
B1MC	0.391 ± 0.028	(5.42 ± 0.02) $\times 10^{-2}$	71.1/14
B2	1.097 ± 0.064	(8.94 ± 0.05) $\times 10^{-2}$	173.2/20
B2MC	0.934 ± 0.037	(8.58 ± 0.03) $\times 10^{-2}$	102.4/14
B3	0.415 ± 0.029	(4.08 ± 0.02) $\times 10^{-2}$	97.1/30
BMC	0.267 ± 0.025	(3.61 ± 0.02) $\times 10^{-2}$	29.8/15

Table 7.2: The fit parameters of the linear functions in figures 7.4 through 7.6

Data Set	$\mathbf{D}_{input}$ $[\mu m/\sqrt(cm)]$	$\mathbf{D}_{measured}$ $[\mu m/\sqrt(cm)]$	Defocussing [mm]
ArCO$_2$			
(A1-A4)MC	220	181 ± 33	1.74 ± 0.12
(D1-D4)MC	220	189 ± 30	1.63 ± 0.24
ArCH$_4$CO$_2$			
B1MC	400	368 ± 16	1.98 ± 0.22
B2MC	500	442 ± 13	3.05 ± 0.19
B3MC	350	317 ± 11	1.63 ± 0.24

Table 7.3: The input and measured diffusion constants (D) for Monte Carlo data sets.

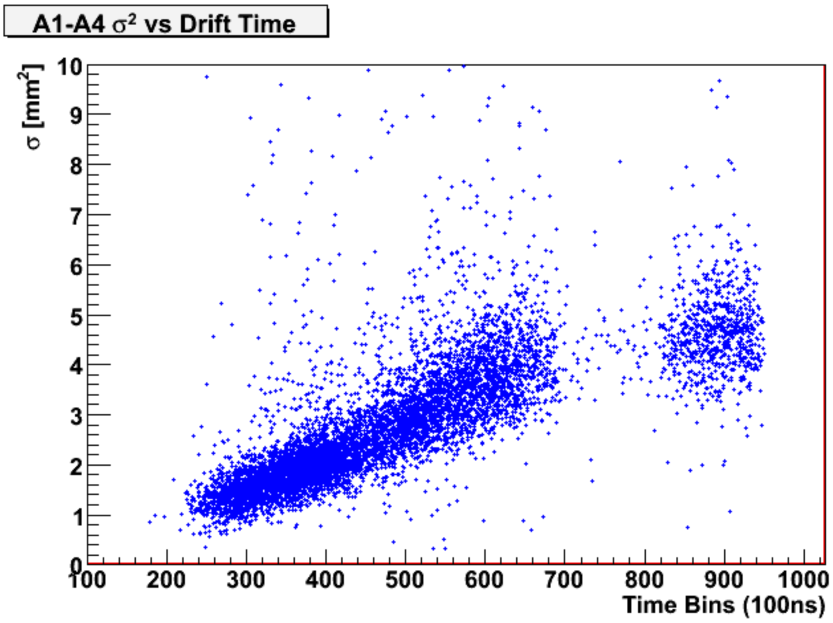

Figure 7.3: A plot showing σ for each track that was selected in data sets A1-A4.

that only the paddle of the scintillator registered the passage of cosmic ray muons, then the distributions of measured data as a function of drift time would be more similar to the Monte Carlo.

Although the slopes of the σ^2 versus drift time plots shown in figures 7.4 through 7.6 are similar between the Monte Carlo data and the measured data, thereby giving rise to similar diffusion constants, a vertical offset can be observed between the Monte Carlo and measured data. In all cases, the best-fit line to the measured data lies at larger values of σ^2 than the best fit line to the Monte Carlo data. This effect can be parameterized by examining the width of tracks created directly in front of the GEMs. This width, known as the *defocussing* can be measured by taking the square

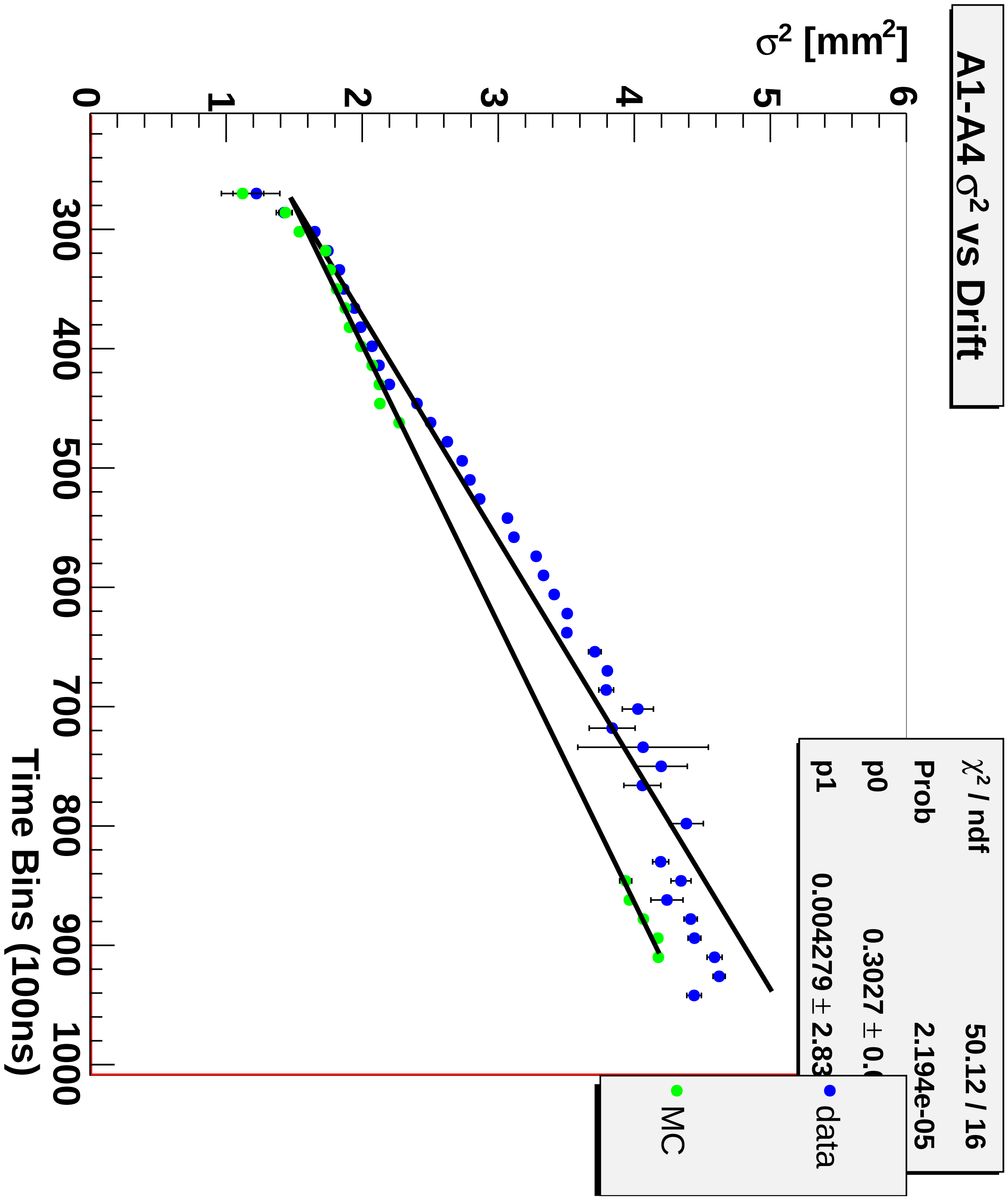

Figure 7.4: σ^2 as a function of drift time for data sets A1-A4. (ArCO$_2$ gas)

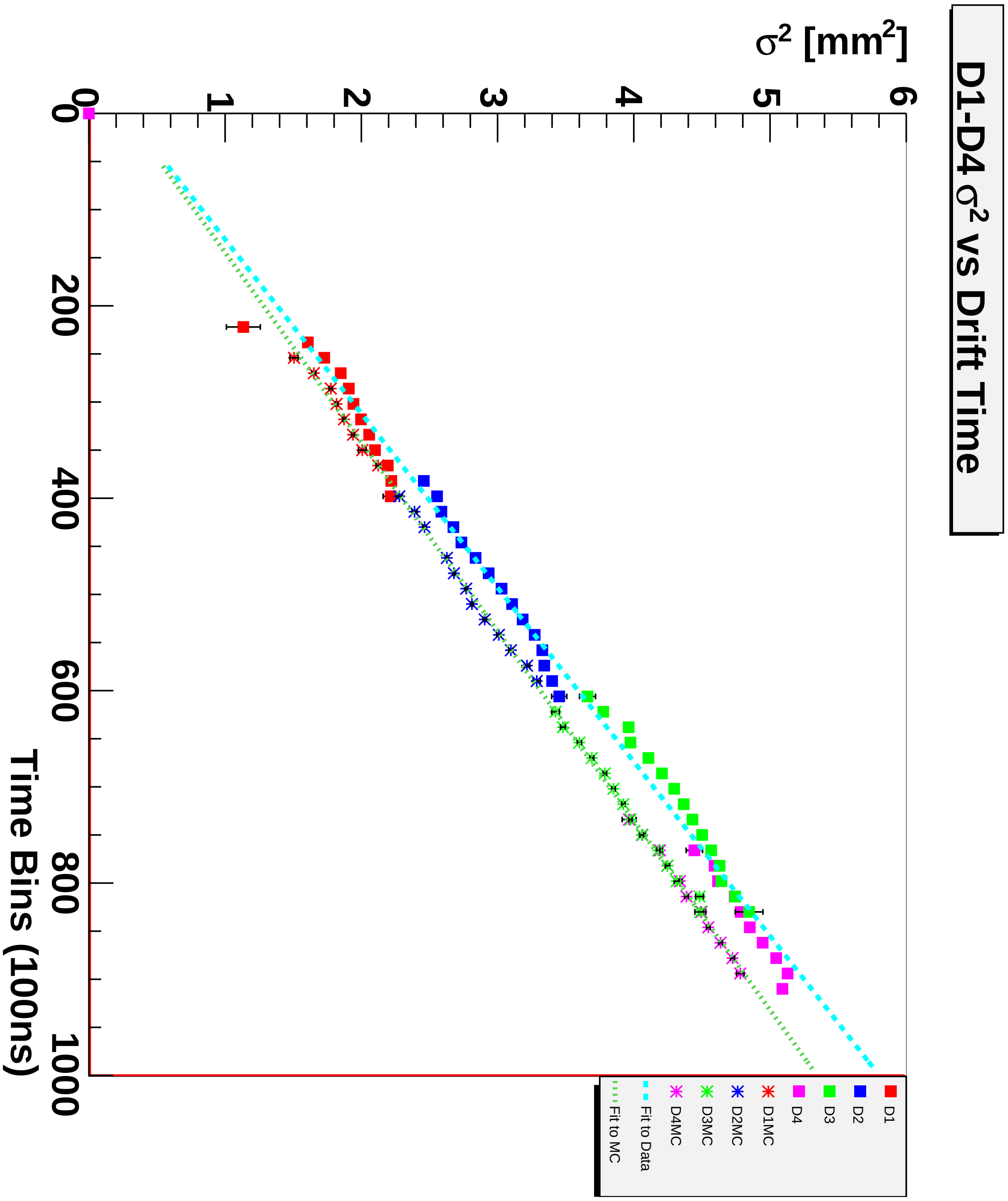

Figure 7.5: σ^2 as a function of drift time for data sets D1-D4. ($ArCO_2$ gas)

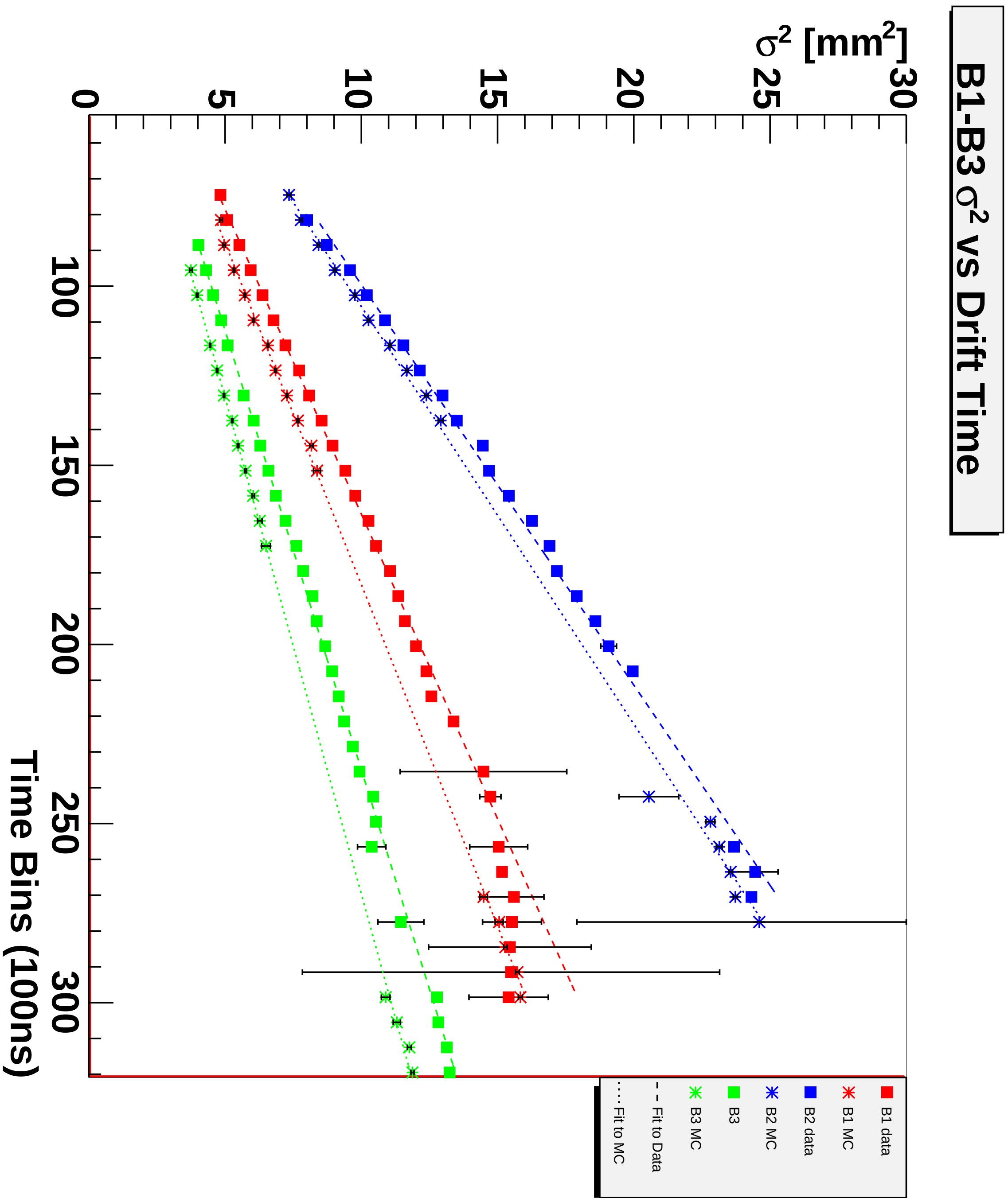

Figure 7.6: σ^2 as a function of drift time for data sets B1-B3. ($ArCH_4CO_2$ gas)

Data Set	$\mathbf{D}_{expected}$ $[\mu m/\sqrt(cm)]$	$\mathbf{D}_{measured}$ $[\mu m/\sqrt(cm)]$	Defocussing [mm]
$ArCO_2$			
A1-A4	225	244 ± 35	0.45 ± 0.46
D1-D4	225	232 ± 34	1.66 ± 0.06
$ArCH_4CO_2$			
B1	423	413 ± 15	1.96 ± 0.28
B2	480	514 ± 14	3.31 ± 0.30
B3	380	370 ± 18	1.74 ± 0.12

Table 7.4: The expected and measured diffusion constants (D) for different data sets. Expected diffusion constants for measured data were calculated by Magboltz. Measured diffusion constants presented here have been scaled by $D^{MC}_{expected}/D^{MC}_{measured}$.

root of the y-intercept of the plot of σ^2 versus drift time, and is a measure of the spreading of charge that occurs in the GEMs. The measured defocussing, shown in table 7.3, is consistent with the Monte Carlo in all cases except for data set A. There are some non-linear effects in data set A that cause a larger slope to be measured, thereby decreasing the diffusion constant. These effects are discussed in detail below.

The statistical errors associated with the diffusion constants in table 7.3 are calculated from the uncertainty in the slope of σ^2 vs time and the error on the drift velocity. It is a known effect for TPCs with pad readout that the fitted width of a track, σ, is sensitive to the choice of a noise parameter, p_{noise}, which is the probability of a noise signal to be present in a particular pad in a row.[15] For $p_{noise} = 0.01$ as was used in this analysis, the authors in reference [15] found that measured diffusion constants were underestimated by ~10% from the known values in Monte Carlo simulations. A slightly larger effect is observed in the $ArCO_2$ Monte Carlo diffusion constants quoted in table 7.3, where the measured diffusion constants from data sets (A1-A4)MC and (D1-D4)MC underestimate the input diffusion constants by factors of 1.22 and 1.16 respectively. The $ArCO_2$ diffusion constants shown in table 7.4 have therefore been scaled up by a factor of $D^{MC}_{expected}/D^{MC}_{measured}$, where D^{MC} is the Monte Carlo diffusion constant corresponding to each particular $ArCO_2$ data set.

In the lower half of table 7.3 the diffusion constants measured for Monte Carlo $ArCH_4CO_2$ data are shown. In this case, as expected, the diffusion constants measured for Monte Carlo data sets B1MC, B2MC and B3MC underestimate the input values by factors of 1.09, 1.13 and 1.11 respectively. The measured diffusion constants shown in table 7.4 have therefore been appropriately scaled up by these factors.

From table 7.2, which shows the fitted parameters for all of the slopes in figures 7.4 through 7.6, it can be observed that there is a very large χ^2/ndf value for most of the fits, especially for $ArCO_2$ gas. There are some non-linearities in the plots of σ versus drift distance, and due to the large amount of statistics, the error bars are quite small. The non-linear effects cause some of the data points to be many standard deviations away from the fitted function, increasing the χ^2/ndf of the fit. Although present in every figure, the non-linear effects are most visible in figure 7.4, which shows that the values of σ measured at intermediate drift times are larger than a linear trend would predict.

The non-linearity in the figures could arise from distortions in the electric field.

(It will be shown in section 7.4 below that there are some significant distortions in the electric field.) If different regions of the charge cloud are displaced by different amounts in a direction other than the drift direction, a larger σ will result from the track fit. This effect would be similar in data sets A and B, since they share the same trigger configuration, but more apparent in data set A, because of the smaller diffusion constant.

In terms of the diffusion, it is not necessary to understand these effects to a more precise degree, since successful operation of the TPCs in the ND280m detector is not very sensitive to the diffusion constant at this level of precision.

7.3 Attachment

The amount of electron attachment measured in $ArCO_2$ gas can be seen from the fitted functions in figures 7.7 through 7.10 below. Figure 7.9 shows the measured amount of electron attachment in the Monte Carlo data. Table 7.5 summarizes the measured attachments for all of the data sets, including the expected values for the Monte Carlo data.

It is apparent from the measured attachment distributions that the dependence of dE/dx on drift time is not purely exponential, contrary to expectation. There is some structure in these plots that is not present in the Monte Carlo sample, and is important to understand to extract correct attachment coefficients from the distri-

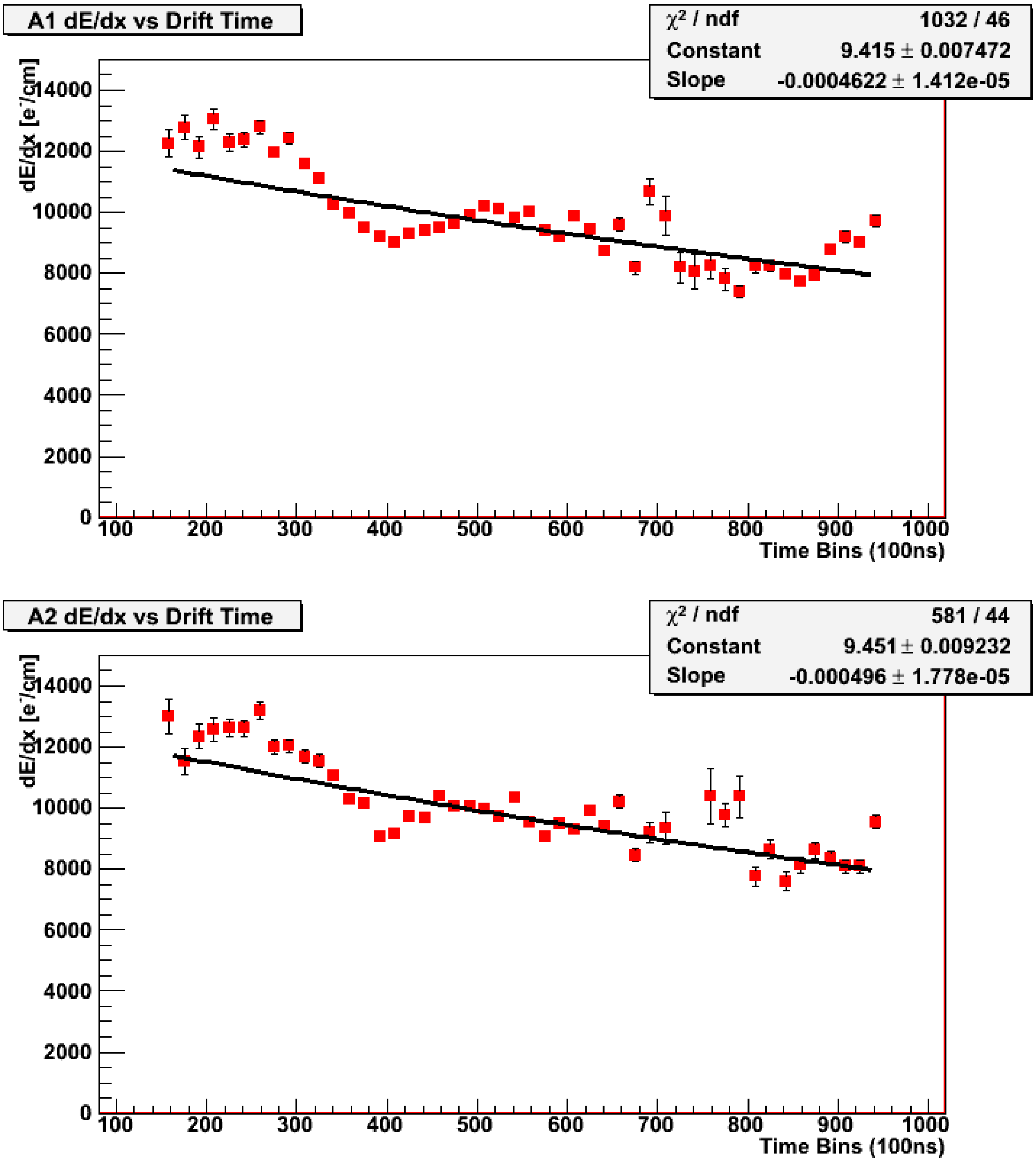

Figure 7.7: The electron attachment of data sets A1 and A2. (ArCO$_2$ gas)

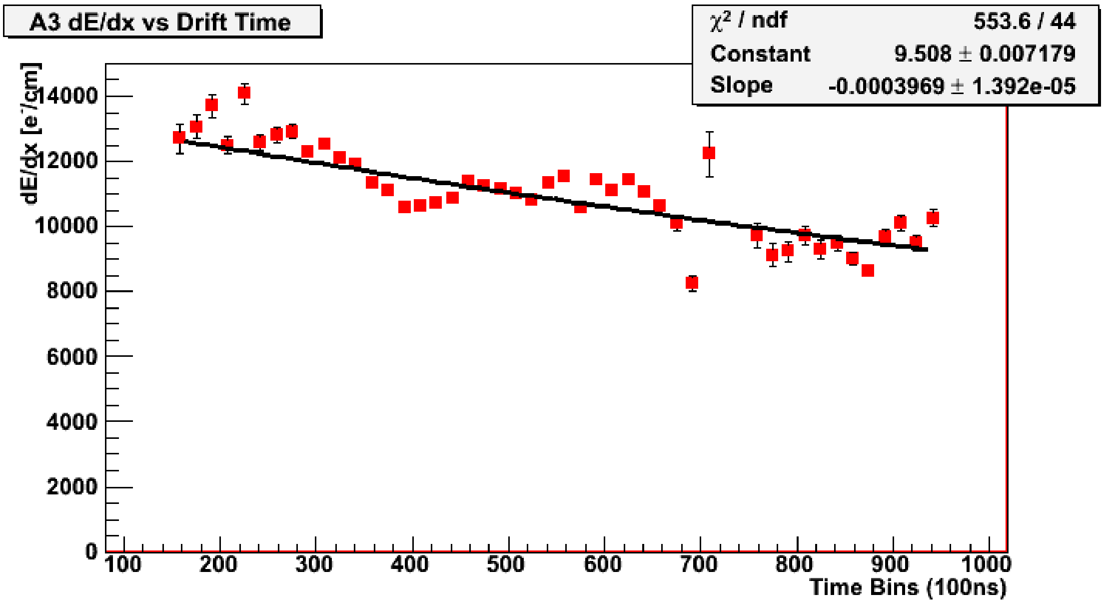

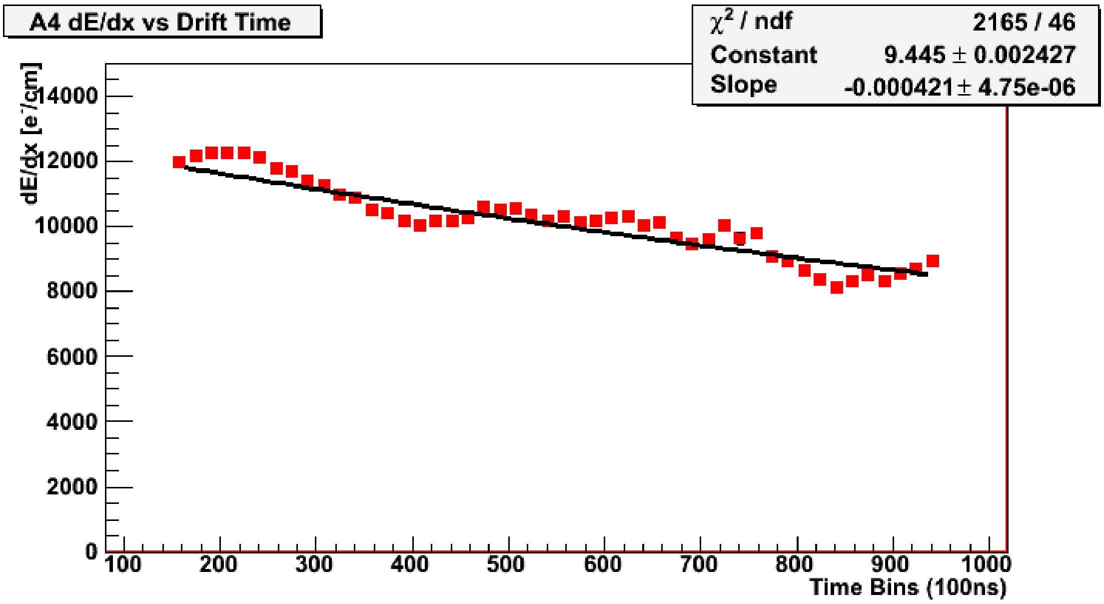

Figure 7.8: The electron attachment of data sets A3 and A4 (ArCO$_2$ gas)

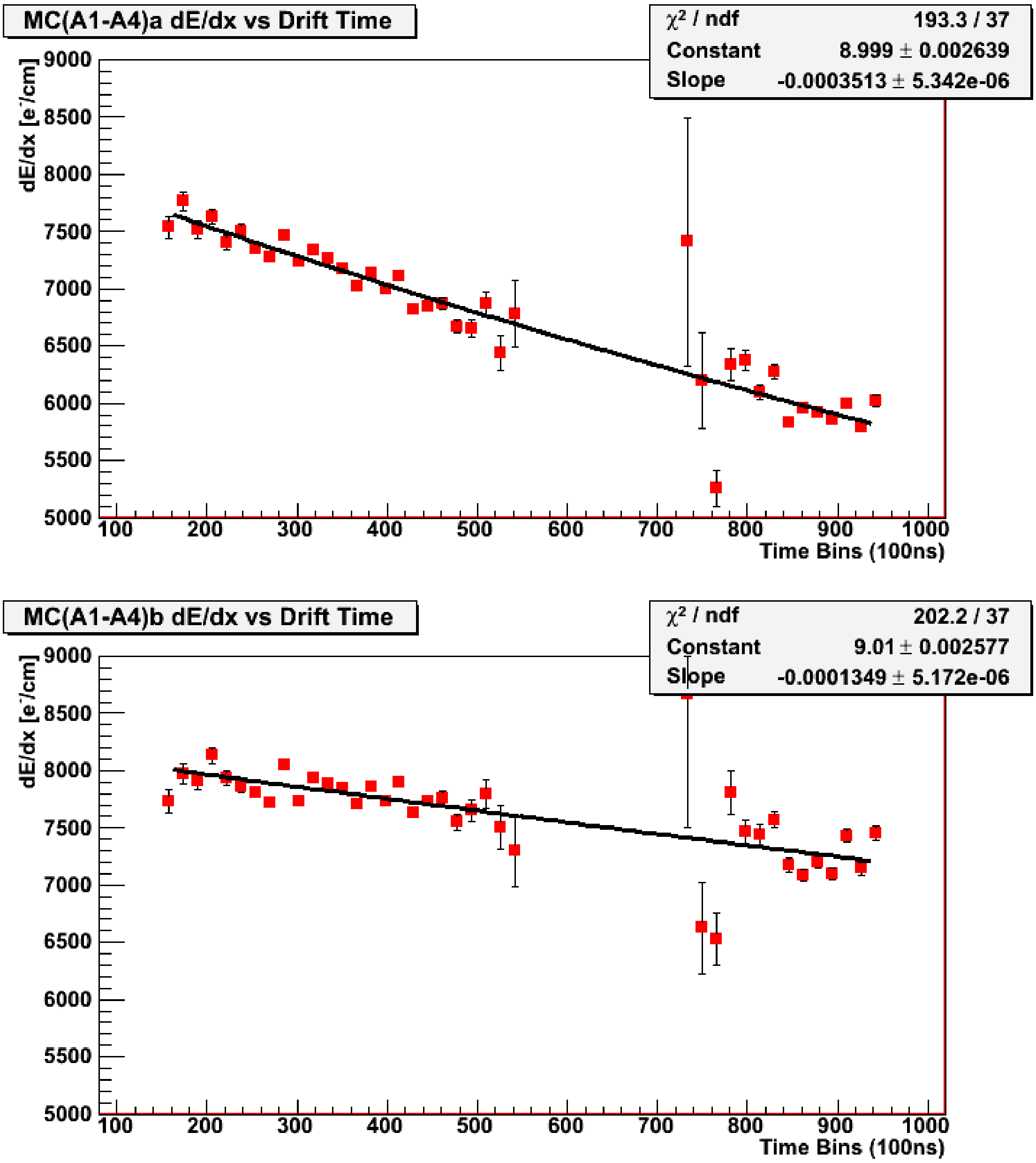

Figure 7.9: The electron attachment of two different MC simulations of data sets A1 through A4.(ArCO$_2$ gas)

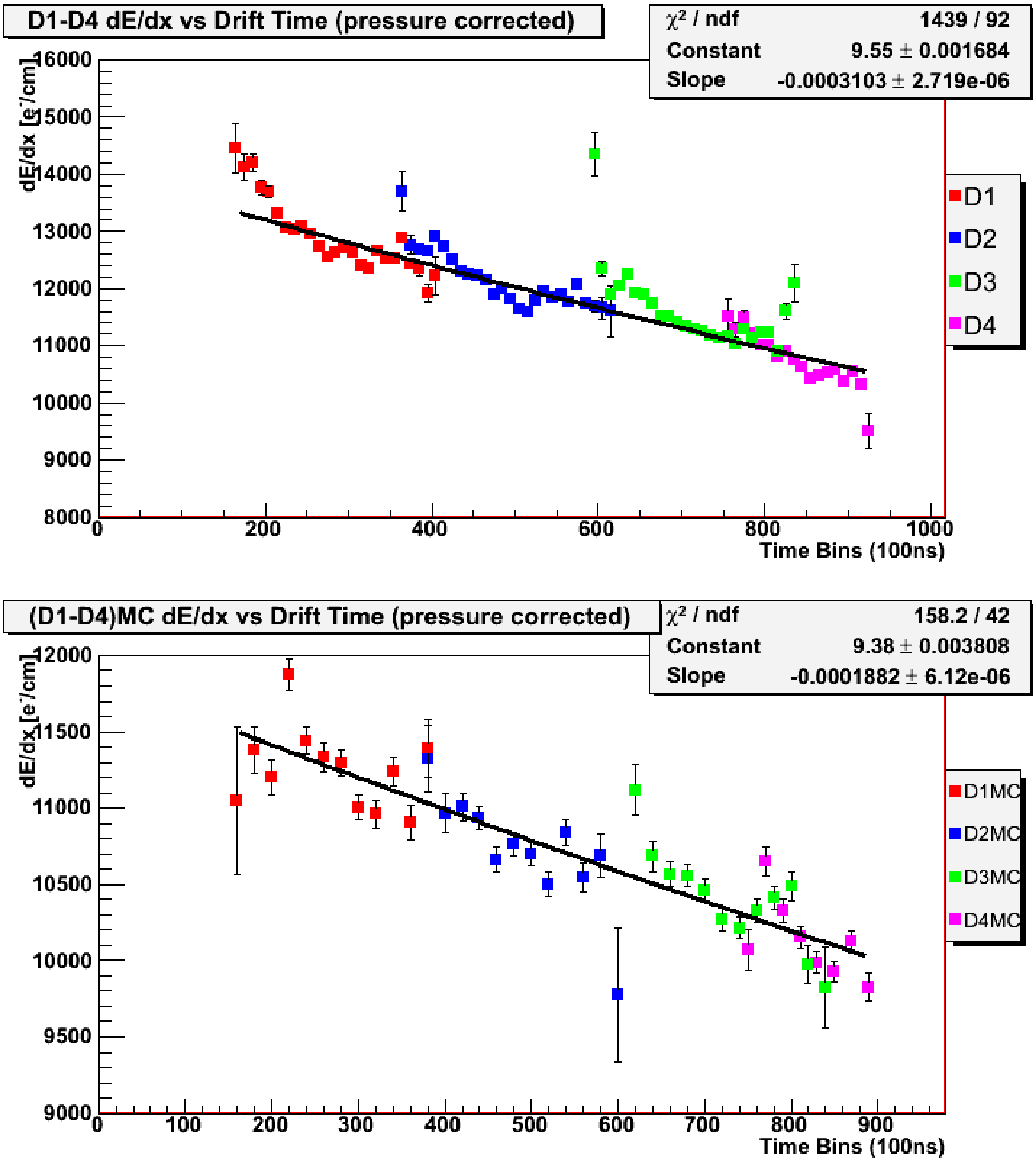

Figure 7.10: The electron attachment of data sets D1 through D4.(ArCO$_2$ gas)

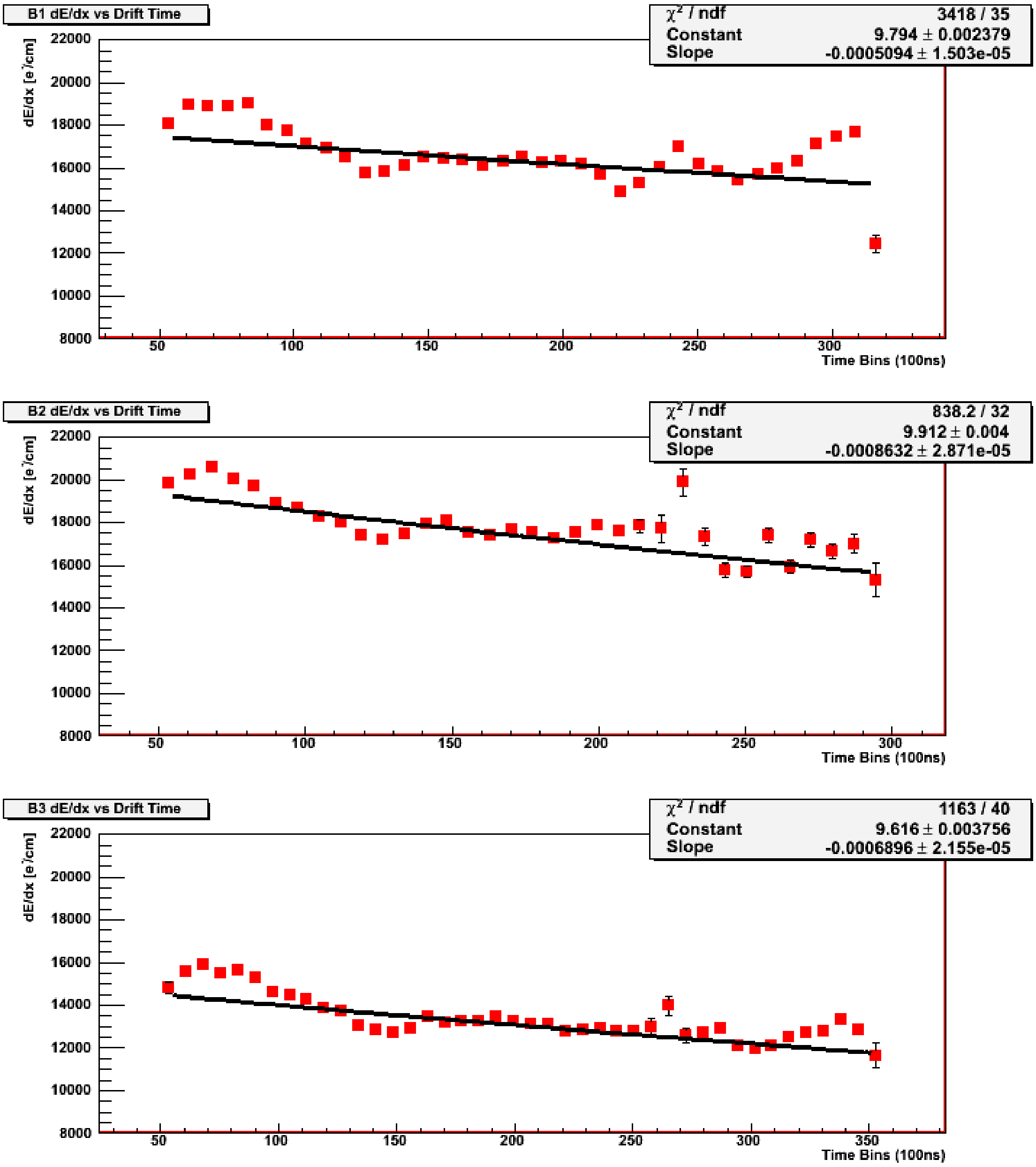

Figure 7.11: The electron attachment of data sets B1, B2 and B3 (Ar$CH_4$$CO_2$ gas)

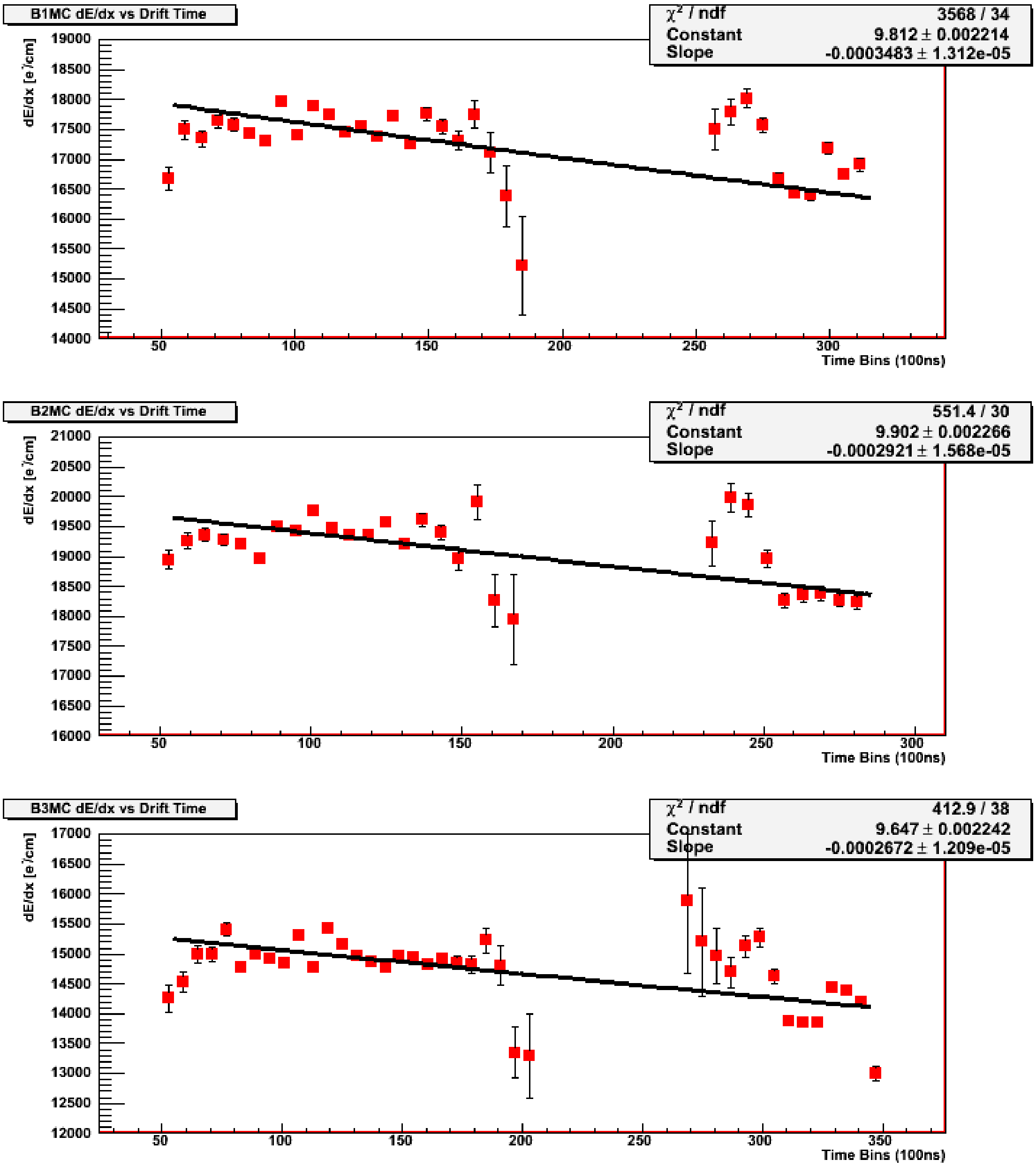

Figure 7.12: The electron attachment of two different MC simulations of data sets B1, B2 and B3.

Data Set	$\tau_{expected}$ μs	$\tau_{measured}$ μs
ArCO$_2$		
A1	-	216.3 ± 6.6
A2	-	201.6 ± 7.2
A3	-	251.9 ± 8.8
A4	-	237.5 ± 2.6
MC(A1-A4)a	200	284.6 ± 4.3
MC(A1-A4)b	500	741.1 ± 28.4
D1-D4	-	322.2 ± 2.8
(D1-D4)MC	400	531.5 ± 17.2
ArCH$_4$CO$_2$		
B1	-	196.2 ± 5.7
B1MC	200	287.1± 10.9
B2	-	115.8 ± 3.9
B2MC	200	342.3 ± 18.4
B3	-	145.0 ± 4.5
B3MC	200	374.3 ± 16.9

Table 7.5: The expected and measured electron lifetimes in ArCO$_2$ and ArCH$_4$CO$_2$ gas.

butions. The shaping time of the charge-sensitive amplifier (190ns FWHM) is short when compared with the spread in arrival time of the charge cloud, which has an effect on the amplitude of the signal, and therefore the measured attachment. The effects of a short shaping time on the measured attachment coefficients are presented below.

Also, the measured Monte Carlo attachment coefficients are all notably larger than the input coefficients, and there is some scatter about the exponential fit, especially visible in data set B. These effects highlight the fact that the shaping time of the electronics is not yet well modelled, and more work will be needed to fully understand the effects of electronegative gas contamination in the TPC.

7.3.1 Shaping Time Effects

A diagram of the readout electronics, presented in section 3.3.2, shows that the charge-sensitive amplifier is placed after the inverter card. This amplifier integrates the charge collected on the pads, and shapes the charge with a 4^{th} order semi-Gaussian pulse shaper that has a shaping time of 190ns at FWHM. [22] The output of a pulse shaper with a peaking time shorter than the rise time of the input signal will be smaller in amplitude, since not all of the signal is being effectively sampled.

The width of an input signal depends on two factors: the amount that the charge cluster has diffused in the longitudinal direction before sampling, and the dip angle of the track, since a more angled track will spread charge over a larger area in the drift distance than a vertical track will. Magboltz calculates the longitudinal diffusion in $ArCO_2$ gas to be $250\mu m/\sqrt{cm}$, so knowing the dip angle of a track it is possible to calculate the expected standard deviation of the charge cloud for tracks at different angles and drift distances. Figure 7.13 shows this quantity, as well as the pulse-shaping time of the readout.

Figure 7.13 shows that the longitudinal standard deviation of the signal is expected to exceed the shaping time of the TPC for most tracks through the TPC, and shows that the amplitude of a pulse measured by the readout will be dependent not only on

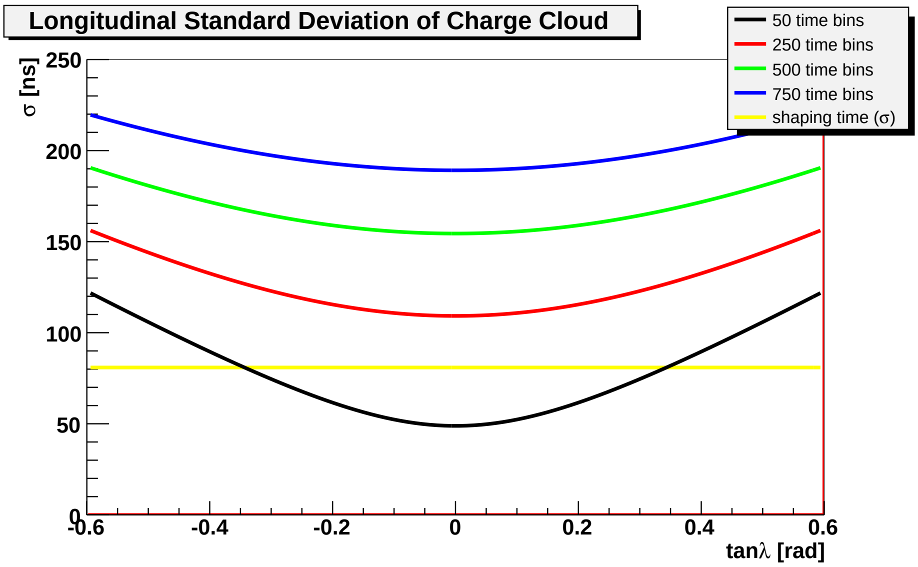

Figure 7.13: The expected standard deviation of the charge cloud in the longitudinal direction as a function of angle for different drift distances. The yellow line shows the shaping time of the electronics.

the angle of a track, but the drift distance as well. Since the measured attachment is therefore dependent on drift distance and track angle, it is challenging to dis-entangle these two effects.

It is useful, however, to examine further the effects of the shaping time, to ensure that they are correctly understood. To quantify the dependence of pulse height on dip angle, the amplitude of charge clouds originating at a fixed drift distance is studied for different dip angles. If the rise time of a pulse is faster than the shaping time of the electronics, there should be no noticeable dependence of pulse height on dip angle. Figure 7.14 shows the pulse heights measured for different angles, where each charge cloud drifted a distance of between 475 and 500 time bins in the TPC. Figure 7.14

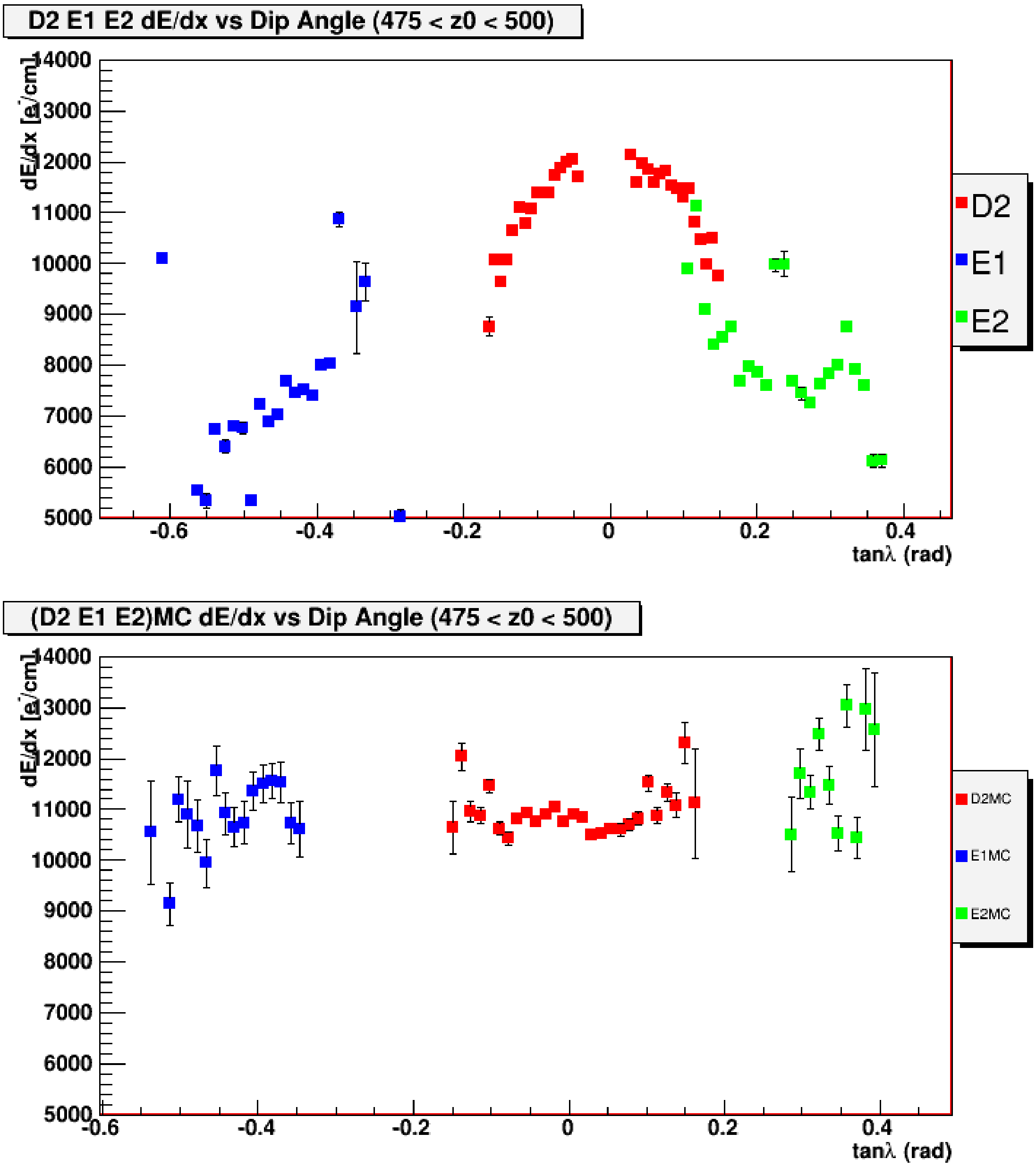

Figure 7.14: dE/dx as a function of angle for a fixed drift time of 475< t_{drift} <500.

shows a clear dependence of pulse height on angle, not predicted by the Monte Carlo. This effect, coupled with the effect of pulse height on drift distance, is a prime cause of the complicated attachment distributions shown at the beginning of this section. The combination of these two effects effectively prevents an accurate measurement of any attachment in the TPC using the current data. In ND280m, however, the fullsize modules have been designed with custom electronics that have adjustable shaping times. A shaping time can therefore be selected that is longer than the arrival time of the charge cloud from all tracks in the detector, allowing an accurate measurement of any electronegative gas contamination in the drift volume.

7.4 Resolution and Bias

As shown in section 6.4, the total resolution of the TPC is determined by the standard deviation of a Gaussian fit to the distribution of residuals from tracks in the TPC. In this section, the overall resolution of the prototype TPC is presented, and the resolution is studied as a function of drift distance, y coordinate, z coordinate, azimuthal angle, and dip angle. Due to the similarities in construction between the prototype and the full-scale TPCs in the ND280m detector, measuring the resolution of the prototype gives an indication of the resolution that will be achievable in the full-scale modules, while searching for biases in the prototype data can uncover systematic errors that will need to be understood and corrected in the ND280m TPCs.

7.4.1 Overall TPC Resolution

Below, figures 7.15 and 7.16 show the transverse residual distributions for $ArCO_2$ and $ArCH_4CO_2$ data sets respectively, while figures 7.17 and 7.18 show the longitudinal residual distributions for both gases. On the upper right corner of every histogram are the parameters of the fitted Gaussian corresponding to the measured bias and resolution of the TPC. Table 7.6 summarizes the measured resolutions for all the data sets.

Data Set	**Transverse Resolution [mm]**	**Longitudinal Resolution [mm]**
$ArCO_2$		
A1-A4	0.817 ± 0.001	1.10 ± 0.01
(A1-A4)MC	0.763 ± 0.002	0.93 ± 0.01
D1-D4	0.750 ± 0.001	0.85 ± 0.01
(D1-D4)MC	0.711 ± 0.001	0.65 ± 0.01
$ArCH_4CO_2$		
B1	0.850 ± 0.001	1.67 ± 0.02
B1MC	0.813 ± 0.002	1.91 ± 0.02
B2	0.899 ± 0.003	1.76 ± 0.02
B2MC	0.898 ± 0.002	2.01 ± 0.02
B3	0.829 ± 0.002	1.57 ± 0.02
B3MC	0.773 ± 0.002	1.57 ± 0.02

Table 7.6: The measured TPC resolutions in $ArCO_2$ and $ArCH_4CO_2$ gas.

Comparing the transverse resolutions measured in data sets A, B and D to the Monte Carlo predictions reveals that apart from data set B2, the measured resolutions are slightly larger than the predicted values by a factor ranging from 4% to 7%. Since the Monte Carlo resolution has been used for momentum resolution studies,

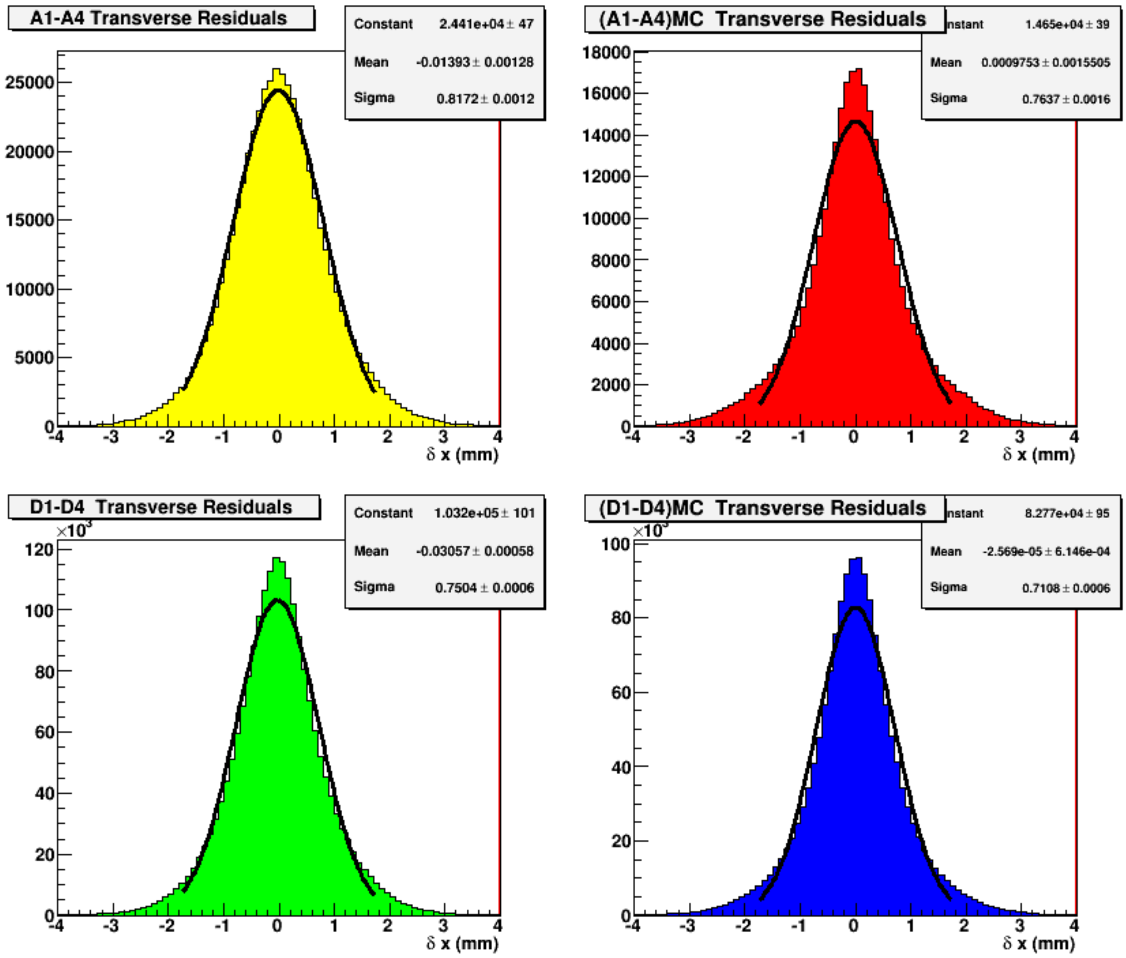

Figure 7.15: The distribution of residuals in the transverse direction for $ArCO_2$ data sets A1-A4 and D1-D4.

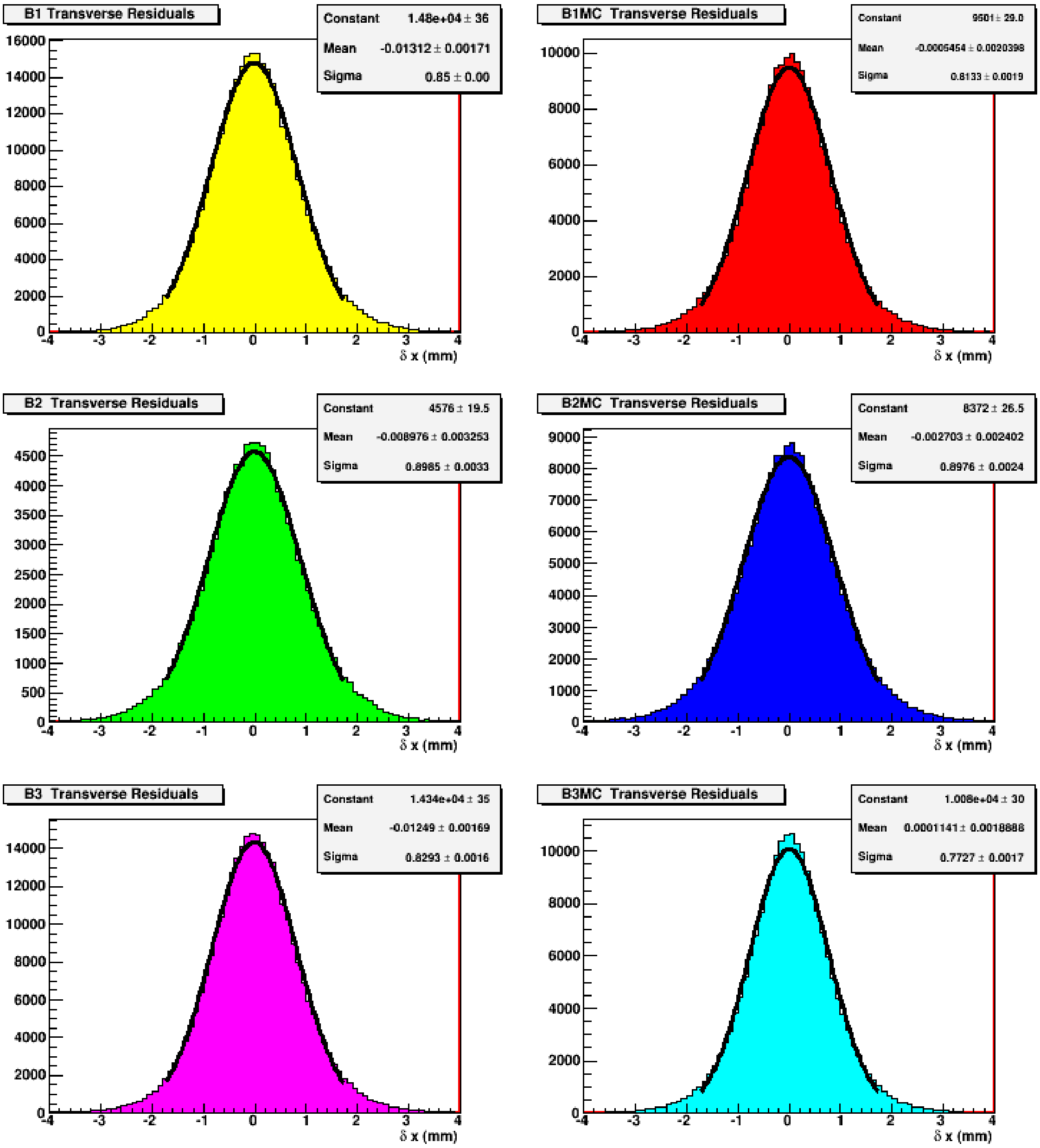

Figure 7.16: The distribution of residuals in the transverse direction for $ArCH_4CO_2$ data sets B1-B3.

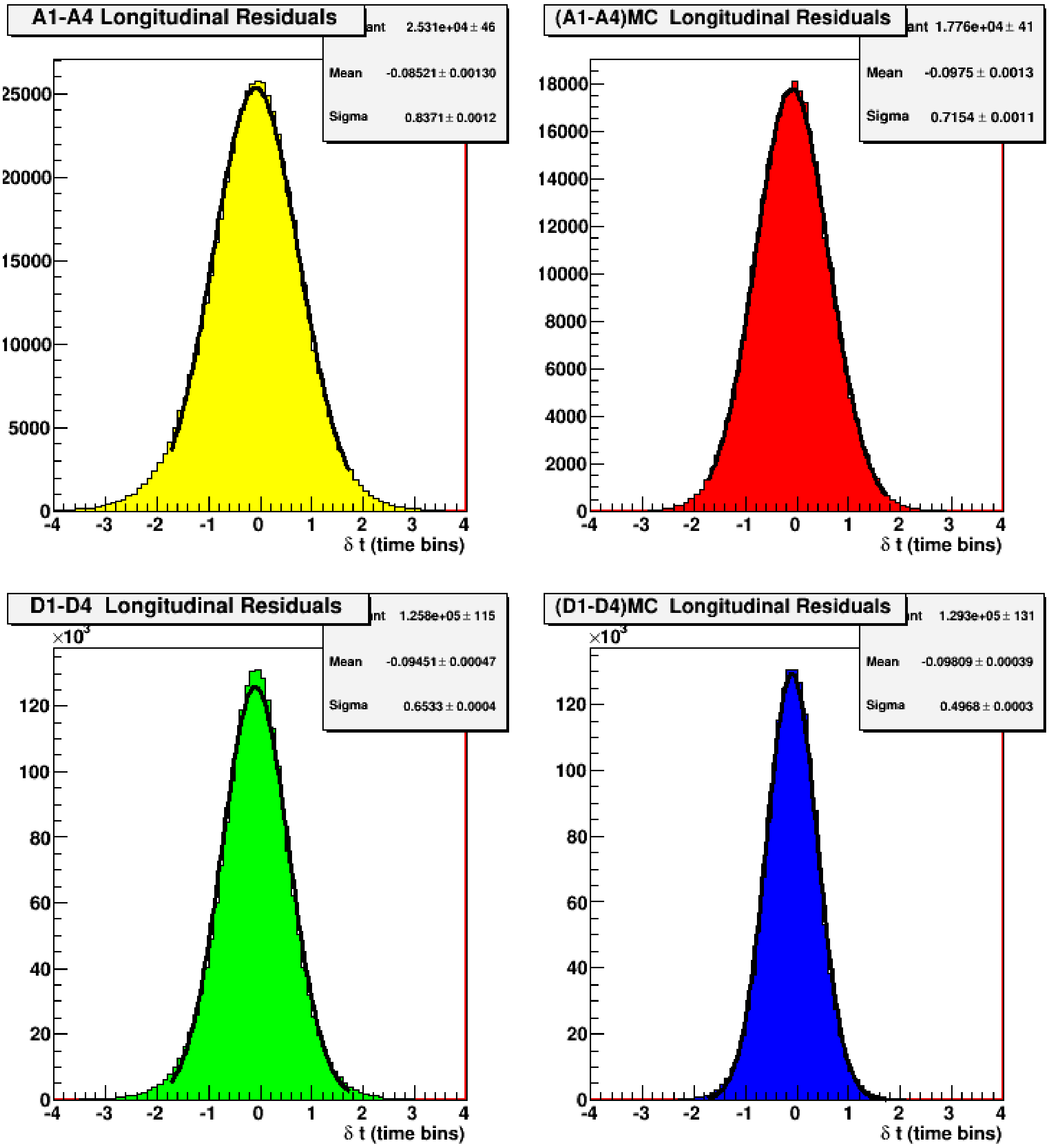

Figure 7.17: The distribution of residuals in the longitudinal direction for $ArCO_2$ data sets A1-A4 and D1-D4.

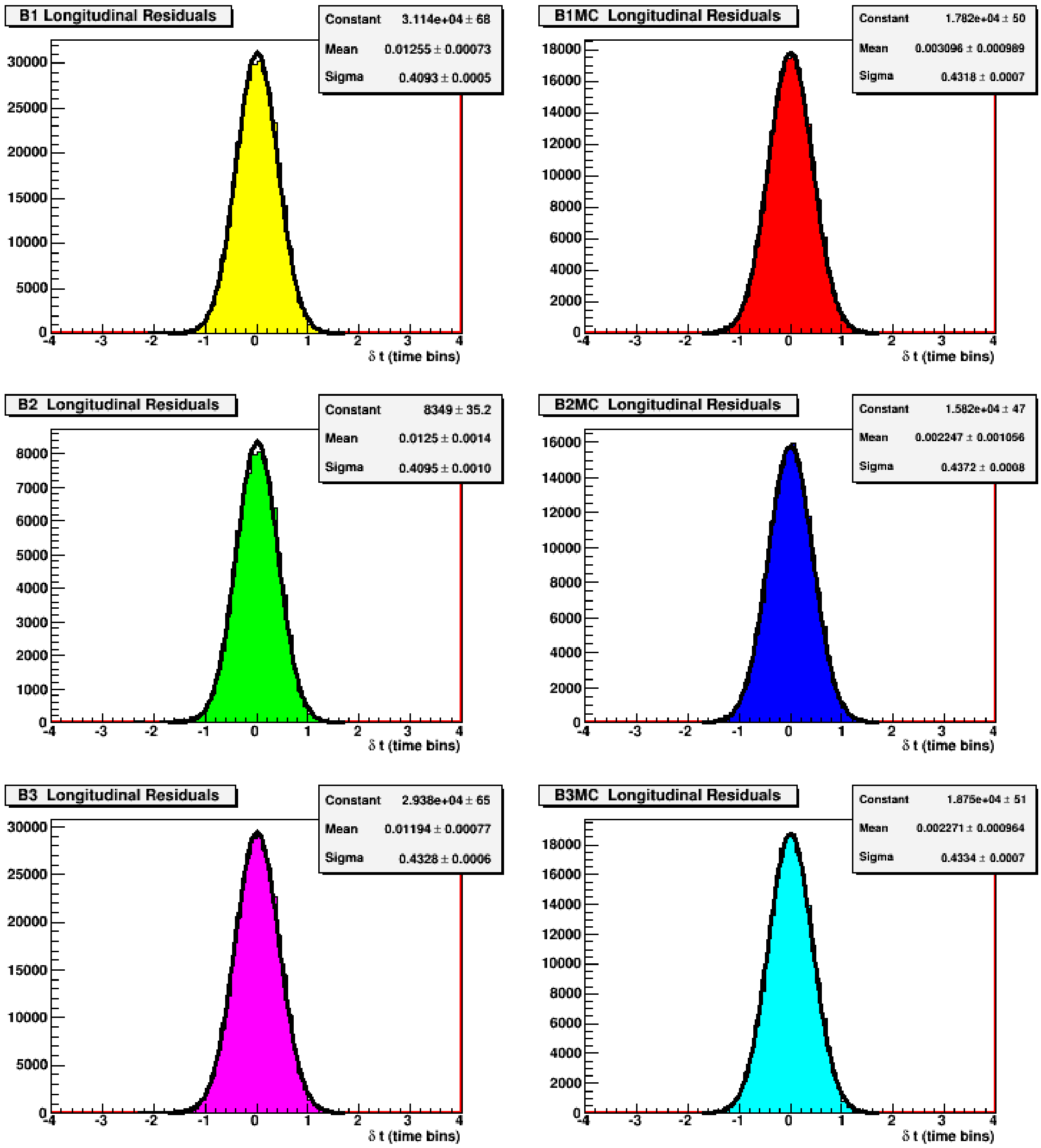

Figure 7.18: The distribution of residuals in the longitudinal direction for $ArCH_4CO_2$ data sets B1-B3.

it is important to understand any differences between the expected and measured distributions. It is shown in the following sections that there are systematic biases associated with tracks that pass through different regions of the TPC. These biases are sufficient to degrade the resolution of the TPC, and are the reason that the measured resolutions of different gases in the TPC are larger than predicted.

In the $ArCH_4CO_2$ gas data sets, (B1-B3) the transverse resolution improves as CO_2 content increases. (Recall that data sets B1, B2 and B3 respectively have CO_2 concentrations of 2%, 1% and 3%.) The correspondence between resolution and CO_2 concentration is largely due to the differences in diffusion constants. The drifting electrons in gases with higher diffusion constants will lose more position information as they drift through the gas volume, resulting in a larger uncertainty on the fitted position of the centroid which causes larger residuals between the track and the local track fit.

7.4.2 Resolution vs Drift

Figures 7.19 and 7.20 show the transverse resolution as a function of drift time for $ArCO_2$ and $ArCH_4CO_2$ data sets. The longitudinal resolution as a function of drift time for these gases is shown in figures 7.21 and 7.22.

Figures 7.19 and 7.20 show that the transverse resolution degrades with drift time. In all cases, the measured resolution is better than the Monte Carlo at low

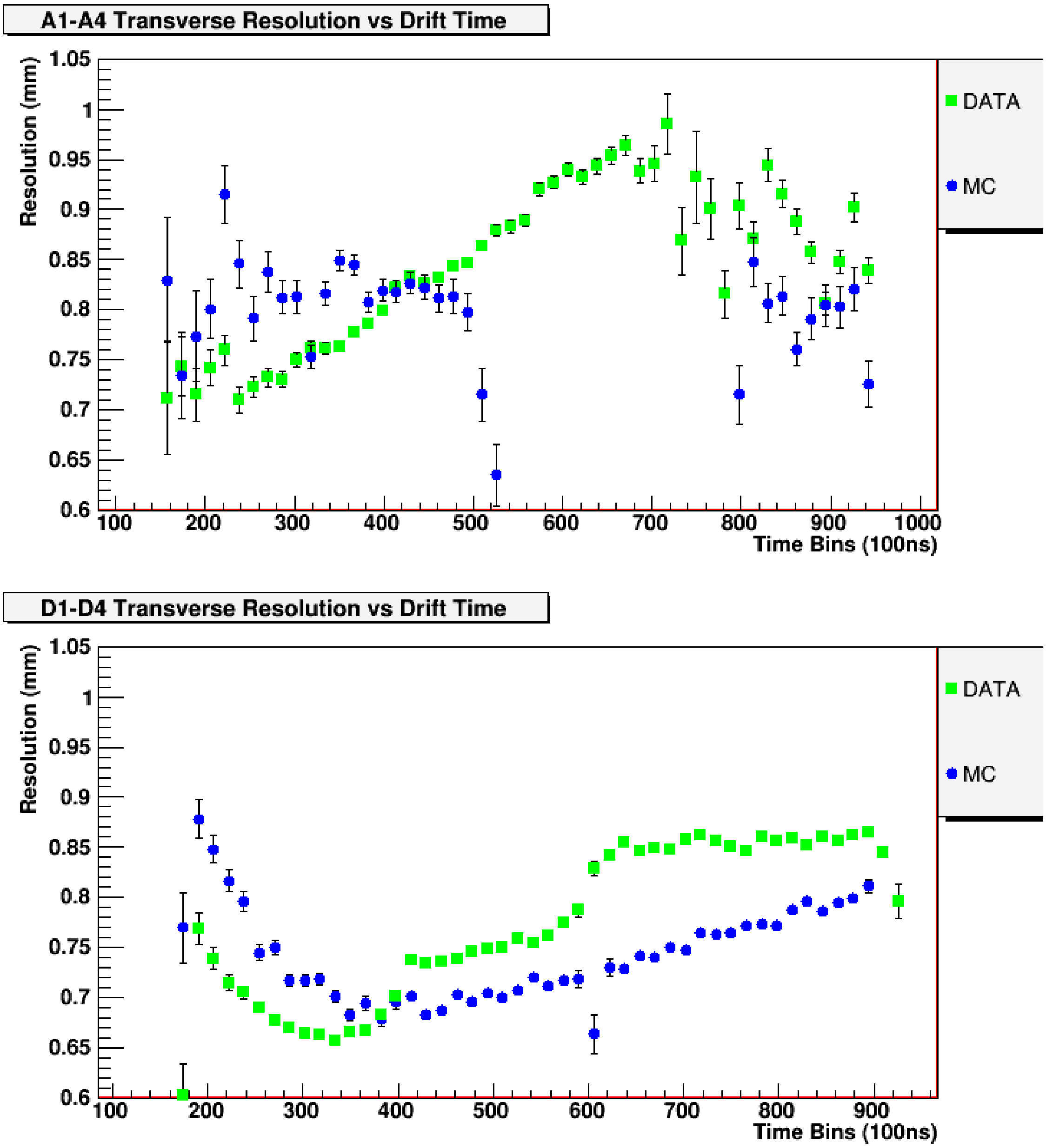

Figure 7.19: The transverse resolution of the TPC as a function of drift time for $ArCO_2$ data sets A1-A4 and D1-D4.

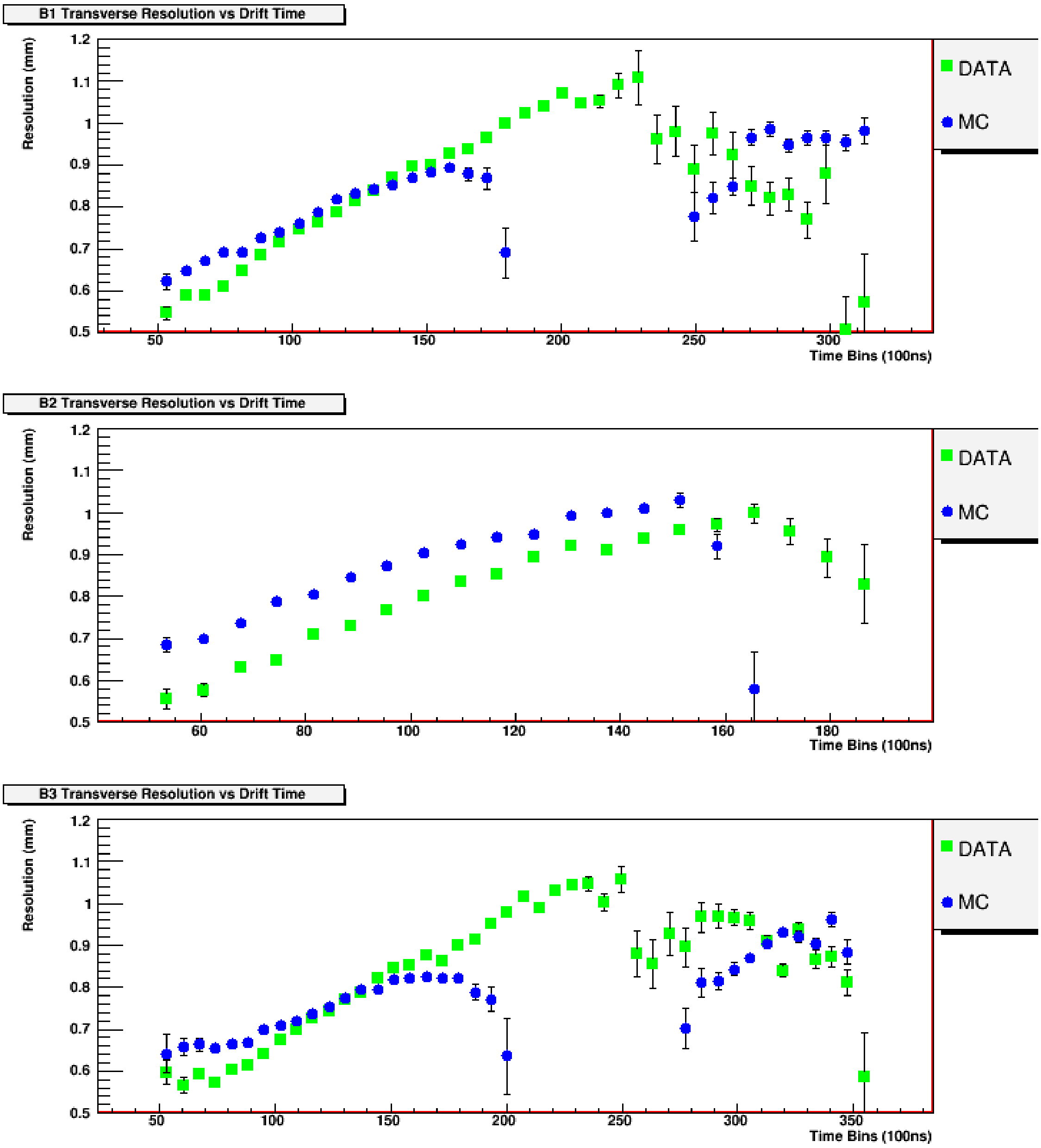

Figure 7.20: The transverse resolution of the TPC as a function of drift time for $ArCH_4CO_2$ data sets B1-B3.

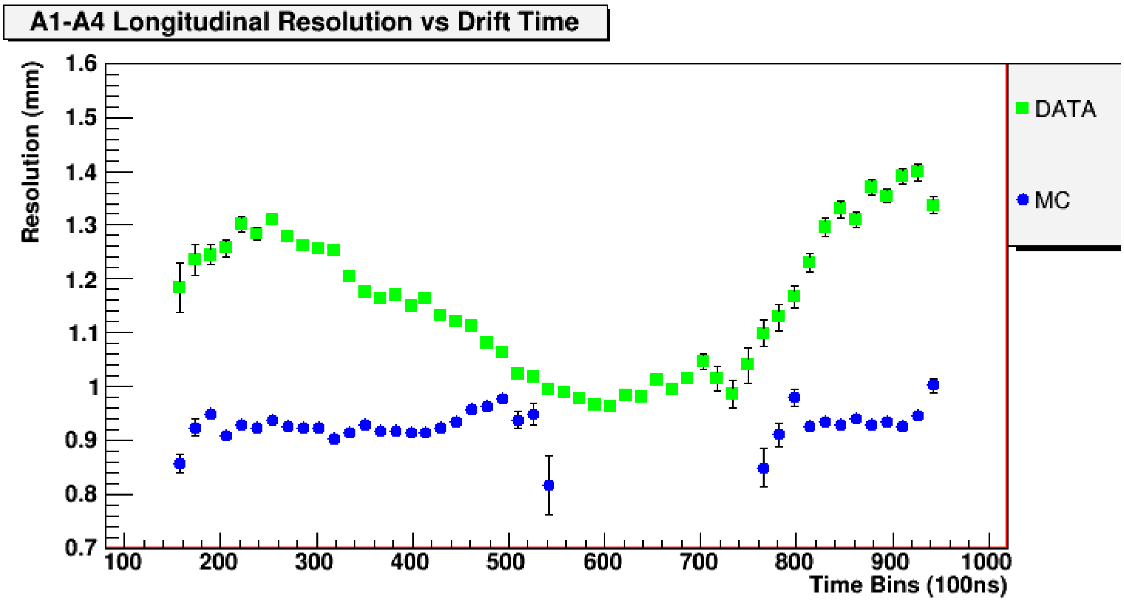

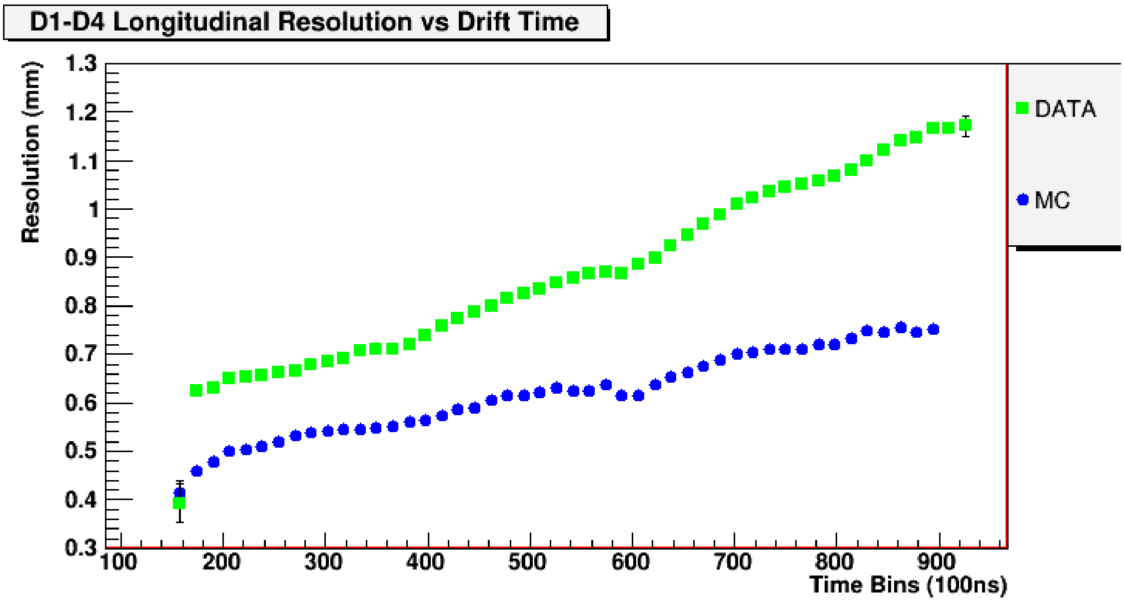

Figure 7.21: The longitudinal resolution of the TPC as a function of drift time for ArCO$_2$ data sets A1-A4 and D1-D4.

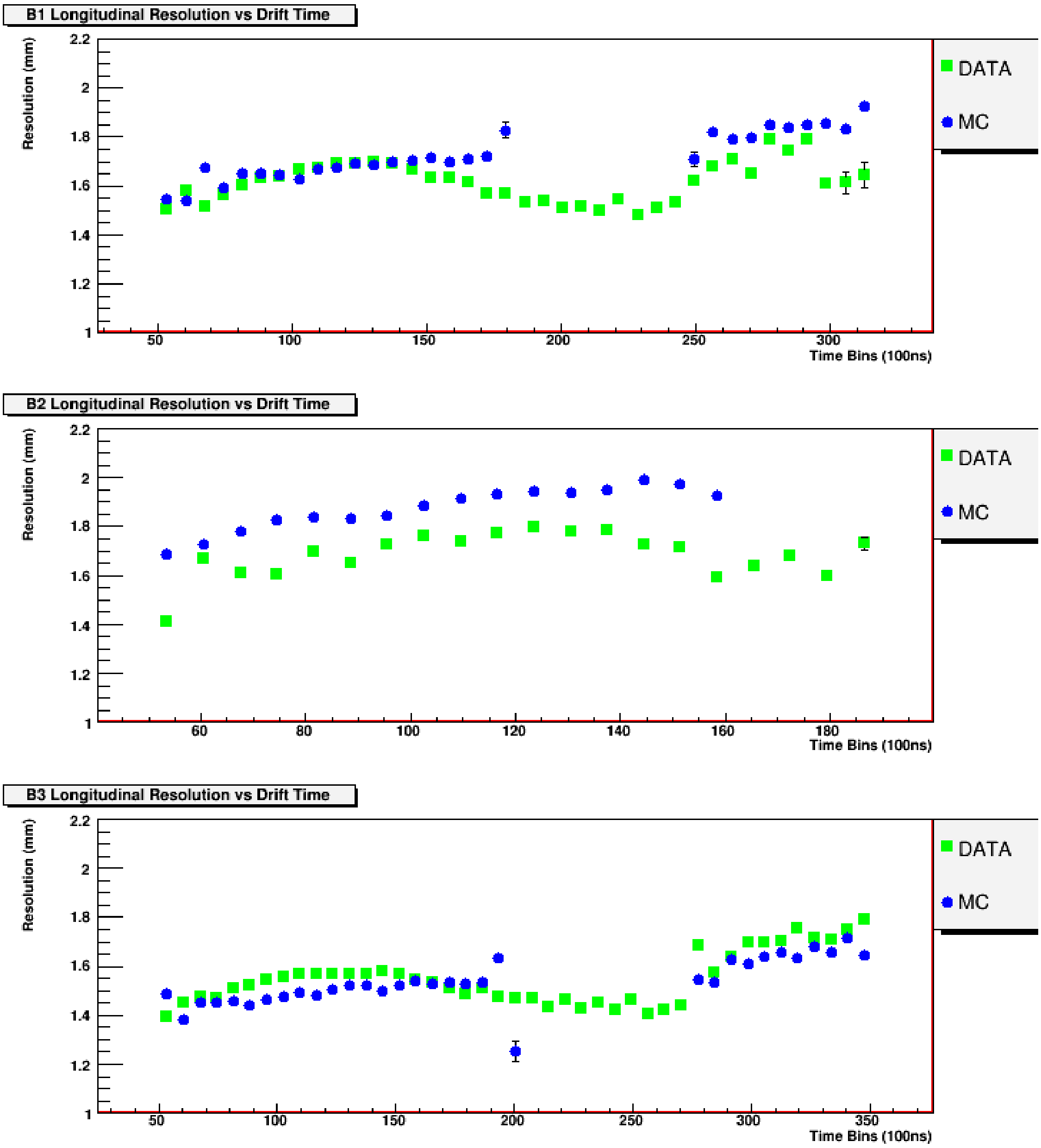

Figure 7.22: The longitudinal resolution of the TPC as a function of drift time for $ArCH_4CO_2$ data sets B1-B3.

drift times, but degrades more rapidly as drift time increases. The cause of this effect can be found by interpreting the distributions of data sets D and MCD in figure 7.19. In both the data and the Monte Carlo, the resolution degrades at low drift distances. At lower drift times, the charge cloud diffuses less before entering the amplification region in the GEMs; there is therefore a higher probability that a cluster of charge will cause only one pad in a row to be hit. If only one pad in a row is hit, the location of the actual centroid of the track is less well known than if multiple pads are hit, causing the resolution to decrease. It was shown in figures 7.4 thorough 7.6 that the average width of the tracks is underestimated by the Monte Carlo, so there is a larger probability that only one pad will be hit in the Monte Carlo rather than in the measured data, implying that the resolution of the data should be (and is) better at low drift distances. This effect is seen in all of the other transverse resolution distributions as well, albeit less clearly, since the drift time is much more dependent on the azimuthal and dip angles of the track in those cases.

In all cases, the transverse resolution generally increases with drift time. Again, this feature is caused by the dependence of diffusion on drift time. As the charge cluster diffuses, some position information is lost. The minimum of the distributions of data sets D and MCD in figure 7.19 is the point where there is sufficient diffusion to fire multiple pads, but less diffusion than at larger drift times, improving the resolution.

The longitudinal resolution of data sets A and D as a function of drift time is larger than the expected Monte Carlo values. The reason for the degraded resolution is unclear, but more insight will be gained in the following sections. The correspondence between Monte Carlo and measured transverse and longitudinal resolutions as a function of drift time is much better for the $ArCH_4CO_2$ data sets B1-B3.

With a more vertical trigger arrangement, data set D shows the expected degradation in resolution with drift time. The measured longitudinal resolution of data sets A and B is the best at intermediate drift distances because these are the tracks that have the lowest dip angles. There is a dependence of resolution on dip angle, as shown in section 7.4.6.

At this juncture, it is important to note that although the longitudinal resolution for $ArCO_2$ gas is larger in the measured data than the Monte Carlo, the measured longitudinal resolution still is more than sufficient for the physics requirements of the ND280m detector. In the transverse direction, the TPCs will be used to measure the radius of curvature of the products of neutrino interactions as shown in section 2.2.2, so properly understanding any transverse effects is especially crucial. In the longitudinal direction, however, the TPCs need to track the particles with less precision since the magnetic field causes particles to curve only in a plane perpendicular to the drift direction.

7.4.3 Resolution vs y

Figures 7.23 and 7.25 show the transverse and longitudinal resolution of $ArCO_2$ data sets A and D as a function of the y coordinate. Similarly, figures 7.24 and 7.26 show the transverse and longitudinal resolution of $ArCH_4CO_2$ data sets B1-B3 as a function of the y coordinate.

In figures 7.23 and 7.24, the measured transverse resolution distributions are similar to the Monte Carlo data. However, it is apparent that there is a large dependence of transverse bias on the y coordinate that is not expected from the Monte Carlo. There is a positive bias at low and high y coordinates, meaning that the overall track fit is generally to the left of the fits to the individual rows in those regions. At intermediate drift distances, the opposite is true, meaning that the track fit is generally to the right of the fits to the individual rows. Figure 7.27 shows a diagram of the type of track that would create such a bias distribution.

The cosmic ray muons used to collect the data are known to be travelling in a linear path, so there is some effect in the TPC that causes the charge cloud to be bent. Understanding this effect is important, since a bias of this type generates a shift in the measured curvature of a track. In section 2.2.2, it was shown that any systematic effects introducing a false curvature of a track have to be understood at the 0.1mm level to satisfy the T2K physics goals. Figures 7.23 and 7.24 show that there is an effect that causes an average change in the sagitta of a curved track of

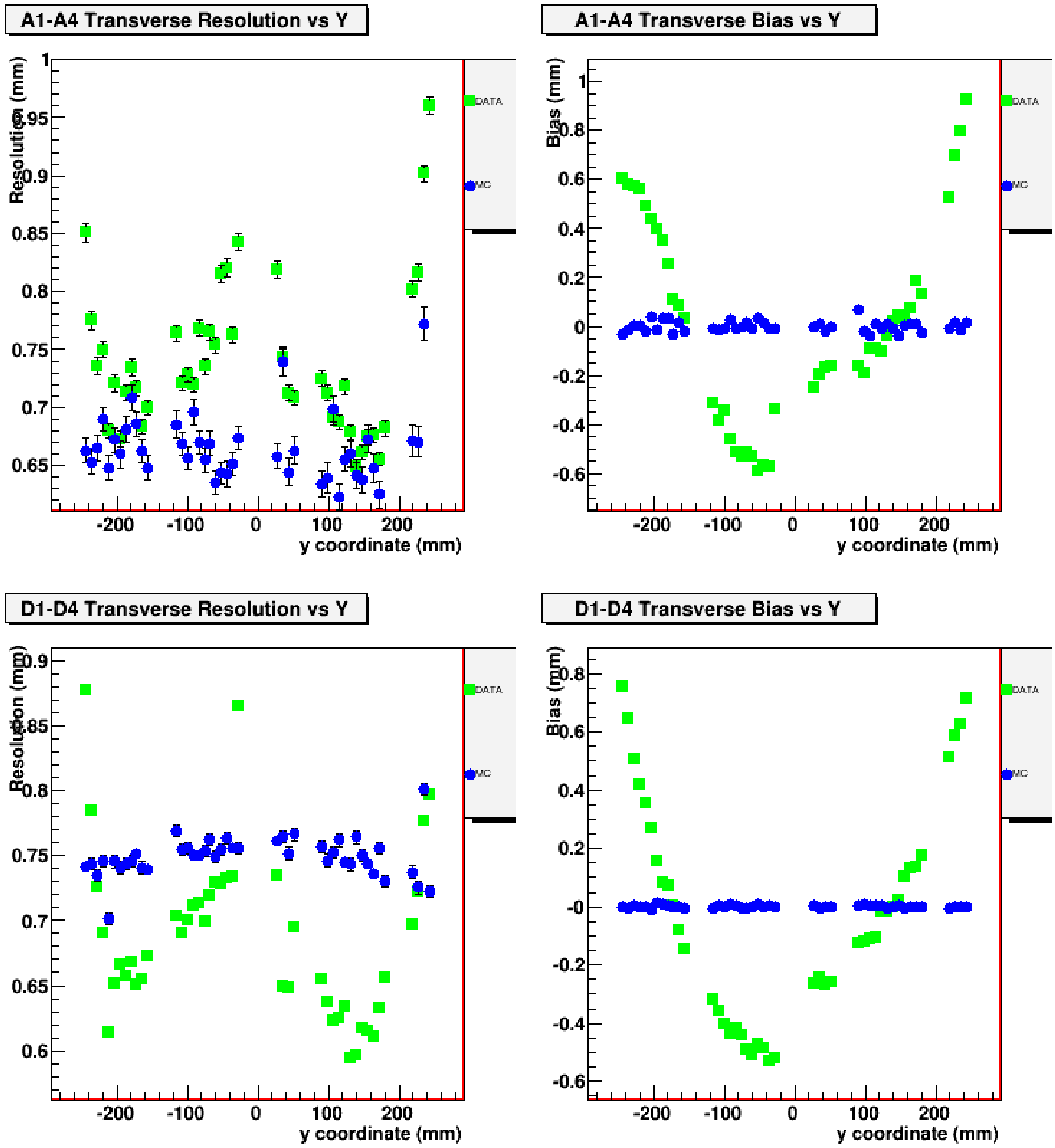

Figure 7.23: The transverse resolution and bias of the TPC as a function of local y coordinate for $ArCO_2$ data sets A1-A4 and D1-D4.

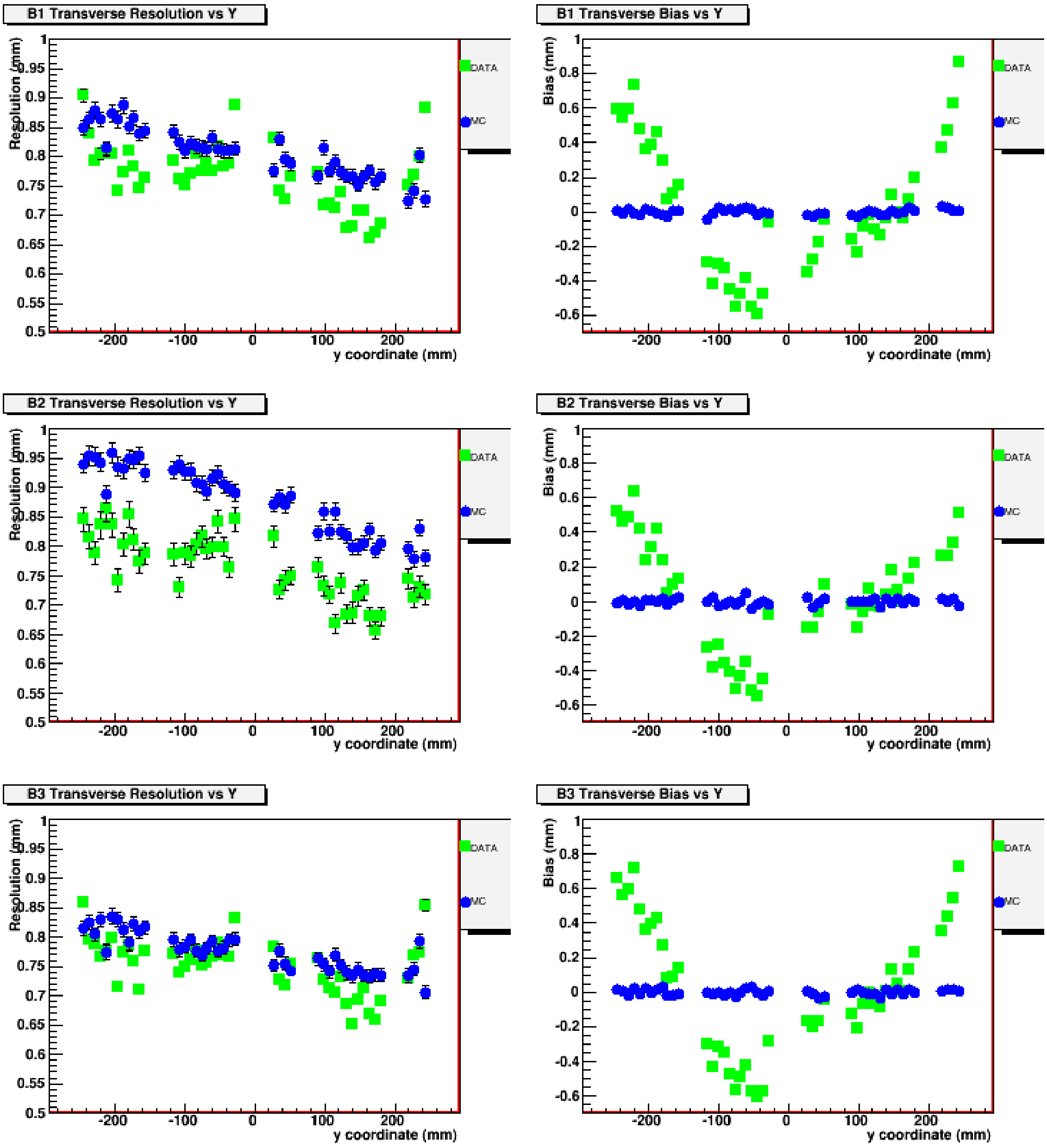

Figure 7.24: The transverse resolution and bias of the TPC as a function of local y coordinate for $ArCH_4CO_2$ data sets B1-B3.

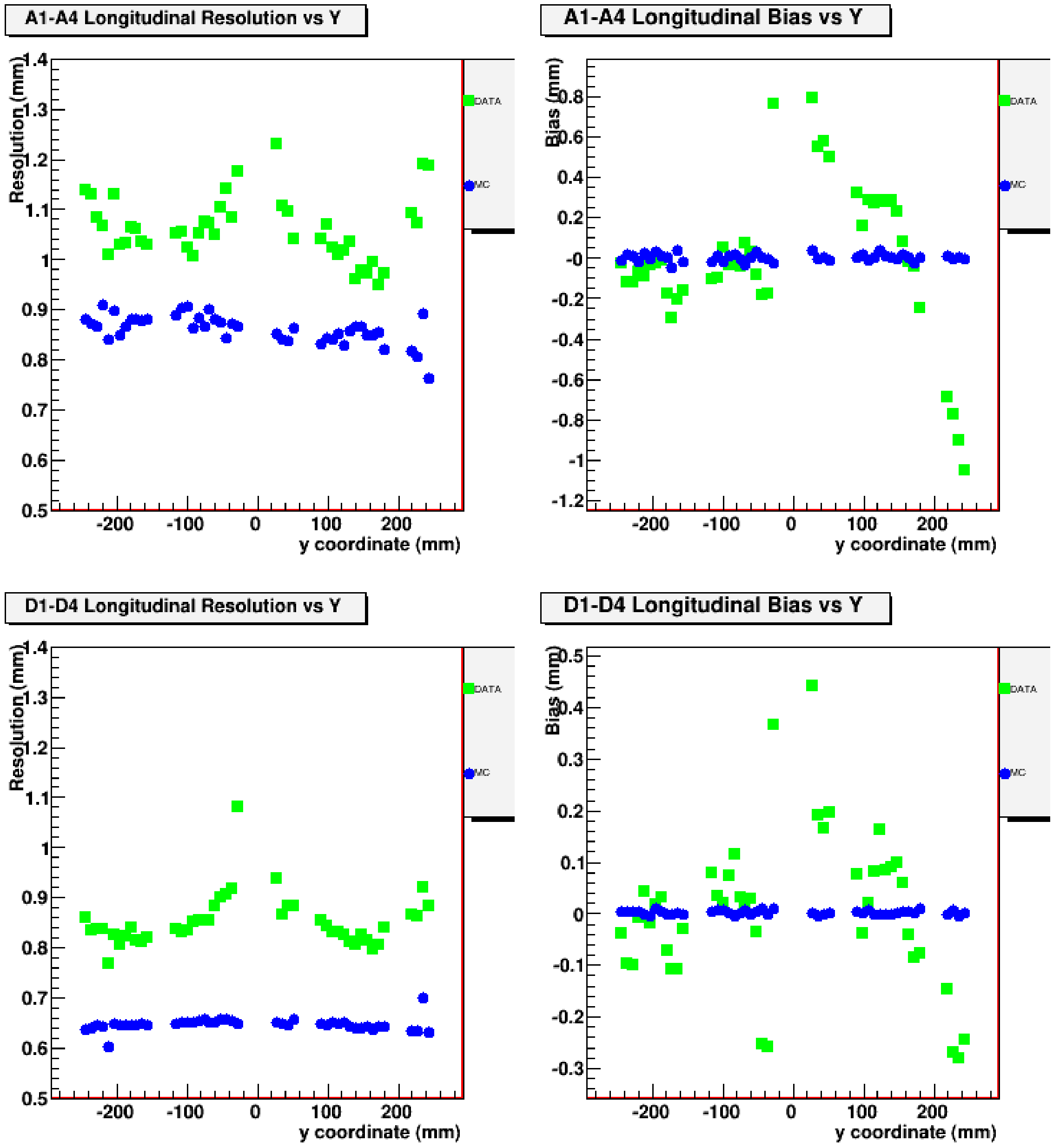

Figure 7.25: The longitudinal resolution and bias of the TPC as a function of local y coordinate for $ArCO_2$ data sets A1-A4 and D1-D4.

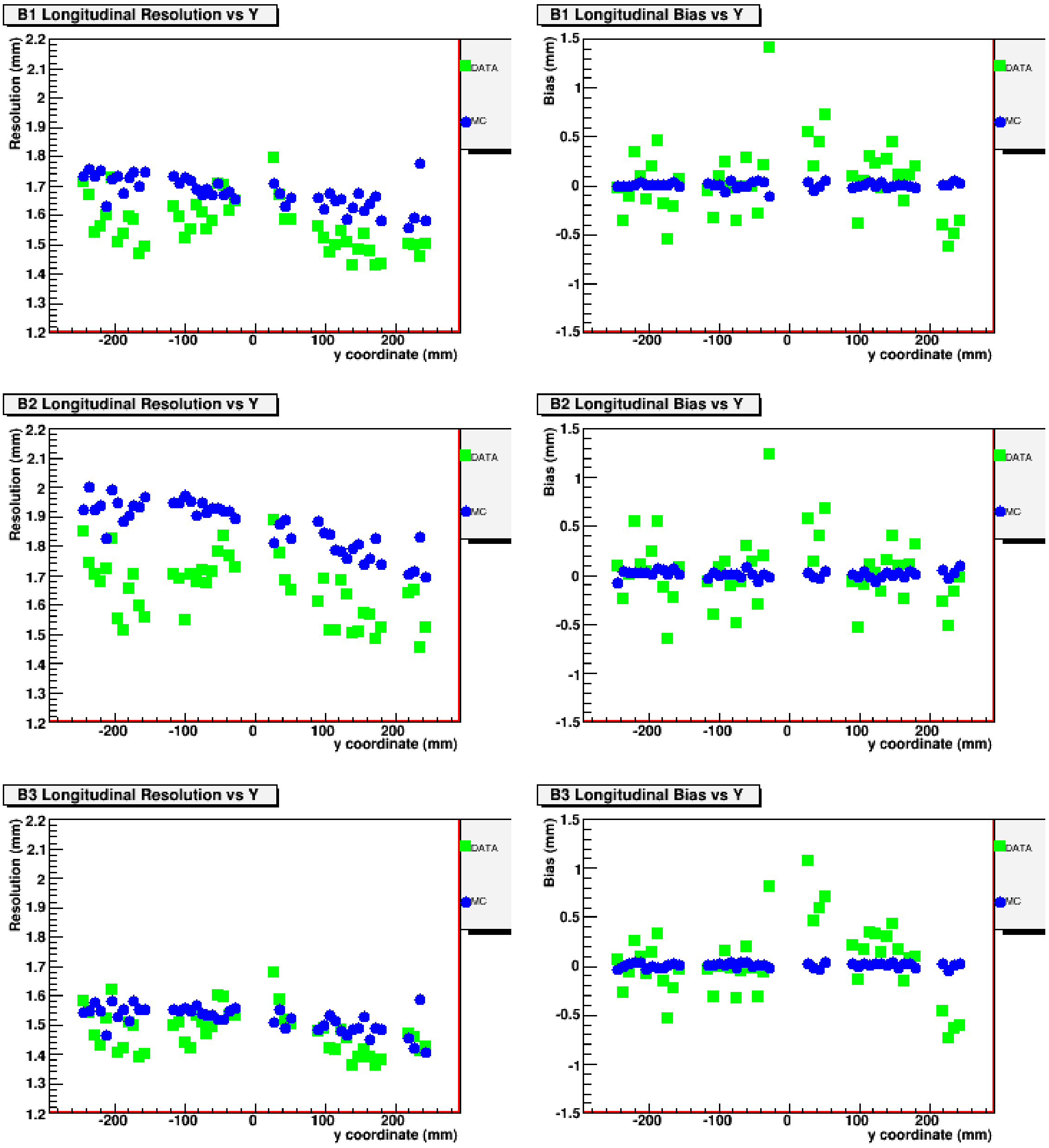

Figure 7.26: The longitudinal resolution and bias of the TPC as a function of local y coordinate for $ArCH_4CO_2$ data sets B1-B3.

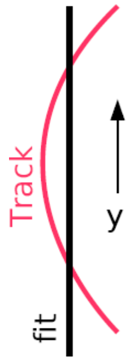

Figure 7.27: A diagram of a track that has a bias distribution similar to that shown in figures 7.23 and 7.25

over 1mm, clearly showing the importance of understanding and correcting for this effect.

There are two possible reasons for the transverse bias distributions to appear as they do. The first involves a physical rotation between the two modules. Should the modules not be perfectly aligned, straight tracks would appear to be kinked at the junction between modules, since the analysis assumes perfect alignment between pad rows in the upper and lower modules.

The second potential cause of the anomalous transverse bias distributions could be a non-zero x component to the electric field in the TPC drift volume. If this hypothetical electric field component had a different magnitude at low and high y values than at intermediate y values, it would cause the cluster of electrons to drift in the x direction at different rates along the length of the track.

It is possible to distinguish between these two scenarios by performing independent track fits to the information in the upper module and the lower module for a single data set. If the modules are in fact rotated with respect to each other, then the track segments within the upper and lower modules will be straight. There should therefore be no significant bias in a track fit performed to either the upper or the lower module. Conversely, should the tracks be curved by a stray electric field in the TPC, the shape of a plot of transverse bias as a function of y should have a similar shape to the plots shown in figures 7.23 and 7.24. Figure 7.28 below shows plots of transverse bias as a function of y coordinate for independent fits performed on each module. Also shown are the residual distributions for the individual modules.

The bias distributions in figure 7.28 have similar shapes to those in figures 7.23 and 7.24, but with smaller deviations from zero. This result strongly argues against the effect being due only to a rotation between modules 1 and 2, and points towards a non-zero electric field component in the x direction that varies in y.

To characterize this stray electric field and gain greater insight into the effect causing the curvature of tracks in the TPC, the bias as a function of y coordinate is examined at different locations in the TPC. Figure 7.29 shows the transverse bias versus y for data sets D1 through D4, which were taken at different drift distances down the length of the TPC. Also shown is the transverse bias vs y for different x coordinates. In the latter case, a cut of $|\phi| < 0.05$ is applied so a single track will contribute to only one of the distributions.

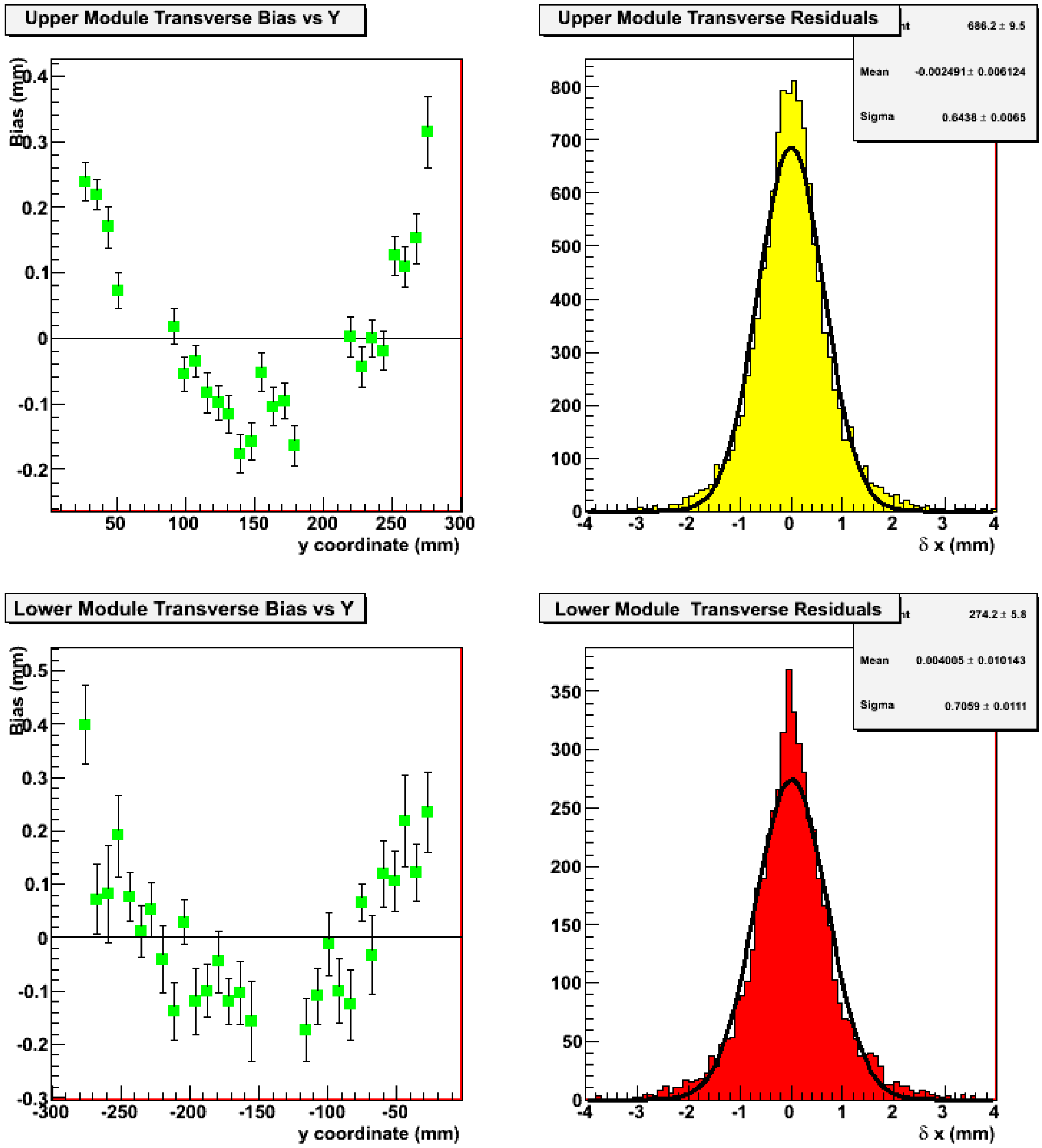

Figure 7.28: The transverse bias as a function of y coordinate and the residual distributions of the upper and lower modules.

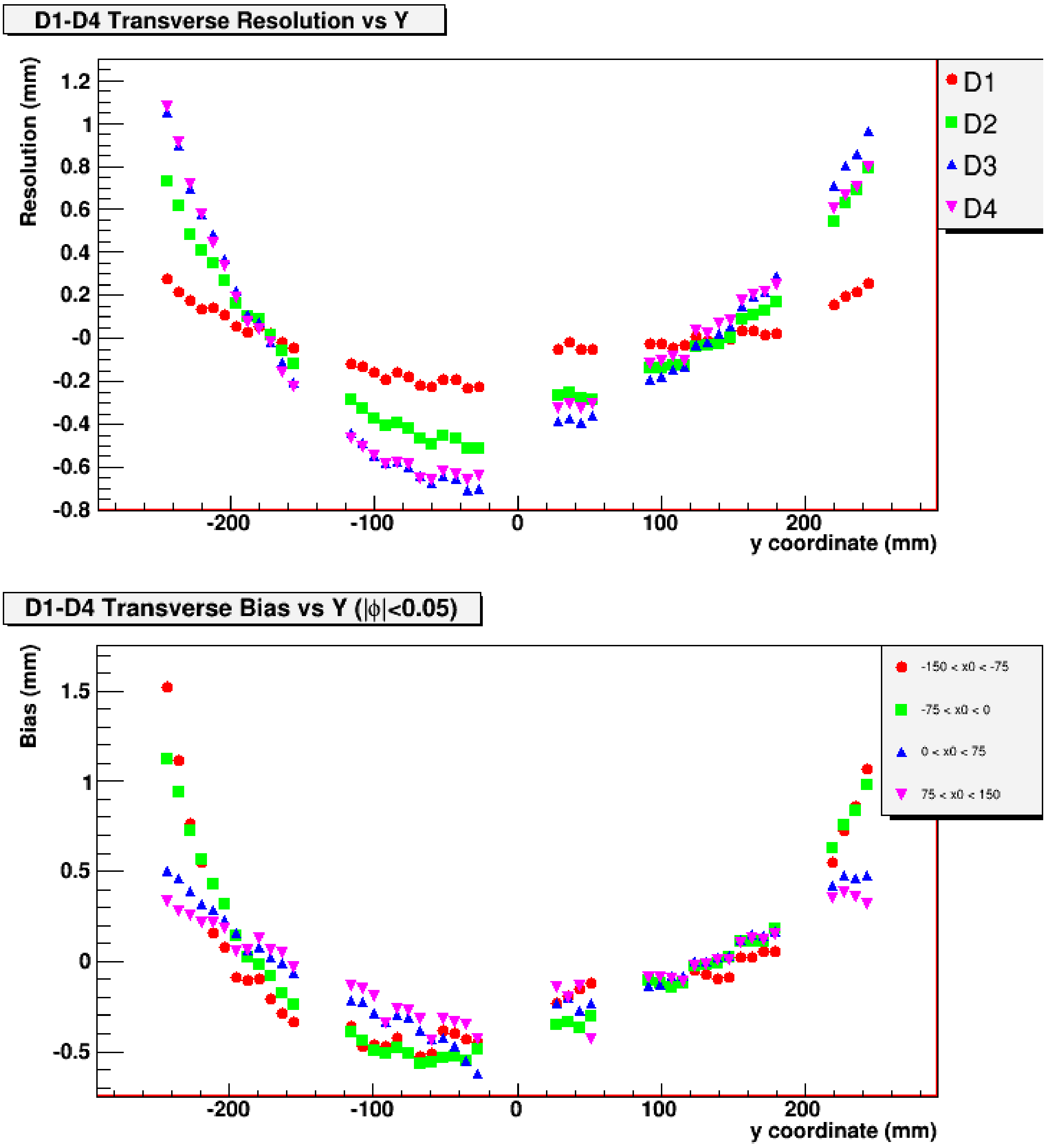

Figure 7.29: The transverse bias as a function of y coordinate for different drift distances and x coordinates.

Figure 7.29 shows that the magnitude of the distortions increases significantly as drift distance increases. (Recall that data sets D1 through D4 have vertically stacked scintillators, and the average drift distance increases with increasing data set number.) This implies that the electric field causing the distortion of the tracks is extended throughout the length of the TPC, since tracks that are created further away from the readout plane are more distorted, on average.

Also, the magnitude of the distortion decreases with increasing x coordinate, implying that the electric field causing the distortions is stronger on the left hand side of the TPC than the right.

There is a mechanism designed to characterize any track distortions in the TPC at a more precise level. On the central cathode of the TPC, (the plane opposite from the readout) aluminum strips have been laid out in a well-measured pattern. Figure 7.30 shows a picture of the central cathode with the aluminum strips. An ultraviolet laser whose wavelength is tuned to the work function of aluminum is coupled via fiber-optic cable to a lens placed between the readout modules.

When the laser is pulsed, the photons strike the central cathode, ejecting electrons from the aluminum strips. No electrons are ejected from the copper or the carbon loaded kapton that coats the rest of the central cathode, since the photoelectric work functions of those two materials are higher. The ejected electrons drift down the length of the TPC, and their locations are measured by the readout pads. The TPC

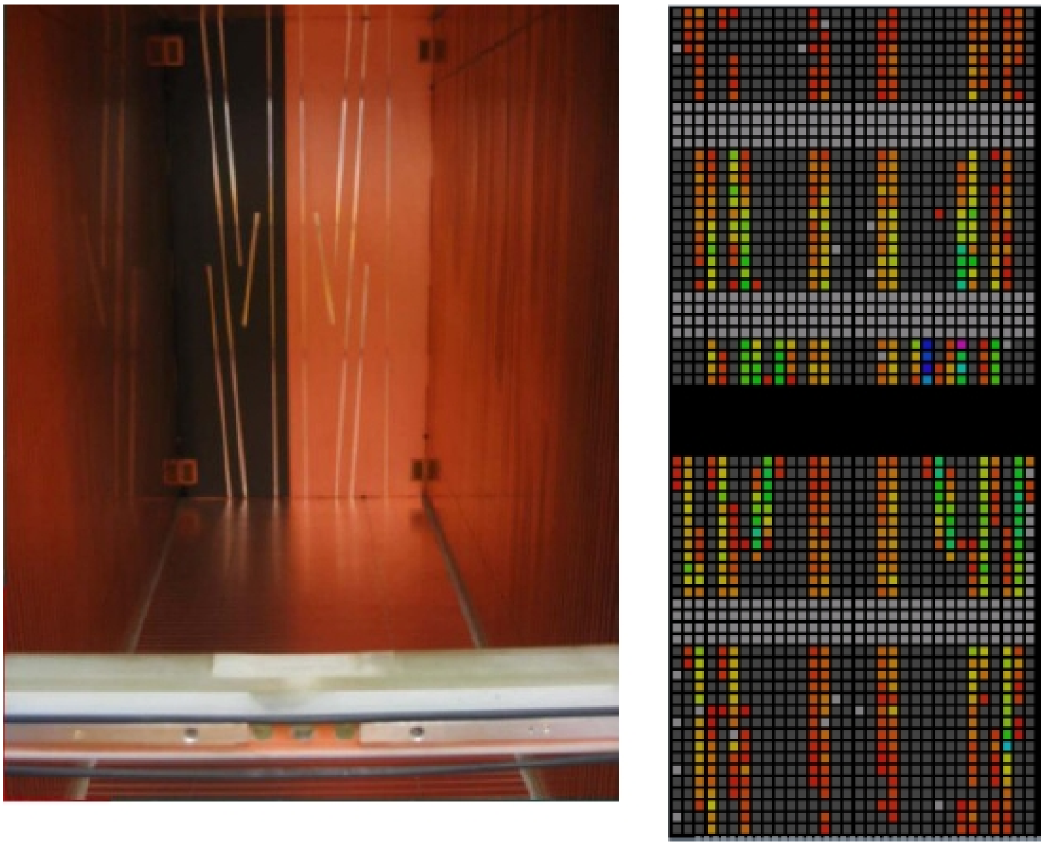

Figure 7.30: A photo of the pattern of aluminum strips on the central cathode, as well as the readout from a typical laser flash.

readout display showing the measured pattern of electrons ejected from the central cathode is also shown in figure 7.30. Any difference between the measured track locations and the known locations of the aluminium strips accurately describes any distortions in the TPC. This laser system has come online only very recently, and as such, no results from any laser tests are included in this thesis, but there is a clear direction for future experimentation.

Figure 7.29 shows that the magnitude of the distortion of the track increases with drift distance. The laser system described above does not give any information on how the bias changes with drift, since the electrons are all ejected from the central cathode. The results of a study using the laser will therefore need to include cosmic-ray data of the type presented in figure 7.29 to determine how the stray electric field component changes with drift distance.

7.4.4 Resolution vs x coordinate

Figures 7.31 and 7.33 show the transverse resolution and bias and the longitudinal resolution and bias as a function of the x coordinate of the fitted track on the pad row where the resolution is being measured for data sets A and D. Figures 7.32 and 7.34 show similar plots for data sets B1-B3.

In data sets A and B, dependence of transverse bias on x coordinate is observed, with a shape similar to the dependence of of transverse bias on y coordinate. However, due to the large dip and azimuthal angles of the tracks in data sets A and B, the x and y bias distributions are not independent. In data set D, where the transverse x and y bias distributions are more independent due to the more vertical nature of the tracks, the magnitude of the bias as a function of x is much reduced. In this case, the magnitude of the bias is below 0.1mm, indicating that there are no significant systematics that need to be further understood from any of the plots of bias as a function of x-coordinate.

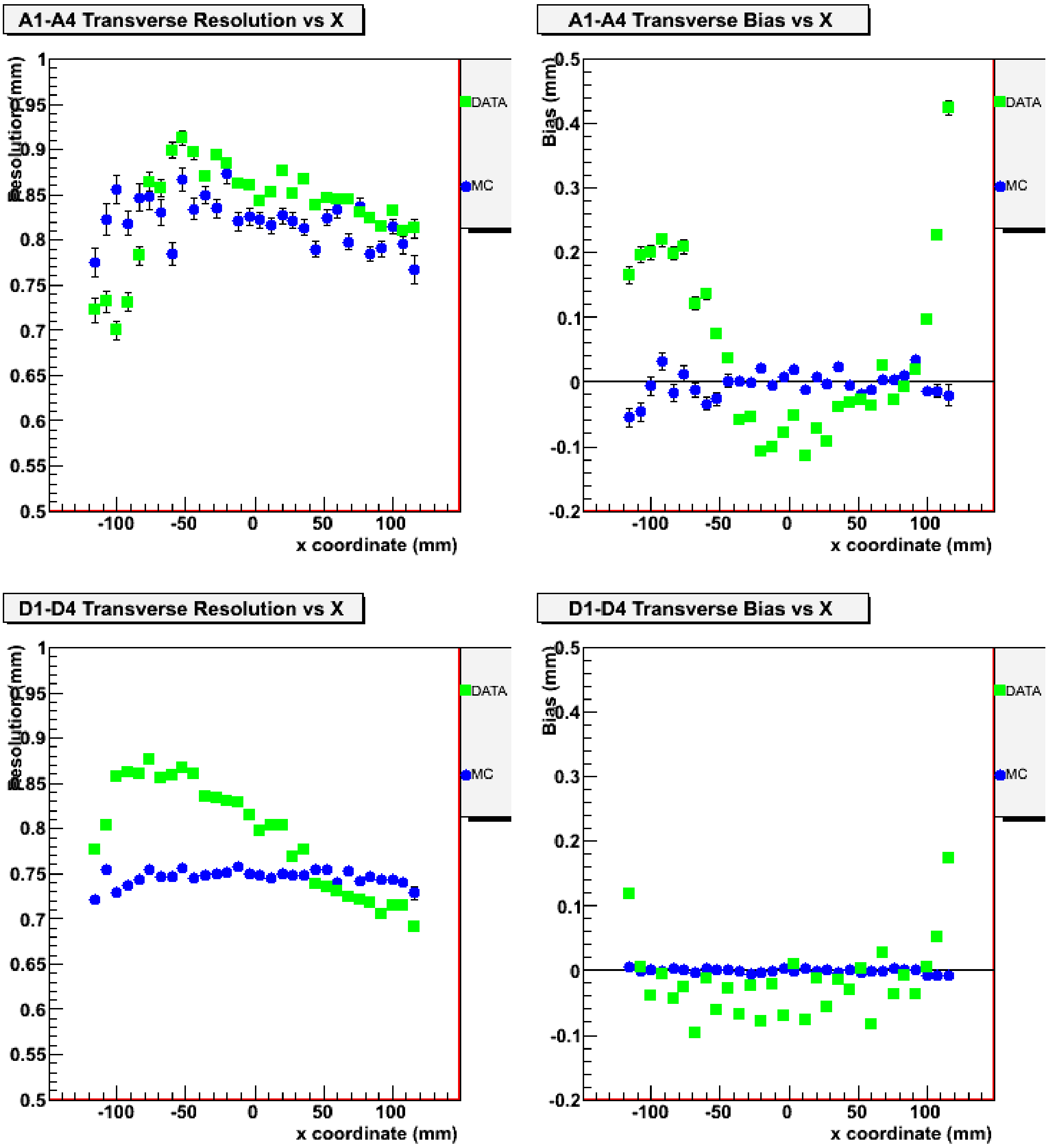

Figure 7.31: The transverse resolution and bias of the TPC as a function of local x coordinate for $ArCO_2$ data sets A1-A4 and D1-D4.

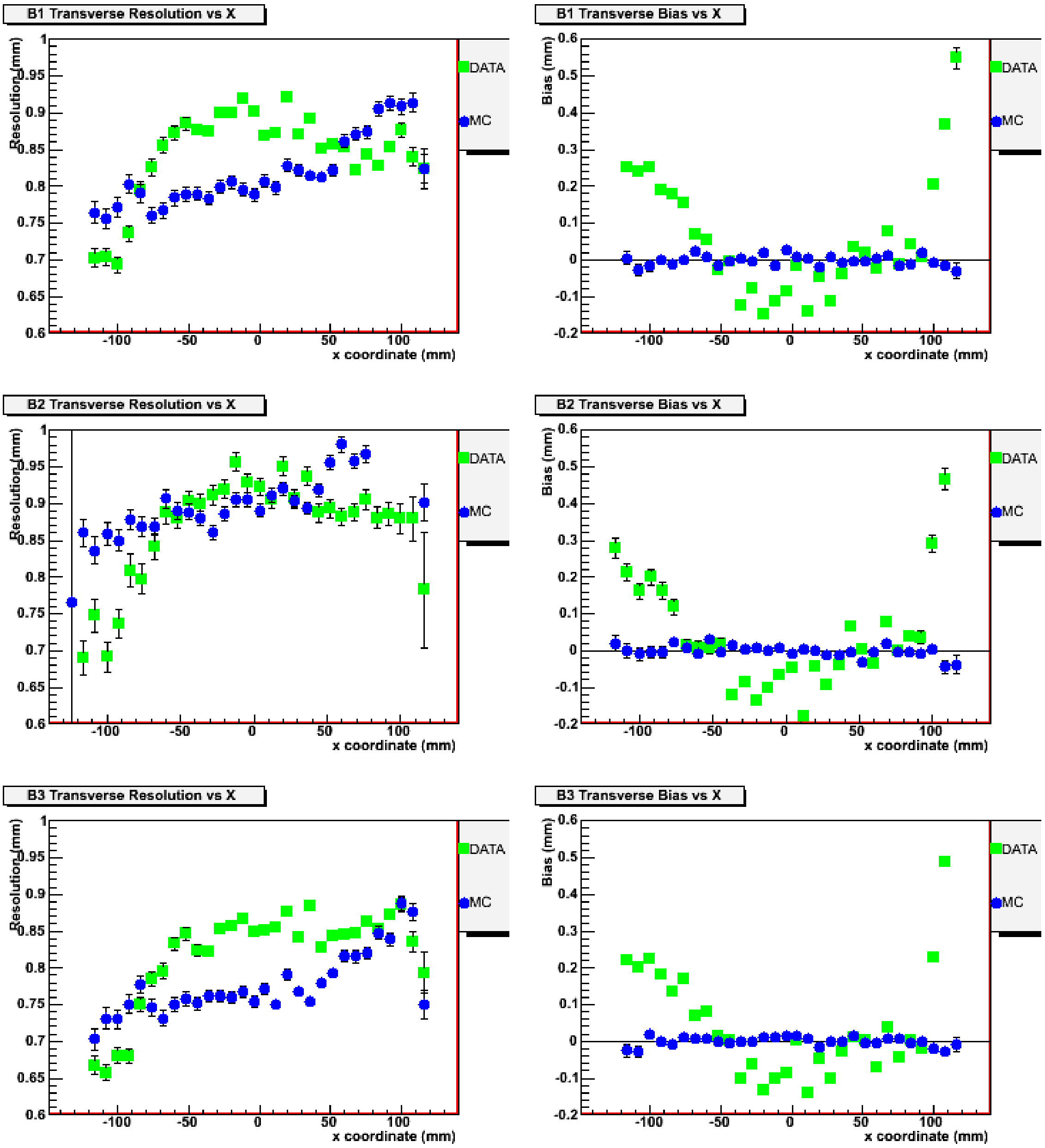

Figure 7.32: The transverse resolution and bias of the TPC as a function of local x coordinate for $ArCH_4CO_2$ data sets B1-B3.

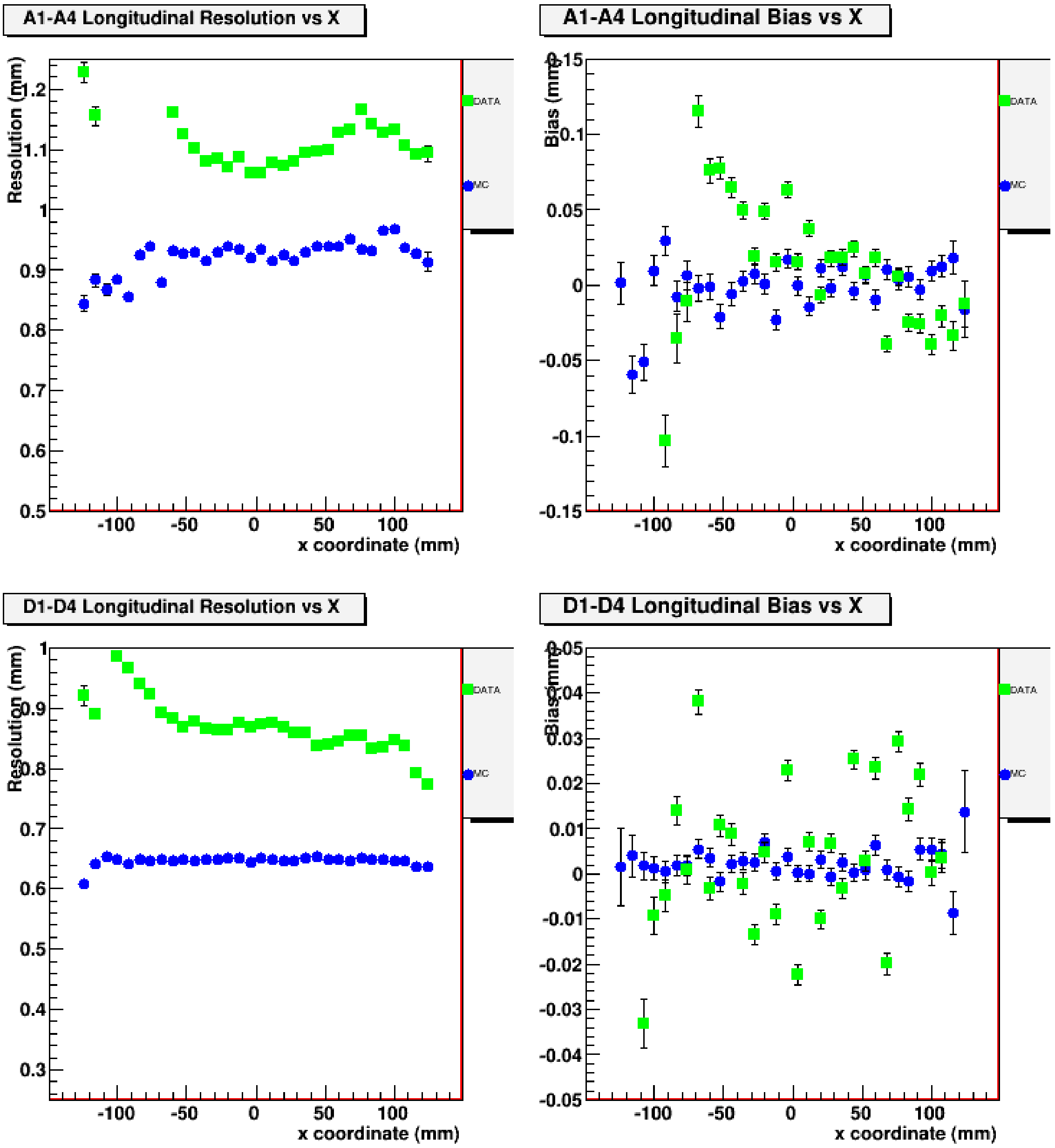

Figure 7.33: The longitudinal resolution and bias of the TPC as a function of local x coordinate for ArCO$_2$ data sets A1-A4 and D1-D4.

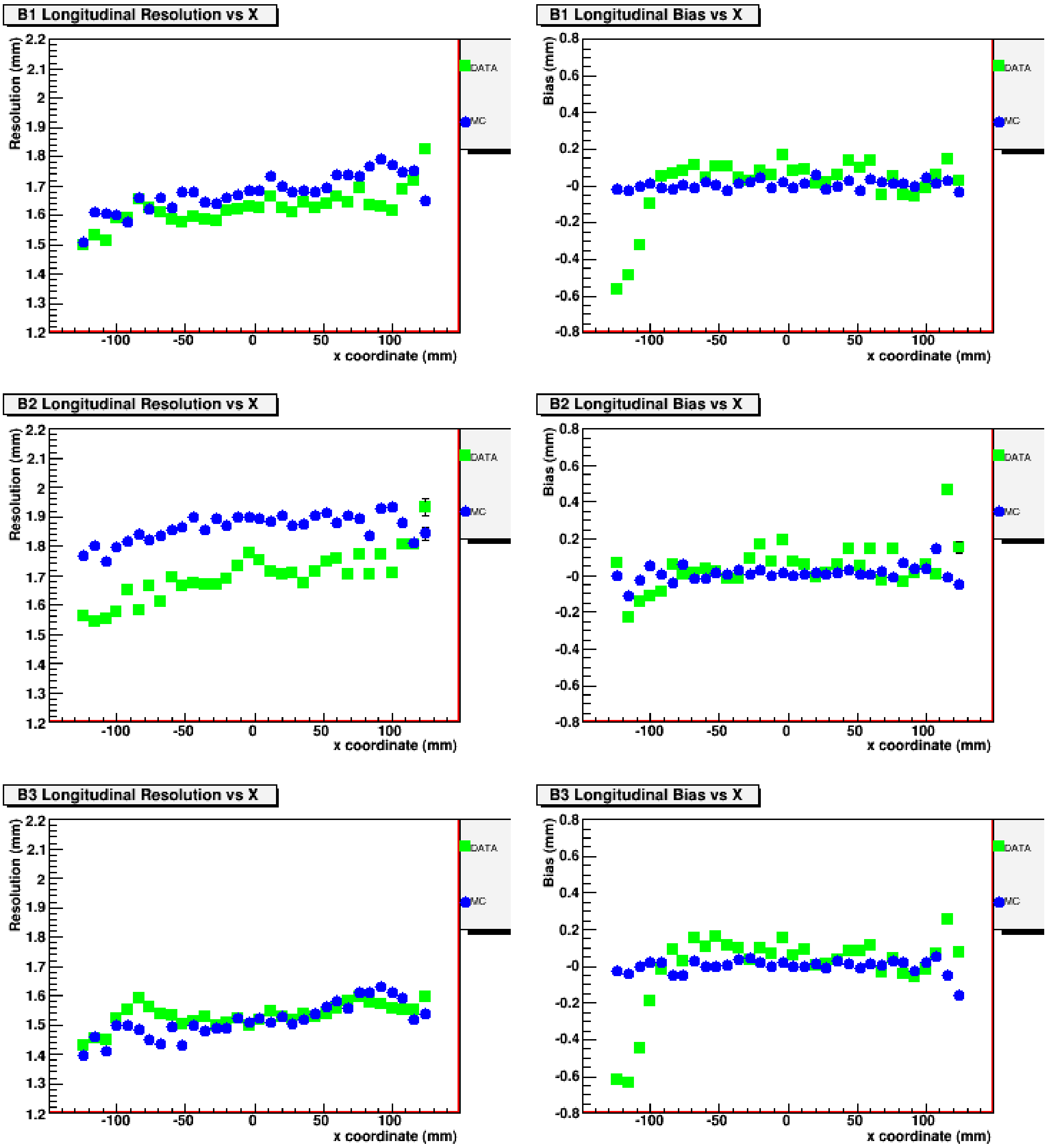

Figure 7.34: The longitudinal resolution and bias of the TPC as a function of local x coordinate for $ArCH_4CO_2$ data sets B1-B3.

In all data sets, the longitudinal bias shows no significant deviation from zero as a function of x coordinate. The longitudinal resolution of the $ArCH_4CO_2$ data sets is quite good, and agrees with the Monte Carlo in all cases. Again, the longitudinal resolution of $ArCO_2$ data sets A and D is slightly larger than predicted.

Many of the resolution plots, both transverse and longitudinal, show poorer behaviour for negative x coordinates. This effect is consistent with the results shown in the previous section, where the field distortions were found to be worse on the left (negative x) side of the TPC.

7.4.5 Resolution vs Azimuthal Angle

To further understand the properties of the TPC, the resolution is examined as a function of azimuthal angle (ϕ). Figures 7.35 and 7.36 show the transverse resolution and bias distributions for $ArCO_2$ data sets A, D2, and F1, and for $ArCH_4CO_2$ data sets B1-B3.

In data sets A and B, the resolution as a function of ϕ has a different shape than the Monte Carlo distributions. Since the track angle is correlated with many other variables in these cases, it is complicated to extract the true ϕ dependence of the TPC from data sets A and B. In order to address this issue, data set F1 was taken with the scintillators positioned as shown in case 8 in figure 5.3. This trigger configuration selects tracks with high azimuthal angle, but there is no correlation with drift time

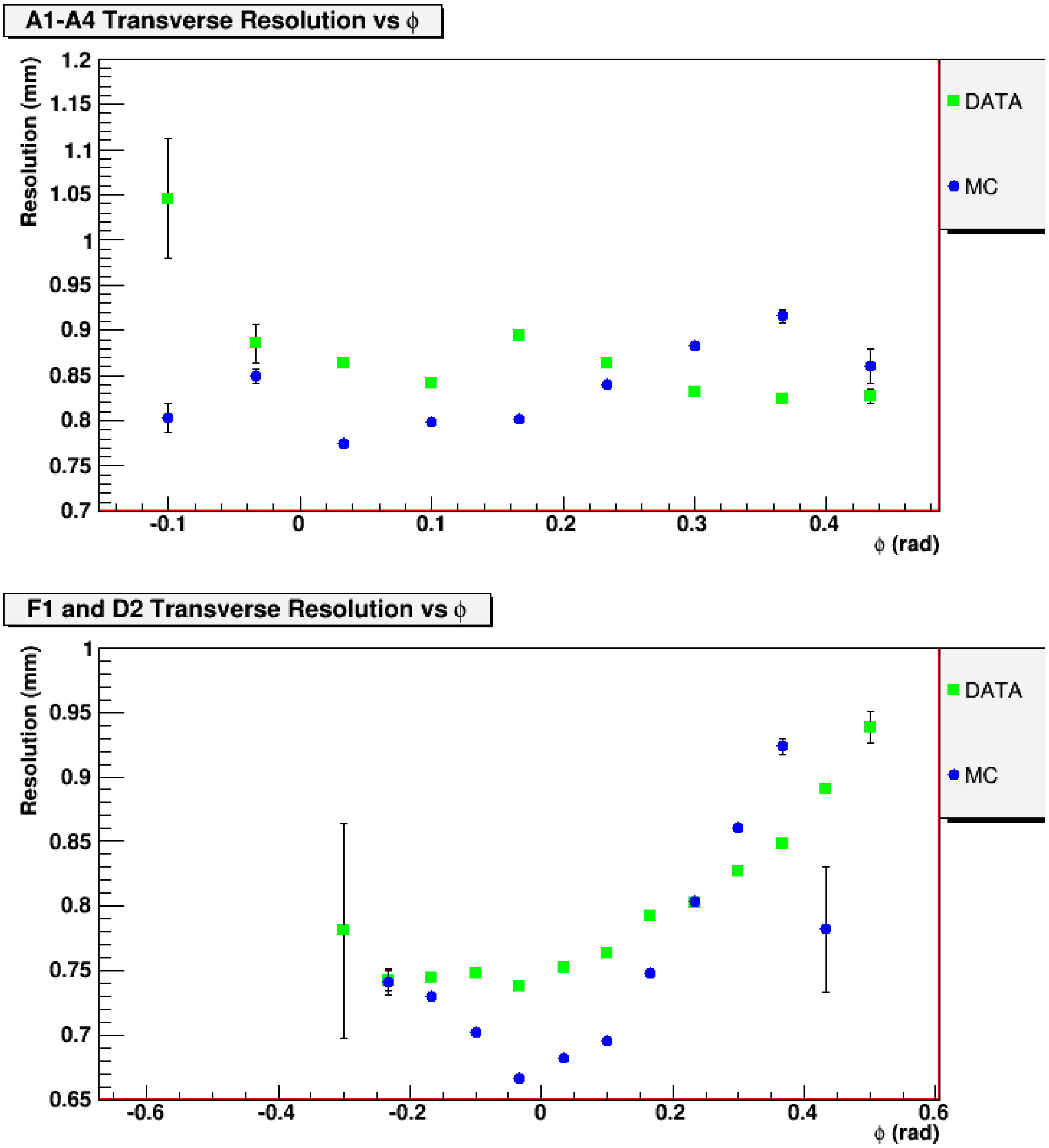

Figure 7.35: The transverse resolution and bias of the TPC as a function of azimuthal angle (ϕ) for $ArCO_2$ data sets A1-A4, and F1 and D2 combined.

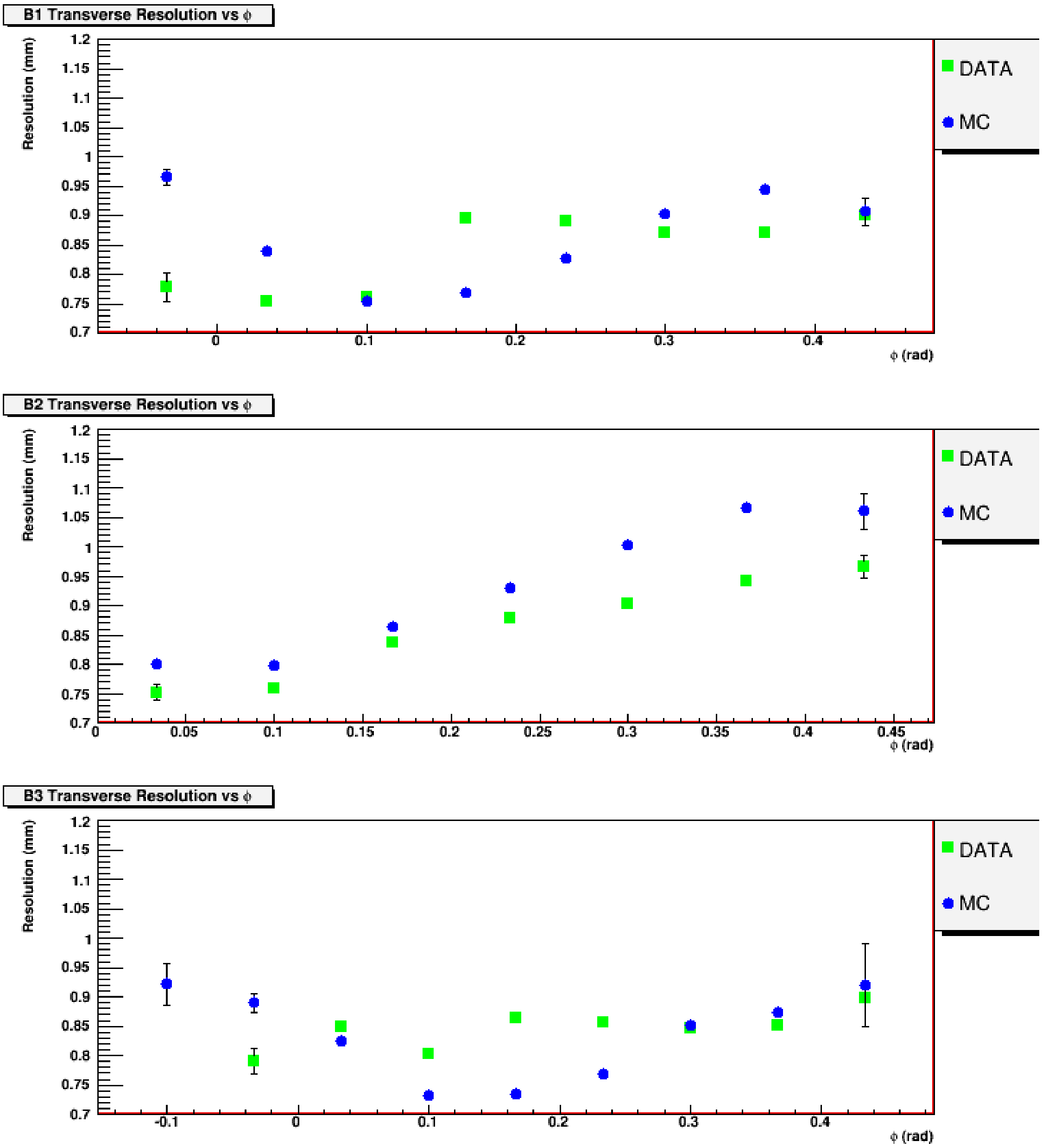

Figure 7.36: The transverse resolution and bias of the TPC as a function of azimuthal angle (ϕ) for $ArCH_4CO_2$ data sets B1-B3.

or dip angle. Data set F1 was then combined with the data from set D2, which covers the more vertical range of azimuthal angles at approximately the same drift distance. The resolution is seen to degrade as ϕ increases, but at a less severe rate than predicted by the Monte Carlo.

This degradation of transverse resolution with increasing azimuthal angle occurs because of non-uniform ionization along the length of the track. When a track has a large azimuthal angle, sections of low and high ionization can occur on different pads in the same row, which causes the fit to that pad row to be skewed in the direction of high ionization. This results in a larger residual measured for that row, and ultimately, a larger standard deviation of the residual distribution. This effect is depicted below in figure 7.37.

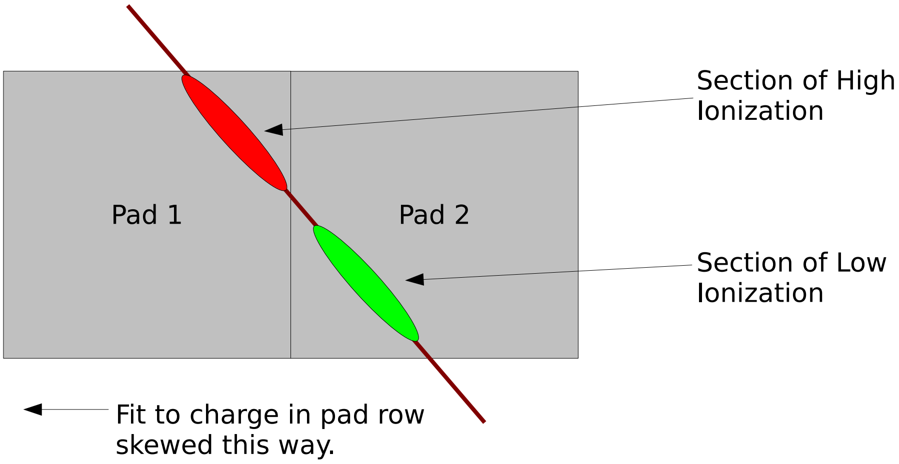

Figure 7.37: The non-uniform ionization along a track, responsible for degrading the resolution of the TPC at larger track angles.

7.4.6 Resolution vs Dip Angle

Finally, the resolution is studied as a function of dip angle ($\tan\lambda$). Figures 7.38 and 7.39 show the longitudinal resolution of data sets A and E, and B respectively.

Data sets E1 and E2 were taken to study the dependence of the resolution on dip angle, while minimizing any extra dependence on azimuthal angle, x coordinate, y coordinate and drift time. The scintillator configuration of these two data sets is shown in cases 6 and 7 in figure 5.3. Again, the data were combined with data set D2 to cover the full range of dip angles.

In all cases, the dependence of the longitudinal resolution on $\tan\lambda$ is very well modeled by the Monte Carlo, although the resolution is larger than predicted in data sets A and E, as has consistently been the the case for the longitudinal resolution in these data sets. The increase in longitudinal resolution as the dip angle increases is again due to ionization fluctuation along the length of the track. The fit to a row will be skewed in the direction of high ionization; in this case the fit will be skewed towards a longer or shorter drift time.

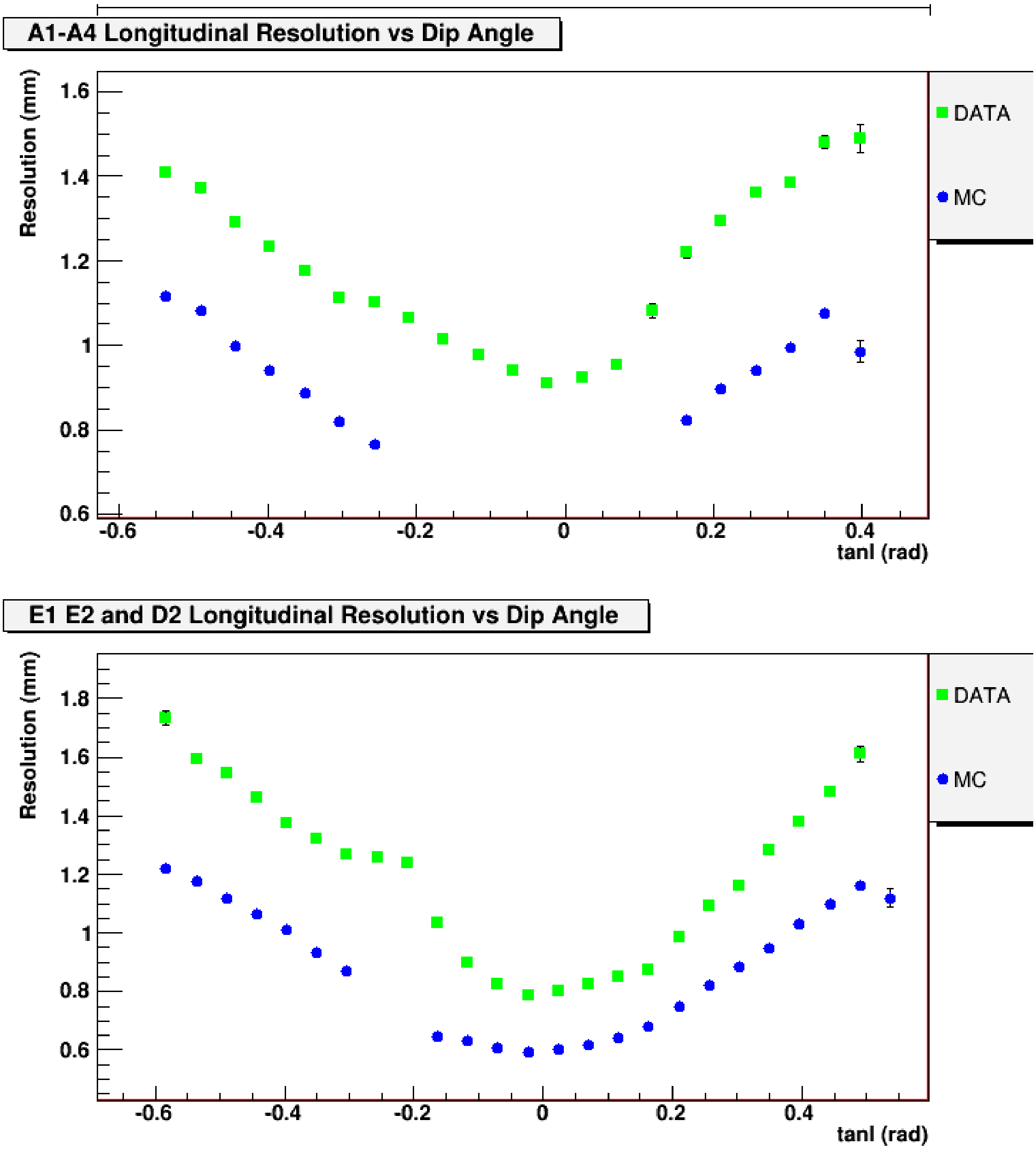

Figure 7.38: The longitudinal resolution and bias of the TPC as a function of dip angle ($\tan\lambda$) for $ArCO_2$ data sets A1-A4, and F1 and D2 combined.

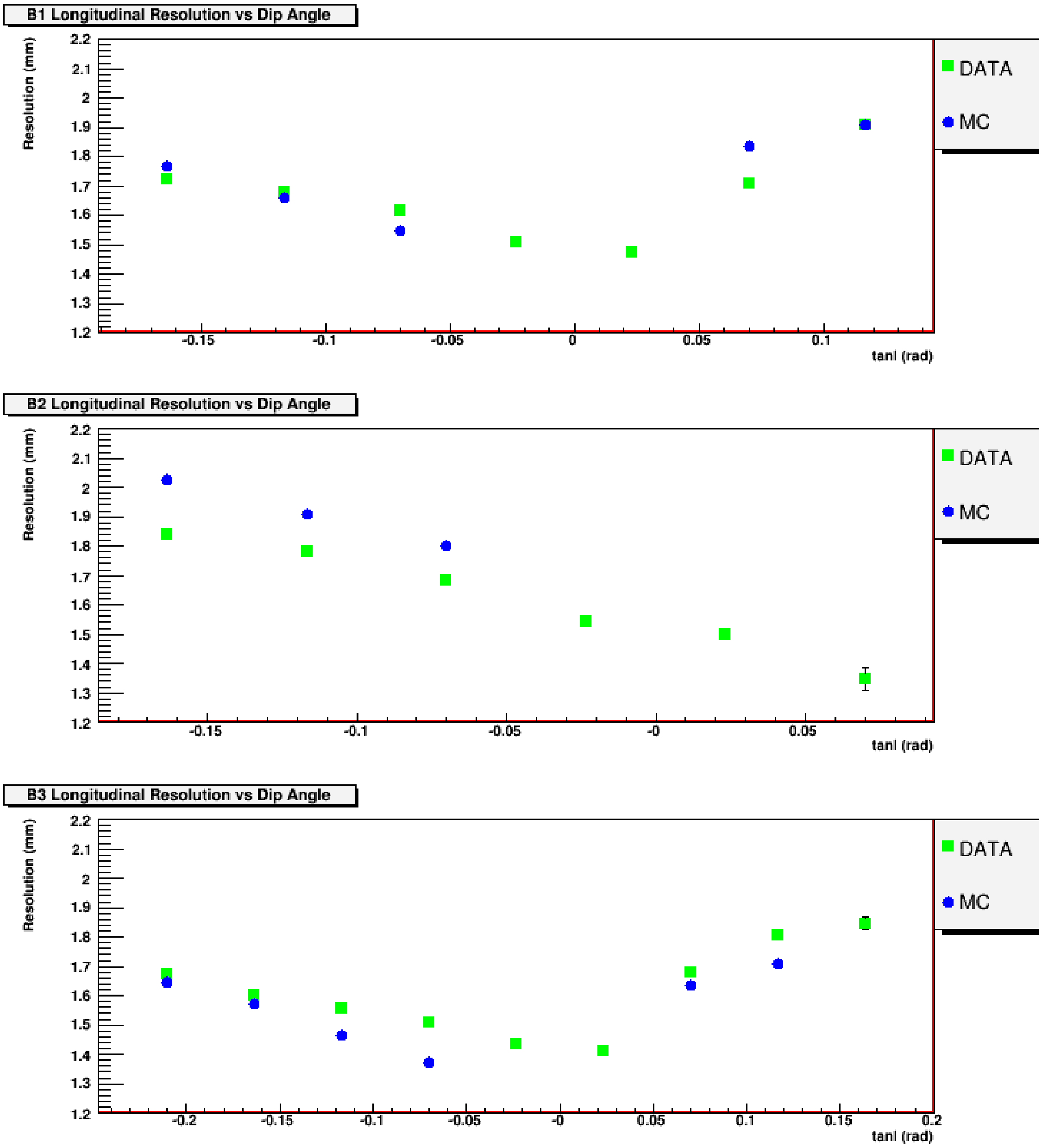

Figure 7.39: The longitudinal resolution and bias of the TPC as a function of dip angle ($\tan\lambda$) for $ArCH_4CO_2$ data sets B1-B3.

Chapter 8

Conclusion

Many aspects of a prototype TPC have been studied, determining the performance that can be expected from three TPCs that will be installed in the ND280m detector of the T2K experiment.

Using the TPC, the drift velocity and diffusion that were measured for different concentrations of $ArCO_2$ and $ArCH_4CO_2$ gas agree with the expected values. For the drift velocity and diffusion measurements, $ArCH_4CO_2$ gas was found to be more consistent with the theoretical expectations.

A main function of the TPCs in the ND280m detector is to measure the curvature of tracks in a magnetic field. As demonstrated in section 2.2.2, this places limits on the transverse resolution necessary to perform the desired measurements. Section 7.4.1 shows that the resolution of the TPC that was measured for different gasses is worse than predicted by the Monte Carlo by up to 7%.

An electric field component perpendicular to the drift direction has been identified as a likely candidate for the degraded resolution, since the track of electrons appears to bend as it drifts towards the readout. The severity of this bias increases with drift distance, indicating that the stray electric field is not only localized near the readout. To reduce this bias, a detailed map of the electric field inside of the TPC drift is required, and the laser system that will be used to characterize the field has just begun to be studied. Future work will involve using laser data and cosmic ray data to map the electric field in the TPC, and developing software corrections based on this map to correct the locations of the tracks on the pads.

In conclusion, the prototype TPC has proved to be very useful in outlining both the benefits and the challenges of using large scale time projection chambers as trackers in the ND280m detector. Most importantly, it has provided the T2K TPC group with a road map to follow in the design and construction of the full-scale TPCs. The TPCs are an integral part of the ND280m detector, and the results from the prototype strongly indicate that the full-size modules will perform well.

Bibliography

[1] The ND280 Collaboration. ND280m conceptual design report. Technical report, 2005.

[2] David Griffiths. *Introduction to Elementary Particles.* John Wiley and Sons, 1987.

[3] Fermi National Laboratory. A brief introduction to the standard model of high energy physics. `http://www-cdf.fnal.gov/events/stan.html`, 2005.

[4] W.M. Yao et al. *J. Phys. G: Nucl. and Part. Phys.*, 2006.

[5] S. Fukada et al. Constraints on neutrino oscillations using 1258 days of Super-Kamiokande solar neutrino data. *Phys. Rev. Lett.*, 86:5656–5660, 2001.

[6] The SNO Collaboration. Direct evidence for neutrino flavor tranformation from neutral-current interactions in the Sudbury Neutrino Observatory. *Phys. Rev. Lett.*, 89:011301, 2002.

[7] Donald Perkins. *Introduction to High Energy Physics*. Cambridge, 2000.

[8] The T2K ND280 software working group. `http://superk.physics.sunysb.edu/~mcgrew/t2k/nd280Doc/v1r0/dox/index.html`, 2007.

[9] R. Bouclier et al. The gas electron multiplier (GEM). *CERN-PPE-96-177*, 1996.

[10] M. Killenberg et al. Modelling and measurement of charge transfer in multiple GEM structures. *Nuclear Instruments and Methods in Physics Research A*, 498:369–383, 2003.

[11] L. Musa et al. The ALICE TPC front end electronics. In *Proc. of the IEEE Nuclear Science Symposium*, 2003.

[12] K. Fransham, R. Hasanen, and D. Karlen. A new technique for independent control of high voltage surfaces in a multi-GEM stack. *JINST*, 1(T11001), 2006.

[13] Sun Microsystems inc. Java communications. `http://java.sun.com/products/javacomm/`, 2006.

[14] Dean Karlen. jtpc analysis package. `http://www.linearcollider.ca/Members/karlen/jtpc/`, 2005.

[15] D. Karlen, P. Poffenberger, and G. Rosenbaum. TPC performance in magnetic fields with GEM and pad readout. *Nuclear Instruments and Methods in Physics Research A*, 555:80–92, 2005.

[16] John Apostolakis. GEANT - detector description and simulation tool. `http://wwwasd.web.cern.ch/wwwasd/geant/`, 2003.

[17] Stephen Biagi. Magboltz 2. http://cnlart.web.cern.ch/cnlart/2000/001/magboltz, 2000.

[18] J. Townsend. *Electrons in Gases*. Hutchinson, London, 1947.

[19] Gabriel Rosenbaum. Measuring the resolution of a GEM - TPC in a magnetic field. Master's thesis, University of Victoria, 2002.

[20] A. Buzulutskov et al. GEM operation in helium and neon at low temperatures. *arxiv-ph-0504184*, 2007.

[21] A. Bondar et al. High and low pressure operation of the gas electron multiplier. *Nuclear Instruments and Methods in Physics Research A*, 419, 1998.

[22] L Musa et al. The ALICE TPC front end electronics. Technical report, CERN, 2003.